



**MAX PLANCK INSTITUTE**  
FOR SOLID STATE RESEARCH



**University of Stuttgart**  
Germany

University of Stuttgart Institute of Materials Science - Department for Material Physics

Max Planck Institute for Solid State Research - Stuttgart Center for Electron Microscopy (StEM)

# **Elektronenptychographische Phasenbildung von vollständig anorganischen Halogenidperovskiten (AIHPs) mittels 4D STEM**

## **Electron ptychographic phase imaging of all-inorganic halide perovskites (AIHPs) using 4D STEM**

A thesis in the field of Transmission Electron Microscopy for the degree Master of Science in  
Materials Science

By **Anna Scheid** (3434644)

First corrector: Prof. Dr. Dr. h.c. Guido Schmitz

Second corrector: Prof. Dr. Peter A. van Aken

Supervisor: Dr. Yi Wang

September 2021



## **Declaration**

I, Anna Scheid, matr. no. 3434644, hereby declare that I have independently prepared and written this master's thesis entitled "Electron ptychographic phase imaging of all-inorganic halide perovskites (AIHPs) using binary 4D-STEM data". Only the indicated auxiliary means were used. All information taken verbatim or in spirit from other works is marked with the source, as are contributions by other persons. This also includes drawings, sketches as well as pictorial and graphical representations that were not made by my own hand. The work has not yet been published or presented in any other form as an examination performance.

Stuttgart: \_\_\_\_\_

Signature: \_\_\_\_\_

## **Acknowledgment**

First of all, I would like to thank Prof. Dr. Peter A. van Aken for giving me the opportunity to work in the field of STEM at the Max-Planck-Institute of Solid State Research in Stuttgart. Moreover, my special thanks go to Prof. Dr. Dr. h.c. Guido Schmitz for being my first corrector and his input to the project.

Many thanks go to Mina Jung and Dr. Davide Moia from the Physical Chemistry of Solids Department for providing me with the samples as well as their support in data evaluation and the inspiring discussions.

I would like to thank Dr. Tobias Heil and Dr. Wilfried Sigle for their enthusiastic support with every conceivable problem.

I am grateful to Kersten Hahn and Peter Kopold for their technical support with the instruments and their helpful advice.

Finally, yet importantly, I thank Prof. Dr. Peter A. van Aken and Dr. Yi Wang for the excellent supervision and the whole StEM group for the nice atmosphere and lively discussions. I liked every day and had a lot of fun with you.

Last but not least, I thank my family and Jan for their support, positive thoughts and for always believing in me.

# Contents

Declaration .....	I
Acknowledgment .....	II
List of Figures .....	V
List of Tables .....	VII
Abstract .....	VIII
Zusammenfassung .....	IX
1. Introduction .....	1
1.1. Transmission Electron microscopy .....	1
1.1.1. Imaging .....	1
1.1.1.1 CTM - Conventional transmission electron microscopy .....	1
1.1.1.2 STEM - Scanning transmission electron microscopy .....	2
1.1.2. Spectroscopy .....	3
1.1.2.1 EELS - Electron energy-loss spectroscopy .....	3
1.1.2.2 XEDS - X-ray energy-dispersive spectroscopy .....	3
1.1.3. Beam damage .....	3
1.2. Halide perovskites .....	4
1.3. Transmission electron microscopy of halide perovskites .....	5
1.4. Ptychography .....	7
1.4.1. From probe-forming lenses and apertures to detectors .....	7
1.4.2. Fundamentals .....	9
1.4.2.1 Single-side-band (SSB) reconstruction .....	12
1.4.2.2 Wigner distribution deconvolution (WDD) .....	14
2. Materials and Methods .....	15
2.1. Sample preparation .....	15
2.1.1. CsPbBr <sub>3</sub> nanocrystals .....	15
2.1.2. CsPbIBr <sub>2</sub> thin films .....	15
2.1.3. CsPbI <sub>3</sub> thin films .....	16
2.2. STEM investigations .....	16
2.3. 4D STEM data processing .....	16
2.4. Electron dose measurements .....	17
3. Results .....	18
3.1. Electron dose measurements .....	18
3.2. CsPbBr <sub>3</sub> .....	19
3.3. CsPbIBr <sub>2</sub> .....	24

3.4. CsPbI <sub>3</sub> .....	30
4. Discussion .....	34
4.1. Noise and dose efficiency .....	34
4.1.1. Direct electron detectors .....	34
4.1.2. Ptychography .....	36
4.2. Resolution.....	37
4.3. Thickness effects .....	40
4.4. Beam damage .....	43
4.4.1. Damage mechanism .....	43
4.4.2. TEM and STEM investigations of AIHPs .....	45
4.5. Sampling considerations.....	48
4.5.1. Probe step size .....	48
4.5.2. Detector sampling conditions .....	48
4.5.3. Binary ptychography.....	49
5. Summary .....	51
6. Outlook.....	52
7. References .....	53

## List of Figures

<b>Figure 1.</b> (a) Signals generated by electrons interacting with a sample material. <sup>7</sup> (b) and (c) show two basic conditions under which a TEM is operated: (b) conventional transmission electron microscopy (CTEM) with parallel beam illumination and (c) scanning transmission electron microscopy (STEM) with a convergent electron beam rastered over the sample surface. <sup>8</sup> .....	2
<b>Figure 2.</b> Schematic representation of the signal portion available for image generation with different detector geometries. (a) Bright-field detector (BF), (b) annular bright-field detector (ABF), (c) annular dark-field detector (ADF), (d) segmented detector, (e) direct electron detector. ....	2
<b>Figure 3.</b> Aristotype cubic perovskite structure, exemplified for SrTiO <sub>3</sub> belonging to the Pm3m space group, with TiO <sub>6</sub> octahedra highlighted in light blue. ....	4
<b>Figure 4.</b> Conventionally applied doses for the main (S)TEM techniques under conventional and low-dose conditions with charge-coupled devices (CCD) and direct electron cameras (DEC), adapted and modified from Zhou et al. <sup>44</sup> Red bars indicate maximum doses applicable to OIHPs and AIHPs before beam damage causes structural changes. ....	6
<b>Figure 5.</b> Two examples of successful imaging of the atomic structure of OIHPs (a-b) MAPbBr <sub>3</sub> and (c-e) FAPbI <sub>3</sub> . <sup>47,52</sup> (a) Unfiltered, raw HRTEM data of MAPbBr <sub>3</sub> and (b) CTF corrected, Wiener filtered image. (c) Unfiltered, raw low-angle annular dark-field image of FAPbI <sub>3</sub> , (d) Bragg filtered sub-area of (c) with enlarged section in the inset (e). Scale bars in (c), (d), and (e) correspond to 10 nm, 5 nm, and 1 nm.....	7
<b>Figure 6.</b> 4D STEM dataset. For each probe position in a scan, a 2D diffraction pattern is captured scanning over a periodic structure. 2D diffraction patterns from a sub-area of the structure are shown in the inset.....	9
<b>Figure 7.</b> (a) $G(Kf, Q0)$ summed over all detector coordinates $Kf$ as a function of $Q0$ . Amplitude in arbitrary units and phase in radians as a function of $Kf$ for two different spatial frequencies $Q0$ in (b) and (c). ....	12
<b>Figure 8.</b> Graphical representation of $GKf, Q0$ applying the WPOA for a SSB phase reconstruction. The overlap of the central beam centered at $Kf = 0$ and two scattered beams centered at $\pm Q0$ are shown exemplarily for two different spatial frequencies. As the spatial frequency increases, the regions of overlap become smaller until the discs finally separate for $Q0 = 2\alpha$ . ....	13
<b>Figure 9.</b> Amplitude and phase of $GKf, Q0$ for a spatial frequency $Q0$ as a function of detector coordinate $Kf$ . Double overlap regions were cut out by applying a mask that sets all other values to zero. ....	13
<b>Figure 10.</b> (a) Selected area for signal integration to determine the CCD camera counts, exemplified for a spot size of 2C. (b) Signals are integrated over areas with a signal greater than 0.1 % of the average signal. ....	18
<b>Figure 11.</b> ADF images of $\gamma$ -CsPbBr <sub>3</sub> . (a) Nanowire oriented along the [110] crystallographic direction. (b) Nanoplatelet oriented along the [001] crystallographic direction. ....	19
<b>Figure 12.</b> (a) Sub-region of $\gamma$ -CsPbBr <sub>3</sub> from which 400×400 CBEDs were captured. (b) Single CBED pattern recorded by the direct electron camera in 1-bit mode. (c) PACBED as a sum of all CBEDs for all probe positions in the scan. ....	20
<b>Figure 13.</b> Synthetic STEM images calculated by applying detector masks. (a) BF image using a mask that includes scattering angles of 0–10.2 mrad, (b) ABF image using a mask that includes scattering angles of 10.2–20.4 mrad and (c) ADF image using a mask that includes scattering angles of 34.9–50.2 mrad.....	21
<b>Figure 14.</b> Elemental mapping of $\gamma$ -CsPbBr <sub>3</sub> along [001]. (a) Simultaneously acquired ADF image, (b) extracted signal for the Cs M <sub>4,5</sub> edge, (c) extracted signal for the Br L <sub>2,3</sub> edge, (d) extracted signal for the Pb M <sub>4,5</sub> edge and (e) colorized map using the color scheme from (b-d). ....	22
<b>Figure 15.</b> Reconstructed phase in unit of radian of $\gamma$ -CsPbBr <sub>3</sub> along the [001] direction. (a) WDD and (b) SSB ptychography. In both cases, residual aberrations were neglected for image reconstruction.....	22

<b>Figure 16.</b> (a) ADF images of bright-contrast precipitates due to beam damage after irradiation with high electron doses pronounced at corners and edges. (b) Void formation in the host lattice upon precipitate growth, indicated by a red arrow leading to (c) dismantling of the host lattice (red circle). (d-f) Nanoplatelet after imaging with moderate doses with almost no beam damage visible.....	23
<b>Figure 17.</b> ADF images of the atomic structure of CsPbIBr <sub>2</sub> . (a) Image, captured with a low electron dose of $\sim 560 \text{ e}^-/\text{\AA}^2$ and (b) a dose of $\sim 1275 \text{ e}^-/\text{\AA}^2$ . Insets in (b) show possible structural orientations.....	24
<b>Figure 18.</b> Synthetic STEM images of $\gamma$ -CsPbIBr <sub>2</sub> calculated by applying detector masks. (a) BF image from a mask that includes scattering angles of 0–7.2 mrad, (b) ABF image using a mask that includes scattering angles of 7.2–14.4 mrad and (c) ADF image calculated from a mask that includes scattering angles of 53.3–92.2 mrad. ....	25
<b>Figure 19.</b> Reconstructed phase in unit of radian of $\gamma$ -CsPbIBr <sub>2</sub> along the [111] direction. (a) WDD and (b) SSB ptychography. In both cases residual aberrations were neglected for image reconstruction.....	25
<b>Figure 20.</b> EELS elemental maps extracted from stacks of signals around repeating sample features. For each feature elemental maps were extracted from raw and PCA filtered data. (a) Signal extracted around Cs atomic columns, (b) signal extracted around Br/I columns and (c) signal extracted from Pb atomic columns. ....	27
<b>Figure 21.</b> Damage pathway of $\gamma$ -CsPbIBr <sub>2</sub> with increasing dose. (a) No damage was observed after low-dose imaging and 4D STEM. (b) With conventional imaging doses, beam damage occurred after a few scans as high-contrast nanoprecipitates indicated by arrows. (c) After high-dose SI acquisition, a large number of nanoparticles formed, dismantling the lattice and leaving a hole behind (d). ....	28
<b>Figure 22.</b> (a) Cubic metallic lead precipitate with an overlay of the atomic structure in the inset. (b) Distorted host lattice due to precipitate diffusion under electron beam irradiation. (c) Secondary phase forming in severely damaged areas as lead leaves the lattice. ....	28
<b>Figure 23.</b> Elemental maps extracted from EELS and XEDS SIs. Due to the low signal-to-background ratio of Pb signals in EELS measurements, XEDS maps were extracted to confirm the presence of Pb nanoprecipitates.....	29
<b>Figure 24.</b> (a) Simultaneously acquired ADF image of the damaged structure containing a severely damaged area. (b) XEDS spectra extracted from the insets in (a) for an area of low damage (blue) and severe damage (red). The spectra were normalized to the Cu <sub>K<math>\alpha</math>1,2</sub> peak of the supporting grid.....	29
<b>Figure 25.</b> ADF images of CsPbI <sub>3</sub> . (a) Image acquired with a dose of $\sim 830 \text{ e}^-/\text{\AA}^2$ . Beam damage in the form of bright-contrast lead precipitates is visible and indicated by red arrows. (b) Image acquired with a dose of $\sim 2110 \text{ e}^-/\text{\AA}^2$ . Distorted host lattice due to mobile lead precipitates, highlighted by red circles. (c) High magnification image with structural inset. The image was acquired with a dose of $\sim 4530 \text{ e}^-/\text{\AA}^2$ . ....	30
<b>Figure 26.</b> (a) ADF image captured with a dose of $\sim 630 \text{ e}^-/\text{\AA}^2$ and a beam current of $\sim 0.23 \text{ pA}$ . Beam damage is observed close to the specimen edge, indicated by red arrows. (b) Higher magnification image acquired with a dose of $\sim 1180 \text{ e}^-/\text{\AA}^2$ and a beam current of $\sim 0.19 \text{ pA}$ . The insets in (b) show possible crystal orientations. ....	31
<b>Figure 27.</b> Synthetic STEM images of $\gamma$ -CsPbI <sub>3</sub> calculated by applying detector masks. (a) BF image from a mask that includes scattering angles of 0–7.2 mrad, (b) ABF image using a mask that includes scattering angles of 7.2–14.4 mrad and (c) ADF image calculated from a mask that includes scattering angles of 53.3–92.2 mrad. ....	31
<b>Figure 28.</b> Reconstructed phase in radians of $\gamma$ -CsPbI <sub>3</sub> along the [111] direction. (a) WDD and (b) SSB ptychography. In both cases, residual aberrations were neglected for image reconstruction. ..	32
<b>Figure 29.</b> Severely damaged perovskite lattice after high-dose irradiation. In addition to the formation of lead nanoparticles, the formation of a second phase was observed.....	33



<b>Figure 30.</b> Maps, extracted from an EELS SI of a copper precipitate. (a) Simultaneously acquired ADF image, (b) extracted signal for the $I M_{4,5}$ edge, (c) extracted signal for the $Cs M_{4,5}$ edge, (d) extracted signal for the $Cu L_{2,3}$ edge. ....	33
<b>Figure 31.</b> Comparison of WDD phase reconstruction results for $CsPbI_3$ . Enlarged subsections are shown for $\epsilon$ ratios of (a) 0.01, (b) 0.1 and (c) 1. ....	37
<b>Figure 32.</b> Power spectra of $GKf, Q0$ for (a) $CsPbBr_3$ , (b) $CsPbIBr_2$ and (c) $CsPbI_3$ . Big red circles indicate the diffraction limited resolution. For each power spectrum, two spatial frequencies with a high contribution are illustrated and the phase of $GKf, Q0$ is shown as a function of $Kf$ . For each inset the whole bright-field disc is shown at the top and extracted signal relevant for the phase reconstruction at the bottom. ....	38
<b>Figure 33.</b> Lead precipitates upon beam damage in $CsPbX_3$ perovskites. (a) STEM HAADF images of $CsPbBr_3$ nanocrystals with cubic Pb precipitates oriented along the [001] direction. <sup>102</sup> (b) STEM HAADF image of a $CsPbI_3$ nanocrystal with bright-contrast Pb precipitates. ....	46
<b>Figure 34.</b> Experimental and simulated images of different domains in a single $CsPbBr_3$ nanocrystal. (a) Perovskite phase and (b) Ruddlesden-Popper type structure both with poor Br and Cs contrast. ....	46
<b>Figure 35.</b> (a) Simultaneously acquired ADF image of $CsPbBr_3$ with high noise level and poor Br contrast and (b) phase reconstructed image with enhanced contrast for all elements. <sup>105</sup> Scale bars in (a) and (b) are 5 Å. (b) Phase image of $CsPbBr_3$ obtained by exit wave reconstruction of 80 low dose-rate HRTEM images. <sup>106</sup> ....	47
<b>Figure 36.</b> Atomic resolution XEDS elemental mapping of an orthorhombic $CsPbBr_3$ nanocrystal. (a) Simultaneously acquired ADF image, (b) Cs atomic columns, (c) Pb atomic columns, and (d) Br atomic columns. <sup>107</sup> ....	47
<b>Figure 37.</b> Example single frame binary CBED patterns from (a) $CsPbBr_3$ , (b) $CsPbIBr_2$ , and (c) $CsPbI_3$ datasets. Red dashed circles indicate the radius of the bright-field disc. ....	49

## List of Tables

<b>Table 1.</b> Beam current and corresponding counts measured by the CCD camera for different spot sizes and apertures. A conversion factor for the counts per electron was calculated for each combination. ....	19
<b>Table 2.</b> Maximum sample thickness to achieve the diffraction limited resolution for a given aperture. Three approximations presented by Rodenburg (equation (4.5)), Chapman (equation (4.6)), and Tsai (equation (4.7)). <sup>54,85,86</sup> ....	41
<b>Table 3.</b> Maximum possible resolution for a given thickness or thickness range calculated by reversing equations (4.5), (4.6), and (4.7). ....	41

## Abstract

Both inorganic and organic-inorganic halide perovskites (HPs) are promising candidates for optoelectronic devices such as solar cells or light-emitting diodes. Despite recent progress in performance optimization and low-cost manufacturing, their commercialization remains hindered due to structural instabilities. HPs are very sensitive to various environmental conditions such as humidity, temperature and radiation. Microscopic properties and degradation mechanisms are still not well understood. Transmission electron microscopy (TEM) can benefit the fundamental understanding of structure-property relationships and plays an important role in revealing microstructural, morphological as well as chemical or physical information. However, the extreme sensitivity of HPs towards electron-beam irradiation prevents access to intrinsic information or leads to artifacts. Imaging is severely limited, especially at high magnifications, and the key factor for TEM studies is the electron dose. Whereas high-resolution TEM (HRTEM) is an effective way to reveal atomic structures under low-dose conditions, the image contrast depends on experimental parameters and is hard to interpret directly. While contrast is directly interpretable in scanning transmission electron microscopy (STEM), low-dose conditions are particularly difficult. Conventional, scintillator-based detectors make use of only a fraction of the total information and perform poorly at low doses. However, technological advances and the development of direct electron cameras (DECs) that can accurately determine the position of an incoming scattered electron have opened up a whole new field of electron microscopy: 4D STEM. A four-dimensional dataset represents two dimensions in real space, the position of the electron probe, and two dimensions in reciprocal space, the detector plane. For each probe position, a convergent electron beam diffraction (CBED) pattern is recorded. From the recorded CBEDs it is not only possible to extract the signal for any STEM detector geometry, but also the phase problem can be solved. Utilizing the coherent interference in the overlap region between direct and scattered beams, the phase and amplitude of the electron wave can be reconstructed. This method, called electron ptychography is a combination of diffraction and imaging. This thesis aims to show the potential of 4D STEM, in particular phase reconstructions via focused probe ptychography. Two non-iterative reconstructions based on weak-phase- and phase-object approximation are presented. Single-side-band (SSB) and Wigner distribution deconvolution (WDD) ptychography are introduced as low-dose, dose-efficient techniques to image the atomic structure of beam-sensitive HPs. The advantages of DECs allow the acquisition of sparse binary diffraction patterns with distinguishable individual electron events. Atomically resolved, almost aberration-free phase images of three all-inorganic halide perovskites, CsPbBr<sub>3</sub>, CsPbIBr<sub>2</sub>, and CsPbI<sub>3</sub> are presented with a resolution down to the aperture-constrained diffraction limit.

## Zusammenfassung

Sowohl anorganische als auch organisch-anorganische Halogenidperowskite (HPs) sind vielversprechende Kandidaten für optoelektronische Bauelemente wie Solarzellen oder Leuchtdioden. Trotz großer Fortschritte bei der Leistungsoptimierung und der kostengünstigen Herstellung wird ihre Kommerzialisierung durch ihre strukturelle Instabilität verhindert. HPs sind sehr anfällig gegenüber verschiedenen Umwelteinflüssen wie Feuchtigkeit, Temperatur und Bestrahlung. Die mikroskopischen Eigenschaften und die Schädigungsmechanismen sind noch immer nicht ausreichend verstanden. Die Transmissionselektronenmikroskopie (TEM) kann zum grundlegenden Verständnis der Struktur-Eigenschafts-Beziehungen beitragen und spielt eine wichtige Rolle bei der Aufdeckung von mikrostrukturellen, morphologischen sowie chemischen und physikalischen Eigenschaften. Allerdings verhindert die extreme Empfindlichkeit von HPs gegenüber dem Elektronenstrahl den Zugang zu intrinsischen Informationen oder führt zu Artefakten. Insbesondere bei hohen Vergrößerungen gestalten sich Untersuchungen schwierig, wobei die Dosis der Schlüsselfaktor ist. Während die hochauflösende TEM (HRTEM) ein effektives Mittel ist, um atomare Strukturen bei niedriger Dosis abzubilden, hängt der Bildkontrast hier von experimentellen Parametern ab und ist schwer direkt zu interpretieren. Während bei Raster-Transmissionselektronenmikroskopie (RTEM) der Kontrast direkt interpretierbar ist, sind die Bedingungen bei niedriger Dosis besonders schwierig. Herkömmliche, auf Szintillatoren basierende Detektoren nutzen nur einen Bruchteil der Gesamtinformation und sind für niedrige Dosen ungeeignet. Technischer Fortschritt und die Entwicklung direkter Elektronenkameras (DEKs), die die Position eines eintreffenden gestreuten Elektrons genau bestimmen können, haben ein neues Feld in der Elektronenmikroskopie eröffnet: 4D RTEM. Ein vierdimensionaler Datensatz repräsentiert zwei Dimensionen im realen Raum, die Position des Strahls, und zwei Dimensionen im reziproken Raum, die Detektorebene. Für jede Strahlposition wird ein konvergentes Elektronenstrahlbeugungsmuster aufgezeichnet. Aus den aufgezeichneten Beugungsmustern lässt sich nicht nur das Signal für jede mögliche RTEM-Detektorgeometrie extrahieren, sondern auch das Phasenproblem lösen. Mit Hilfe der kohärenten Interferenz im Überlappungsbereich zwischen direktem und gestreutem Strahl können Phase und Amplitude der Elektronenwelle rekonstruiert werden. Diese Methode, Elektronenptychographie genannt, ist eine Kombination aus Beugung und Bildgebung. Ziel dieser Arbeit ist es, das Potenzial von 4D RTEM, insbesondere der Ptychographie mittels fokussiertem Strahl, aufzuzeigen. Es werden zwei nicht-iterative Algorithmen genutzt, die auf schwacher Phasen- und Phasenobjektnäherung beruhen. Single-Side-Band (SSB) und Wigner Distribution Deconvolution (WDD) Ptychographie werden als dosisarme, dosiseffiziente Techniken zur Abbildung der atomaren Struktur von strahlungsempfindlichen HPs vorgestellt. Die Vorteile von DEKs ermöglichen die Aufnahme binärer Beugungsmuster mit unterscheidbaren einzelnen Elektronenereignissen. Es werden nahezu aberrationsfreie Phasenbilder von drei anorganischen HPs,  $\text{CsPbBr}_3$ ,  $\text{CsPbIBr}_2$  und  $\text{CsPbI}_3$ , mit einer Auflösung bis hin zur Beugungsgrenze gezeigt.



# 1. Introduction

## 1.1. Transmission Electron microscopy

Nowadays, transmission electron microscopy (TEM) is an indispensable tool for structural and compositional characterization of materials from the micrometer to the Angstrom scale. TEM plays a significant role in materials science, physics, chemistry, and biology, especially in research fields such as nanotechnology, renewable energy or medicine.<sup>1-4</sup> Since the construction of the first TEM in 1931 by Max Knoll and Ernst Ruska, technical developments in sample preservation, aberration correction, detector performance, and computational power have opened the doors to a large variety of imaging and analytical technologies that are still being optimized and improved today. Illumination of a material with an electron beam causes the beam electrons to interact with the sample, producing a variety of signals, as shown in Figure 1(a). Elastically scattered electrons are used for high resolution imaging (HRTEM), diffraction imaging, or scanning transmission electron microscopy imaging (STEM). Inelastically scattered electrons and their secondary effects are useful for analytical spectroscopy such as x-ray energy-dispersive spectroscopy (XEDS) or electron energy-loss spectroscopy (EELS). In general, there are two TEM configurations that offer unique opportunities for material characterization. With a specific arrangement of electromagnetic lenses and apertures, the microscope can be operated as a conventional transmission electron microscope (CTEM) or as a scanning transmission electron microscope (STEM).<sup>5,6</sup>

### 1.1.1. Imaging

#### 1.1.1.1 CTEM - Conventional transmission electron microscopy

Electrons emitted from a source are accelerated and pass through a series of tunable electromagnetic lenses that deflect the electrons using Lorentz forces. In CTEM, the electrons are focused into a parallel beam that impinges on the sample (Figure 1(b)).<sup>7,8</sup> The transmitted beam is dispersed by an objective lens to form a diffraction pattern in the back focal plane (BFP) and recombined into an image in the image plane (IP). The electrons are further directed through a system of imaging lenses and projected onto pixelated detectors such as CCD (charge-coupled device) or CMOS (complementary metal-oxide-semiconductor) devices. If the BFP of the objective lens is selected as an object plane for the intermediate lens, a diffraction pattern is projected onto the screen. If the IP is selected, an image is projected onto the screen. The illumination can also be tilted that a specific set of diffracted beams passes through the objective aperture. This allows the study of particular diffraction features in a sample via dark-field TEM.<sup>7,9</sup> If the electron beam is converged, the sharp diffraction spots broaden into discs. The resulting diffraction pattern, called convergent electron diffraction pattern (CBED), contains additional information about symmetry, structure factors and lattice strains.<sup>10</sup>

### 1.1.1.2 STEM - Scanning transmission electron microscopy

In the scanning configuration, a convergent electron beam of variable diameter is generated for high-resolution imaging. The probe is scanned across the sample surface using scan coils (Figure 1(c)).<sup>8</sup>

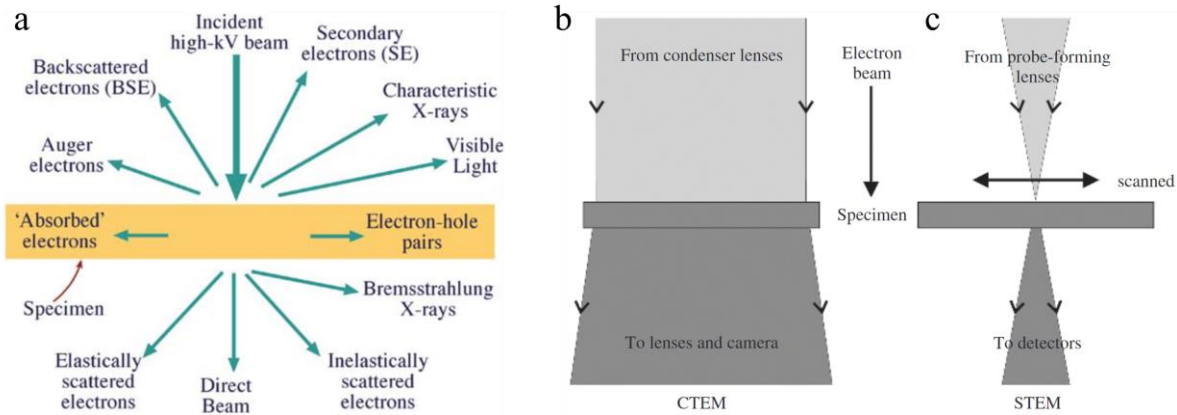


**Figure 1.** (a) Signals generated by electrons interacting with a sample material.<sup>7</sup> (b) and (c) show two basic conditions under which a TEM is operated: (b) conventional transmission electron microscopy (CTEM) with parallel beam illumination and (c) scanning transmission electron microscopy (STEM) with a convergent electron beam rastered over the sample surface.<sup>8</sup>

The scattered electrons, which form a CBED for each position in the scan, are recorded by different types of detectors. In conventional imaging, an image is generated by integrating the signal for each probe position as one pixel. Detector geometry and illumination determine the contrast. The fraction of electrons used for signal generation is shown schematically in Figure 2 for different detector geometries. Bright-field detectors select a portion of the electrons belonging to the direct beam. Annular bright-field detectors (ABF) gather a portion of electrons falling on an annular detector placed inside the bright-field disc. In bright-field imaging, the contrast depends on the interference of the direct and scattered electrons. In contrast, annular dark-field detectors (ADF) select any scattered electrons. The detector surrounds the direct beam and contains a hole in the center where the bright-field detector is located. The contrast can be directly related to the composition and thickness of the sample, independent of interference effects. In general, annular detectors can also be split into segments and used as quadrant detectors.<sup>11</sup> In contrast to conventionally used single-channel integrating detectors, in advanced techniques such as four-dimensional STEM (4D STEM), direct electron detectors (DECs) capture a whole CBED pattern for each probe position. 4D STEM techniques offer possibilities for virtual imaging, orientation mapping and strain mapping, phase contrast imaging, etc.<sup>12</sup>

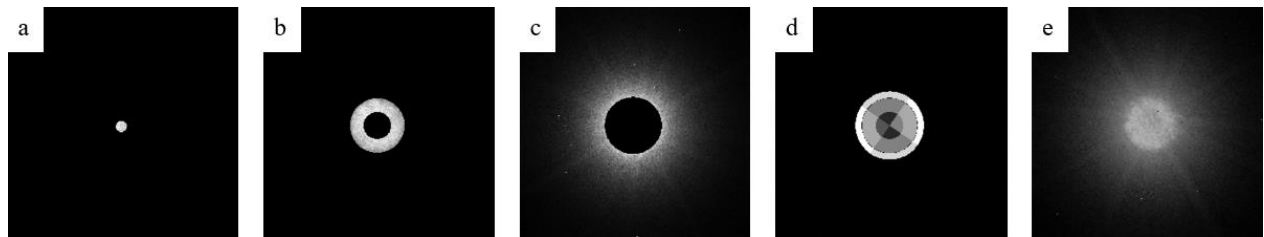


**Figure 2.** Schematic representation of the signal portion available for image generation with different detector geometries. (a) Bright-field detector (BF), (b) annular bright-field detector (ABF), (c) annular dark-field detector (ADF), (d) segmented detector, (e) direct electron detector.

## **1.1.2. Spectroscopy**

### **1.1.2.1 EELS - Electron energy-loss spectroscopy**

EELS is the investigation of the energy distribution of electrons transmitted through a specimen. During scattering, electrons may lose (inelastic scattering) or not lose (elastic scattering) energy. The energy loss of inelastically scattered electrons can be related to the chemistry and electronic structure of the specimen (valence states, dielectric properties, band gaps, thickness, etc.).<sup>13–16</sup> Transmitted electrons are sent through a magnetic prism and deflected through  $\geq 90^\circ$  by a magnetic field. Electrons with a high energy loss are deflected further than electrons with a low loss as they travel through the spectrometer at the end of the microscope column. A spectrum is captured as an intensity distribution as a function of energy loss.<sup>17</sup> In general, an EEL spectrum is divided into two parts, the low-loss spectrum (energy loss  $< \sim 50$  eV) and the high-loss spectrum (energy loss  $> \sim 50$  eV). The low-loss spectrum includes the zero-loss and plasmonic peaks and provides information about dielectric properties and band structure. The high-loss spectrum contains element-specific ionization edges due to inner shell ionization and provides information about the sample chemistry.<sup>18</sup> Element-specific electron energy losses are utilized in the field of energy-filtered TEM (EFTEM). Energy filters select a specific energy range of electrons that contribute to the image in CTEM.<sup>19</sup>

### **1.1.2.2 XEDS - X-ray energy-dispersive spectroscopy**

If an electron is scattered inelastically, it may excite a sample electron from an inner shell, ejecting it and leaving an electron hole. The hole fills with an electron from an outer shell of higher energy. The excess energy can be released in the form of an element-specific characteristic x-ray. The amount and energy of characteristic x-rays are measured by an energy dispersive spectrometer positioned above the specimen plane in the TEM. XEDS allows for quantitative and qualitative elemental analysis.<sup>20</sup> This technique is particularly useful for heavy element characterization due to an increase in the x-ray emission probability with the atomic weight, whereas the emission probability of Auger electrons decreases. In an Auger electron event, excess energy is not emitted as an x-ray but is transferred to another sample electron that leaves the material.<sup>21–23</sup>

### **1.1.3. Beam damage**

TEM can achieve characterizations on a multiple-scale level from the micrometer to the atomic level and contribute strongly to the fundamental understanding of degradation mechanisms and structure-property relationships of materials. Illumination of a material with an electron beam results in an interaction between beam electrons and sample electrons causing scattering events of either elastic or inelastic nature. The inelastic events introduce an unfavored side effect, namely beam damage. The damage mechanisms vary from material to material and include knock-on damage, radiolysis and heating. They affect the structure and/or the chemistry of the material and may lead to misinterpretations if ignored. Different damaging mechanisms require precautions to prevent or minimize their effects when investigating beam-sensitive

materials. Inelastically scattered electrons that pass close to the atomic nucleus are scattered at high angles and lose a large amount of energy sufficient to displace the entire atom from its initial position. This so-called knock-on damage results in point defect formation and can be avoided by lowering the electron beam energy below the displacement energy threshold of the material components. Phonon heating, which mainly affects materials with low thermal conductivity, is an effect of energy transfer of incident electrons inducing lattice vibrations. Phonon heating can be minimized by cooling the sample to cryogenic temperatures and minimizing the cross section for inelastic scattering. Furthermore, the electron beam may induce changes in the chemical bonding of the materials by radiolysis, causing bond breakage, loss of crystallinity or escape of light elements. Radiolysis is often observed in polymers and alkali halides. In conducting materials, electron holes in the conduction or valence band are rapidly filled by electrons in the system, making metals resistant to this form of damage. To minimize the effects of radiolysis, the interaction cross section must be reduced, i.e., the TEM should be operated with the highest possible voltage and the specimen should be as thin as possible.<sup>7,24,25</sup>

## 1.2. Halide perovskites

The designation “perovskite” was initially coined by Gustav Rose, who named the as yet unknown mineral  $\text{CaTiO}_3$  after the Russian politician and mineralogist Lev Alexeyevich Perovski in 1839.<sup>26</sup> Nowadays, perovskites are known as materials that crystallize in a general  $\text{ABX}_3$  stoichiometry. They contain a network of corner-sharing  $\text{BX}_6$  octahedra as illustrated in Figure 3 on the prime example  $\text{SrTiO}_3$  as an aristotype belonging to the  $\text{Pm}\bar{3}\text{m}$  space group.<sup>27</sup>

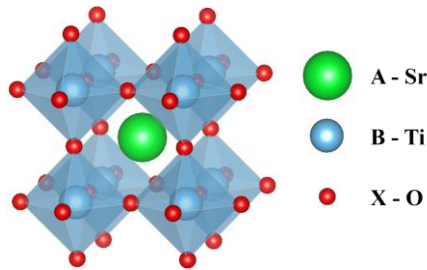


**Figure 3.** Aristotype cubic perovskite structure, exemplified for  $\text{SrTiO}_3$  belonging to the  $\text{Pm}\bar{3}\text{m}$  space group, with  $\text{TiO}_6$  octahedra highlighted in light blue.

Most perovskite materials are so-called hettotypes, owning a structure of lower symmetry due to lattice- and octahedral distortions, ordering of vacancies or cations or due to the presence of organic cations in the material.<sup>27,28</sup> Halide perovskites (HPs) are a subgroup of perovskites characterized by halides as their X-anions, usually  $\text{Cl}^-$ ,  $\text{I}^-$ , or  $\text{Br}^-$ . The B-ions are divalent metal cations such as  $\text{Pb}^{2+}$ ,  $\text{Sn}^{2+}$  or  $\text{Ge}^{2+}$ . Depending on the A-site cation, HPs are further classified into all-inorganic halide perovskites (AIHP) and organic-inorganic halide perovskites (OIHP). AIHPs contain  $\text{Cs}^+$  and OIHPs  $\text{CH}_3\text{NH}_3^+$  (Methyammonium) or  $\text{HC}(\text{NH}_2)_2^+$  (Formamidinium) as A-site cations.<sup>29,30</sup> HPs are promising candidates for optoelectronic devices, such as photovoltaic (PV) solar cells, lasers, photodetectors, scintillators or light-emitting diodes



(LEDs) due to their excellent optoelectronic properties, such as tunable band gaps, light-harvesting capability, and high charge-carrier mobility.<sup>31–36</sup> Especially in the field of solar-cell devices, OIHPs have attracted widespread interest since the pioneering work of Miyasaka and coworkers in 2009. They initially reported a conversion efficiency of 3.8 %, which was improved to 25.5 % recently in 2020, approaching the record value for silicon-based devices of 26.7 %.<sup>37,38</sup> Since most perovskite-based devices are fabricated by low-cost solution processing, they meet two of the four main criteria for the commercialization of PV techniques. In addition to high power-conversion efficiency (PCE) and low production cost, low toxicity and long-term stability are critical factors for the commercialization of optoelectronic devices.<sup>39</sup> The toxicity issues associated with the use of lead-based HPs are mainly overcome by appropriate encapsulation or lead-free perovskite alternatives, e.g., using  $\text{Sn}^{2+}$  as B-site cation.<sup>40</sup> The more critical factor limiting the commercial production is their insufficient long-term stability in operation. The causes of rapid degradation range from minor changes in defect concentration to severe structural degradation, depending on the environmental stresses to which the material is exposed in service. Structural point defects such as vacancies or lattice distortions induced by lattice strains are the main factors responsible for the susceptibility of HPs towards external stimuli and can barely be avoided during thin film fabrication due to the soft ionic nature of HPs. Environmental stresses such as temperature, moisture, oxygen, solar illumination, electrical biasing, etc. are the main external stimuli for degradation. Therefore, it is of great importance to understand degradation mechanisms and structure-property relationships of these materials to solve stability problems via doping, precursor additive engineering, compositional engineering, surface post-treatments, hetero-junction control, etc.<sup>39,41,42</sup>

### 1.3. Transmission electron microscopy of halide perovskites

Although TEM offers a variety of techniques for multiple-scale characterizations and would be an excellent tool to study stability issues, (atomic resolution) imaging of HPs is difficult due to their extreme sensitivity towards electron beam irradiation. It has been shown that OIHP  $\text{MAPbI}_3$  (MA = Methylammonium) shows first signs of beam-induced damage at doses as low as  $100 \text{ e}^-/\text{\AA}^2$ . The material degrades to  $\text{PbI}_2$  within  $2200 \text{ e}^-/\text{\AA}^2$  via intermediate superstructures.<sup>43</sup> In the case of AIHP  $\text{CsPbIBr}_2$ , investigated with a 300 kV electron beam, beam damage occurred at doses higher than  $6000\text{--}8000 \text{ e}^-/\text{\AA}^2$ . During degradation, structural changes via an intermediate phase ( $\text{CsPb}_{(1-x)}(\text{IBr})_{(3-y)}$ ), the formation of Pb nanoparticles and a  $\text{Cs}_2\text{IBr}$  phase as well as I/Br desorbing from the material were observed.<sup>44</sup> Dang et al. studied beam damage in AIHP  $\text{CsPbBr}_3$  nanocrystals at different acceleration voltages (80/200 kV) and different temperatures. They suggest that radiolysis is the dominant damaging mechanism causing electron-stimulated desorption of Br and the formation of Pb nanoparticles for doses in the range of  $10^3 \text{ e}^-/\text{\AA}^2$ . The speed of degradation depends strongly on the surface-to-volume ratio and increases with temperature.<sup>45</sup> The extreme beam sensitivity of these materials has been ignored in many literature studies, leading to incomplete or wrong interpretations. For instance, Chen et al. identified more than 20 publications in which authors incorrectly identified the

decomposition product  $\text{PbI}_2$  as  $\text{MAPbI}_3$  based on the similarity of their electron diffraction patterns along several zone axes. The researchers ignored the absence of reflections in the diffraction patterns which must be present in the case of  $\text{MAPbI}_3$ .<sup>25,46</sup> Which mechanism of beam damage dominates in AIHPs and OIHPs is still controversial, but conclusions can be drawn from experiments under different conditions. It has been shown that beam damage is slower when high acceleration voltages are used.<sup>45,47</sup> The question of whether or not cryogenic conditions should be used to study HPs is still controversial. Some researchers claim that the critical dose for  $\text{MAPbBr}_3$  increases fourfold at cryogenic temperatures, from  $11 \text{ e}^-/\text{\AA}^2$  up to  $46 \text{ e}^-/\text{\AA}^2$ .<sup>48</sup> However, Chen et al. noted that superstructure reflections in the FFT pattern at  $7.6 \text{ e}^-/\text{\AA}^2$  were disregarded in this study indicating that beam damage began much earlier.<sup>25</sup> The majority of researchers agrees that low temperatures lead to a rapid amorphization of the material without any suppression of beam damage.<sup>47</sup> Rothmann et al. observed a rapid crystalline - amorphous transition of  $\text{MAPbI}_3$  within  $1440 \text{ e}^-/\text{\AA}^2$  at  $-180^\circ\text{C}$  and  $3720 \text{ e}^-/\text{\AA}^2$  at room temperature. Atomic defects formed under irradiation become frozen and immobile at cryogenic temperatures, accumulate into clusters, and become amorphous. Similar amorphization has been observed for  $\text{MAPbBr}_3$ .<sup>46,49</sup> Unlike materials that are sensitive towards the dose rate, such as zeolites, HPs are sensitive to the cumulative electron dose. Beam damage occurred at very low dose rates ( $1 \text{ e}^-/\text{\AA}^2$ ) in OIHPs. Besides that, damage was visible in  $\text{CsPbIBr}_2$  after applying a similar total dose at different dose rates.<sup>43,44,50</sup> Given the extreme radiation sensitivity of these materials, few (S)TEM imaging techniques are suitable to image HPs. Figure 4 shows a rough estimate of the doses used for different (S)TEM imaging techniques. The threshold ranges for maximum doses for OIHPs and AIHPs reported in the literature are highlighted by red bars in the  $10^2 \text{ e}^-/\text{\AA}^2$  and  $10^3 \text{ e}^-/\text{\AA}^2$  range respectively.<sup>44</sup>

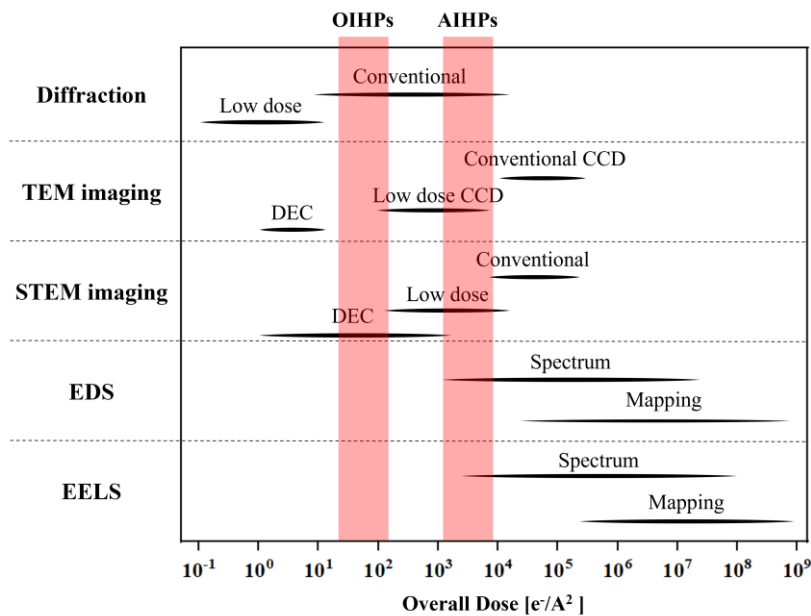


**Figure 4.** Conventionally applied doses for the main (S)TEM techniques under conventional and low-dose conditions with charge-coupled devices (CCD) and direct electron cameras (DEC), adapted and modified from Zhou et al.<sup>44</sup> Red bars indicate maximum doses applicable to OIHPs and AIHPs before beam damage causes structural changes.

To date, only a few successful atomic resolution images of these materials without any structural damage or phase transition exist, most of them captured under extreme low-dose conditions with poor signal-to-noise ratios. To improve the image quality, most images were additionally filtered e.g., using Bragg- or Butterworth filters<sup>47</sup>, Fourier filters<sup>51</sup>, ABSF- and Wiener filters<sup>52</sup>. Two examples of a low-dose HRTEM and a low-dose STEM image of OIHPs are shown in Figure 5. Besides low-dose HRTEM imaging with direct electron detectors, recent progress in the establishment of advanced 4D STEM techniques provide a new pathway to investigate beam-sensitive materials with a dose-efficient low-dose phase-retrieval technique, called electron ptychography. This work aims to demonstrate the efficiency of electron ptychography for high-contrast imaging of beam-sensitive HPs under conventional and low-dose conditions to reveal the undamaged atomic structure of CsPbBr<sub>3</sub>, CsPbIBr<sub>2</sub>, and CsPbI<sub>3</sub>.

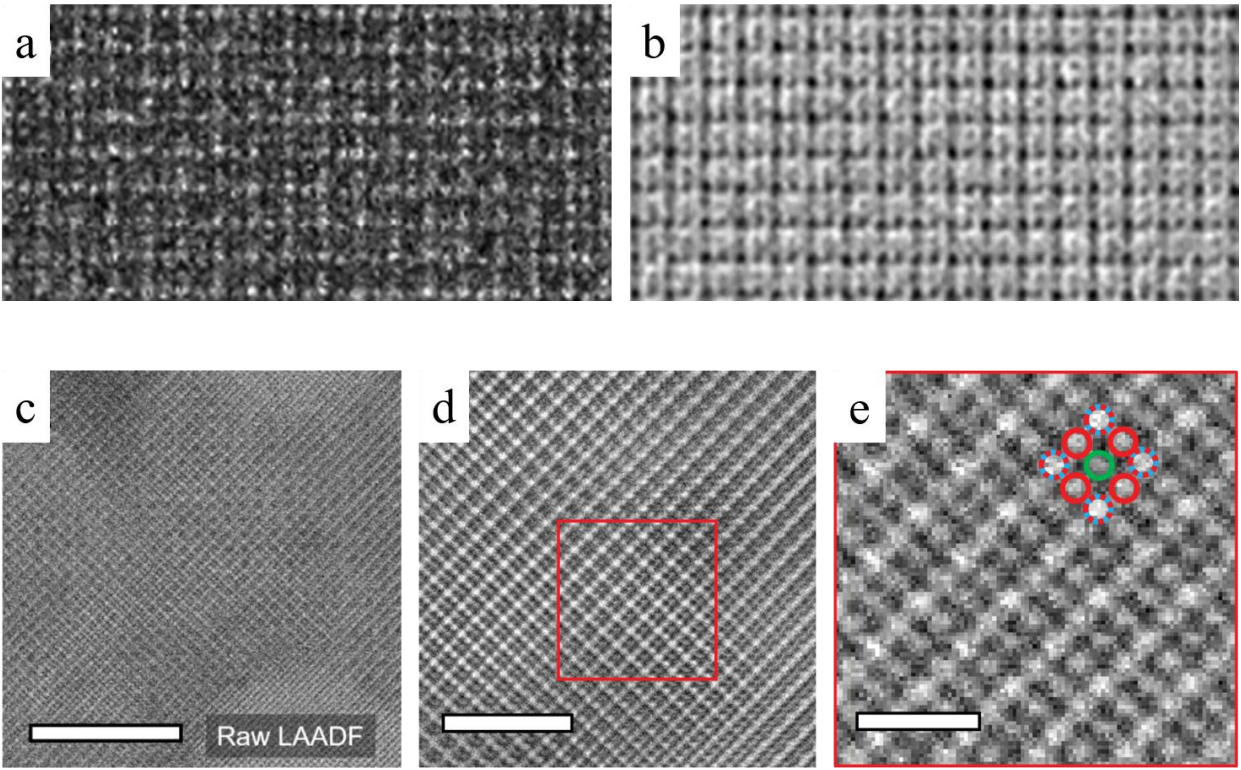


**Figure 5.** Two examples of successful imaging of the atomic structure of OIHPs (a-b) MAPbBr<sub>3</sub> and (c-e) FAPbI<sub>3</sub>.<sup>47,52</sup> (a) Unfiltered, raw HRTEM data of MAPbBr<sub>3</sub> and (b) CTF corrected, Wiener filtered image. (c) Unfiltered, raw low-angle annular dark-field image of FAPbI<sub>3</sub>, (d) Bragg filtered sub-area of (c) with enlarged section in the inset (e). Scale bars in (c), (d), and (e) correspond to 10 nm, 5 nm, and 1 nm.

## 1.4. Ptychography

### 1.4.1. From probe-forming lenses and apertures to detectors

If a thin sample could be illuminated by a convergent electron beam without the use of apertures and imperfect electromagnetic lenses, changes in the electron wave would be implied only by the presence of the sample and thus depend on the atomic potential of the material. However, to focus the electrons to form a small probe, they need to pass through a system of lenses and apertures on their way down the microscope

column. Since electromagnetic lenses are highly imperfect, apertures are used to limit the angular range to minimize lens aberration effects, and a particular defocus value can be chosen. The presence of the probe-forming system affects the electron wave incident on the sample. Mathematically, the electron wave passing through the lens and aperture system is described as a complex function called aperture function  $A(\mathbf{K})$ .<sup>7,53–</sup>

55

$$A(\mathbf{K}) = T(\mathbf{K}) \exp(i\chi(\mathbf{K})) \quad (1.1)$$

The wave amplitude  $T(\mathbf{K})$  represents the aperture limit in terms of a top-hat function.

$$T(\mathbf{K}) = 1 \quad \text{if } |\mathbf{K}| < K_{\max} \quad (1.2)$$

$$T(\mathbf{K}) = 0 \quad \text{if } |\mathbf{K}| \geq K_{\max} \quad (1.3)$$

Thus, for reciprocal-space vectors  $\mathbf{K}$ , which are not allowed to pass the aperture, the amplitude of the wave function is zero.  $\chi(\mathbf{K})$  describes the phase of the electron wave affected by lens imperfections. The lens aberration function  $\chi(\mathbf{K})$  is given here only for the lowest-order rotationally symmetric aberrations.<sup>53</sup>

$$\chi(\mathbf{K}) = (\pi C_{1,0} |\mathbf{K}|^2 \lambda + \frac{1}{2} \pi C_{3,0} |\mathbf{K}|^4 \lambda^3) \quad (1.4)$$

with  $C_{1,0}$  = defocus,  $C_{3,0}$  = spherical aberration coefficient of the objective lens,  $\lambda$  = electron wavelength.

For a perfectly coherent electron beam without the influences of any lens imperfections, the phase  $\chi(\mathbf{K})$  would be constant at constant convergence angles. The electron beam is focused on the sample using a lens system to form a probe. Mathematically, this is equivalent to the inverse Fourier transform of the aperture function  $A(\mathbf{K})$  (reciprocal space) resulting in the probe function  $P(\mathbf{R})$  (real space).<sup>53</sup> For simplicity, researchers in the field of ptychography have agreed to perform forward (1.5) and backward (1.6) Fourier transformations using the following convention:

$$F(y) = FT_x[f(x)] = \int f(x) \exp(2\pi i x \cdot y) dx \quad (1.5)$$

$$f(x) = IFT_y[F(y)] = \int F(y) \exp(-2\pi i y \cdot x) dy \quad (1.6)$$

Therefore, the probe function is given in this case as

$$P(\mathbf{R}) = IFT_K[A(\mathbf{K})] = \int A(\mathbf{K}) \exp(-2\pi i \mathbf{K} \cdot \mathbf{R}) d\mathbf{K} \quad (1.7)$$

Assuming that the sample is thin enough to follow the phase-object approximation, the interaction of electrons with the sample leads only to a change in the phase of the electron wave and not in the amplitude. Therefore, a multiplicative approximation is used to describe the exit wave  $\psi(\mathbf{R}, \mathbf{R}_0)$  as a product of real-space probe function  $P(\mathbf{R})$  and real-space specimen transmission function  $\varphi(\mathbf{R})$ .<sup>7,53</sup>

$$\psi(\mathbf{R}, \mathbf{R}_0) = P(\mathbf{R} - \mathbf{R}_0) \varphi(\mathbf{R}) \quad (1.8)$$

where  $\mathbf{R}_0$  refers to the spatial probe position. Electrons emerging from the sample are guided through the image-forming intermediate and projector lens system until they reach the detector in the microdiffraction

plane. In the detector plane, the electron wave is described as a Fourier transform of the exit wave  $\psi(\mathbf{R}, \mathbf{R}_0)$ .<sup>54</sup> Applying the convolution- and Fourier shift theorems, the exit wave can be written as a convolution of two functions.<sup>56</sup>

$$\psi(\mathbf{K}_f, \mathbf{R}_0) = [A(\mathbf{K}_f) \exp(2\pi i \mathbf{K}_f \cdot \mathbf{R}_0)] \otimes \phi(\mathbf{K}_f) \quad (1.9)$$

In contrast to conventionally used integrating detectors, in 4D STEM, DEC's are used that acquire an entire CBED pattern for each probe position. Conventional detectors use only a certain portion of the total electrons incident on the sample at a time, resulting in loss of information. A major advantage of DEC's is that the measured data can be used not only for advanced phase-retrieval techniques, but also for virtual imaging in post-processing analysis. Specific detector masks can be offset against the individual CBEDs with subsequent integration of the signal to obtain a virtual image.<sup>57,58</sup>

As mentioned before, in 4D STEM, an entire CBED pattern is recorded for each probe position during the scan. In the detector plane, it is only possible to record intensities. Thus, only the squared modulus of the electron wave  $|\psi(\mathbf{K}_f, \mathbf{R}_0)|^2$  can be detected. It is impossible to directly access the phase of the electron wave, which contains the specimen-induced phase shift information. However, the phase information is accessible from the overlap of direct and scattered beam discs in periodic structures via in silico processing of 4D STEM datasets. A 4D dataset is schematically illustrated in Figure 6. For each probe position, a 2D diffraction pattern is captured in the detector plane with an intensity of  $|\psi(\mathbf{K}_f, \mathbf{R}_0)|^2$ .

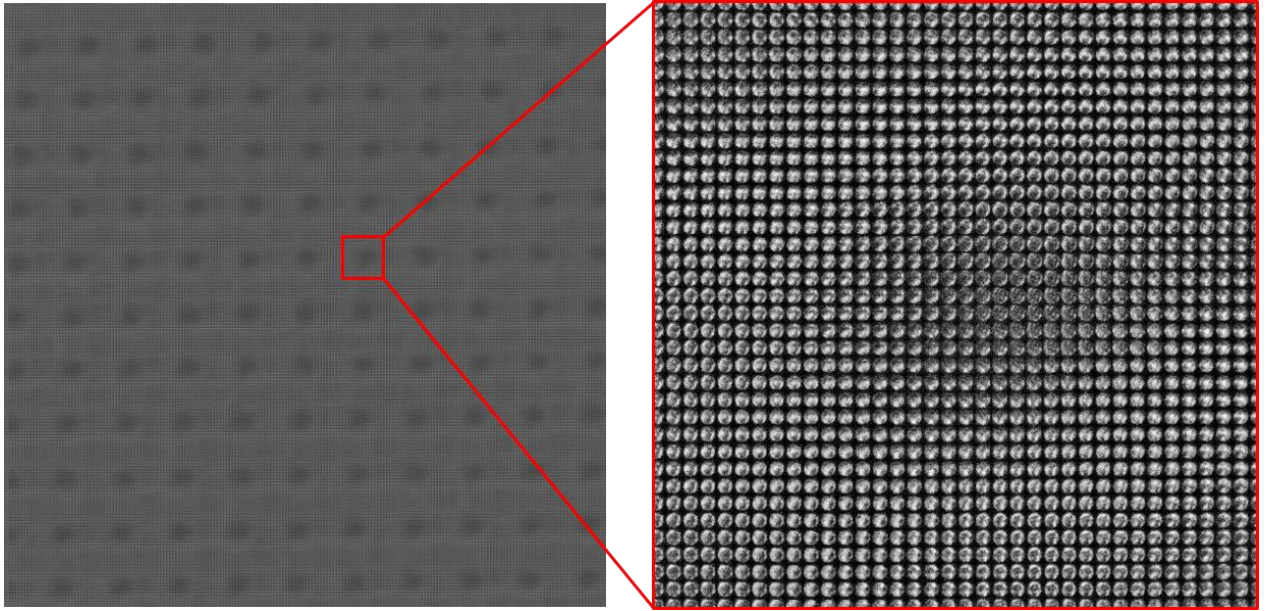


**Figure 6.** 4D STEM dataset. For each probe position in a scan, a 2D diffraction pattern is captured scanning over a periodic structure. 2D diffraction patterns from a sub-area of the structure are shown in the inset.

#### 1.4.2. Fundamentals

The idea of ptychography as a method to solve the phase problem with a coherent source was first introduced by Walter Hoppe in 1969. From a single diffraction pattern consisting of overlapping, interfering diffraction



discs, the phase differences can be determined except for their sign. It is possible to overcome this ambiguity by shifting the beam or the sample to a second position and performing another diffraction experiment and applying the Fourier shift theorem.<sup>59</sup> After Hoppe gave up his initial idea on the grounds that both STEM techniques and detectors were not developed sufficiently in the 1960s, Rodenburg and co-workers developed a method called Wigner Distribution Deconvolution (WDD) in the early 1990s based on Hoppe's initial idea. WDD is a non-iterative method to retrieve the specimen transmission function of a material. Deconvolution of the influences of the microscope imaging system following the phase-object approximation is performed.<sup>54</sup> Based on the weak-phase object approximation, they developed another non-iterative algorithm called single-side-band (SSB) method in 1992 and were able to prove their concepts experimentally.<sup>60</sup> Besides the development of non-iterative algorithms such as WDD and SSB, iterative algorithms were developed more recently in the 2000s. Here, the phase problem is solved by converging from an initial guess to a solution for the object and probe function and matching the intermediate algorithm results with experimental data.<sup>61</sup> However, limitations in computer technology for big-data processing and poor detector quality at that time were the reason why ptychography found little resonance. Widespread interest started in the field of x-ray synchrotron microscopy around 2007.<sup>62</sup> With the development of DEC's which are capable of capturing entire diffraction patterns for each probe position and the possibility for processing big datasets, ptychography is increasingly becoming an important tool for high-resolution, dose-efficient measurements that provide high-contrast images. In this work, SSB and WDD non-iterative algorithms were used to retrieve the electron ptychographic reconstructions of beam-sensitive halide perovskites with moderate and low electron doses.<sup>57,58,63</sup>

Non-iterative phase reconstructions rely on approximations between sample and electron beam to retrieve the phase of the exit wave. WDD assumes the sample is thin enough to behave as a phase-object. This approximation (POA) implies that the presence of a sample, i.e., the atomic potentials will cause a change in the electron wave function only in phase and not amplitude. The specimen transmission function of a phase-object is given in equation (1.10).<sup>7</sup>

$$\varphi_{\text{POA}}(\mathbf{R}) = \exp(-i\sigma V_t(\mathbf{R})) \quad (1.10)$$

with  $\sigma$  as the interaction coefficient that varies with the wavelength of the electrons and  $V_t(\mathbf{R})$  as the projected electrostatic potential of the specimen.

If the material is thin enough, such that  $\sigma V_t(\mathbf{R}) \ll 1$ , the specimen transmission function can be simplified as a linear approximation via the first-degree Taylor polynomial. This approximation, known as weak-phase object approximation (WPOA) is used in the SSB method for phase reconstruction.<sup>7</sup>

$$\varphi_{\text{WPOA}}(\mathbf{R}) \approx 1 - i\sigma V_t(\mathbf{R}) = 1 - i\varphi'(\mathbf{R}) \quad (1.11)$$

Relying on the POA, a multiplicative approach is used to describe the electron wave function exiting the material (equation (1.7)). The recorded intensity in the diffraction plane is given as the squared modulus of

the electron exit wave  $\psi(\mathbf{K}_f, \mathbf{R}_0)$ . To extract the specimen transmission function, the first step in both non-iterative algorithms is to perform a Fourier transform of the whole dataset with respect to the spatial probe position  $\mathbf{R}_0$ . The Fourier transform results in a new complex 4D dataset  $G(\mathbf{K}_f, \mathbf{Q}_0)$ .

$$G(\mathbf{K}_f, \mathbf{Q}_0) = \text{FT}_{\mathbf{R}_0} [|\psi(\mathbf{K}_f, \mathbf{R}_0)|^2] = \text{FT}_{\mathbf{R}_0} [|[A(\mathbf{K}_f) \exp(2\pi i \mathbf{K}_f \cdot \mathbf{R}_0)] \otimes \phi(\mathbf{K}_f)|^2] \quad (1.12)$$

Since the product of a complex number with its complex conjugate is defined as the square of the number's modulus,  $|\psi(\mathbf{K}_f, \mathbf{R}_0)|^2$  can be written as

$$|\psi(\mathbf{K}_f, \mathbf{R}_0)|^2 = \{[A(\mathbf{K}_f) \exp(2\pi i \mathbf{K}_f \cdot \mathbf{R}_0)] \otimes \phi(\mathbf{K}_f)\} \cdot \{[A^*(\mathbf{K}_f) \exp(-2\pi i \mathbf{K}_f \cdot \mathbf{R}_0)] \otimes \phi^*(\mathbf{K}_f)\} \quad (1.13)$$

To simplify equation (1.13), the first step is to apply the convolution theorem.<sup>56</sup>

$$\begin{aligned} |\psi(\mathbf{K}_f, \mathbf{R}_0)|^2 &= \int A(\mathbf{a}) \exp(2\pi i \cdot \mathbf{a} \cdot \mathbf{R}_0) \cdot \phi(\mathbf{K}_f - \mathbf{a}) d\mathbf{a} \\ &\quad \cdot \int A^*(\mathbf{b}) \exp(-2\pi i \cdot \mathbf{b} \cdot \mathbf{R}_0) \cdot \phi^*(\mathbf{K}_f - \mathbf{b}) d\mathbf{b} \\ &= \iint A(\mathbf{a}) A^*(\mathbf{b}) \phi(\mathbf{K}_f - \mathbf{a}) \phi^*(\mathbf{K}_f - \mathbf{b}) \exp(2\pi i \cdot \mathbf{R}_0(\mathbf{a} - \mathbf{b})) d\mathbf{a} d\mathbf{b} \end{aligned} \quad (1.14)$$

with  $\mathbf{a}$  and  $\mathbf{b}$  as dummy variables. A Fourier transform is performed to obtain  $G(\mathbf{K}_f, \mathbf{Q}_0)$ .

$$G(\mathbf{K}_f, \mathbf{Q}_0) = \iiint A(\mathbf{a}) A^*(\mathbf{b}) \phi(\mathbf{K}_f - \mathbf{a}) \phi^*(\mathbf{K}_f - \mathbf{b}) \exp(2\pi i \cdot \mathbf{R}_0(\mathbf{a} - \mathbf{b} + \mathbf{Q}_0)) d\mathbf{a} d\mathbf{b} d\mathbf{R}_0 \quad (1.15)$$

The first integral is solved with a subsequent substitution of  $\mathbf{c} = \mathbf{b} - \mathbf{Q}_0$ .

$$\int \exp(2\pi i \cdot \mathbf{R}_0(\mathbf{a} - \mathbf{b} + \mathbf{Q}_0)) d\mathbf{R}_0 = \delta(\mathbf{a} - \mathbf{b} + \mathbf{Q}_0) \quad (1.16)$$

with  $\delta$  as the Dirac delta function.

$$\begin{aligned} G(\mathbf{K}_f, \mathbf{Q}_0) &= \iint A(\mathbf{a}) A^*(\mathbf{c} + \mathbf{Q}_0) \phi(\mathbf{K}_f - \mathbf{a}) \phi^*(\mathbf{K}_f - \mathbf{c} - \mathbf{Q}_0) \delta(\mathbf{a} - \mathbf{c}) d\mathbf{a} d\mathbf{c} \\ &= \int A(\mathbf{c}) A^*(\mathbf{c} + \mathbf{Q}_0) \phi(\mathbf{K}_f - \mathbf{c}) \phi^*(\mathbf{K}_f - \mathbf{c} - \mathbf{Q}_0) d\mathbf{c} \end{aligned} \quad (1.17)$$

By applying the convolution theorem to equation (1.17),  $G(\mathbf{K}_f, \mathbf{Q}_0)$  is brought to the final form.

$$G(\mathbf{K}_f, \mathbf{Q}_0) = A(\mathbf{K}_f) A^*(\mathbf{K}_f + \mathbf{Q}_0) \otimes \phi(\mathbf{K}_f) \phi^*(\mathbf{K}_f - \mathbf{Q}_0) \quad (1.18)$$

$G(\mathbf{K}_f, \mathbf{Q}_0)$  is a convolution of two functions. The first represents the overlap of two aperture functions separated by  $\mathbf{Q}_0$  and the second represents the overlap of two specimen transmission functions separated by  $\mathbf{Q}_0$ .  $G(\mathbf{K}_f, \mathbf{Q}_0)$  is a function of detector coordinate  $\mathbf{K}_f$  and probe spatial frequency  $\mathbf{Q}_0$ . Under this condition, amplitude and phase are accessible since the equation is free of any squared terms.  $G(\mathbf{K}_f, \mathbf{Q}_0)$  can be interpreted as the Fourier transform of all STEM images generated from the intensities of individual detector pixels during the scan.<sup>57,64</sup> Its nature is illustrated in Figure 7 by summing  $G(\mathbf{K}_f, \mathbf{Q}_0)$  over all  $\mathbf{K}_f$  for all

spatial frequencies and plotting it as a function of  $\mathbf{Q}_0$ . To retrieve the specimen transmission function from the convolution, SSB and WDD are the methods of choice, both introduced in the following paragraphs.

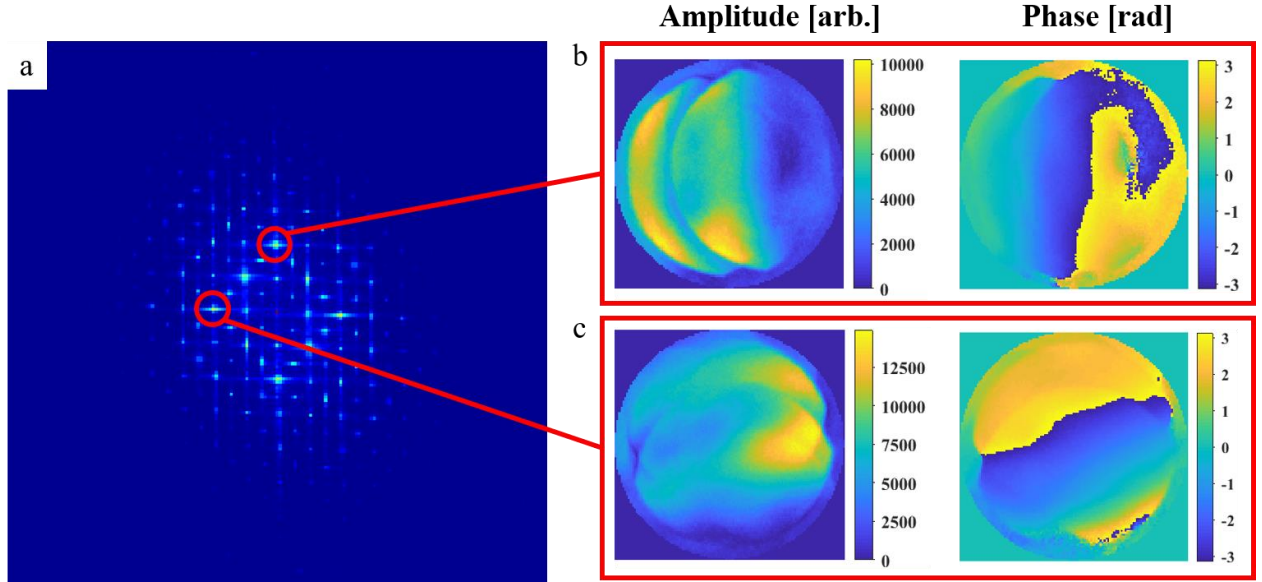


**Figure 7.** (a)  $G(\mathbf{K}_f, \mathbf{Q}_0)$  summed over all detector coordinates  $\mathbf{K}_f$  as a function of  $\mathbf{Q}_0$ . Amplitude in arbitrary units and phase in radians as a function of  $\mathbf{K}_f$  for two different spatial frequencies  $\mathbf{Q}_0$  in (b) and (c).

#### 1.4.2.1 Single-side-band (SSB) reconstruction

As mentioned before, in SSB ptychography, the material is assumed to be thin enough to be approximated as a WPO. The specimen transmission function can be approximated by the linear part of the Taylor expansion if  $\sigma V_t(\mathbf{R})$  is much less than unity. Using the WPOA (1.11),  $G(\mathbf{K}_f, \mathbf{Q}_0)$  can be expressed in the following form:

$$G(\mathbf{K}_f, \mathbf{Q}_0) = |A(\mathbf{K}_f)|^2 \delta(\mathbf{Q}_0) + A(\mathbf{K}_f)A^*(\mathbf{K}_f + \mathbf{Q}_0)\phi'^*(-\mathbf{Q}_0) + A^*(\mathbf{K}_f)A(\mathbf{K}_f - \mathbf{Q}_0)\phi'(\mathbf{Q}_0) \quad (1.19)$$

using an approximation of the transfer function calculated from the Fourier transform (1.11) as

$$\begin{aligned} \phi_{WPOA}(\mathbf{K}_f) &= \delta(\mathbf{K}_f) + \phi'(\mathbf{K}_f) \\ \phi'(\mathbf{K}_f) &= -i\text{FT}_R[\phi'(\mathbf{R})] \end{aligned} \quad (1.20)$$

Equation (1.19) consists of three parts. The first part corresponds to the direct beam and the other two represent two scattered beams located at  $\pm \mathbf{Q}_0$  that interfere with the central disc and also interfere with each other depending on the spatial frequency.<sup>57,60</sup> A graphical representation of the equation is given in Figure 8 for two different spatial frequencies. Due to the constraints imposed by the aperture function, a transfer theoretically occurs only in the regions of double overlap, i.e., in areas where the direct beam overlaps with a scattered beam. Moreover, since  $\phi'(\mathbf{Q}_0) = -\phi'^*(-\mathbf{Q}_0)$ ,  $\phi'(\mathbf{Q}_0)$  and  $\phi'^*(-\mathbf{Q}_0)$  have the same amplitude but are  $\pi$  radians out of phase, i.e., in a region of triple overlap no transfer will take place due to destructive interference.<sup>54</sup>



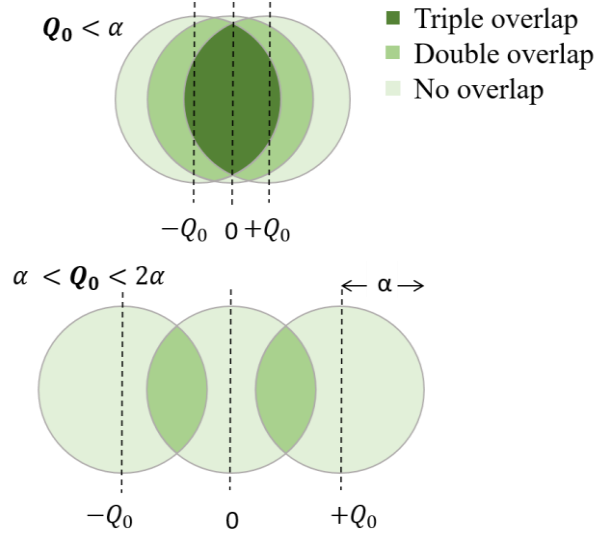


**Figure 8.** Graphical representation of  $G(K_f, Q_0)$  applying the WPOA for a SSB phase reconstruction. The overlap of the central beam centered at  $K_f = 0$  and two scattered beams centered at  $\pm Q_0$  are shown exemplarily for two different spatial frequencies. As the spatial frequency increases, the regions of overlap become smaller until the discs finally separate for  $Q_0 = 2\alpha$ .

For data processing, the amplitudes and phases of  $G(K_f, Q_0)$  are multiplied with masks that set all values outside double overlap regions to zero as illustrated in Figure 9. Non-zero amplitudes and phases in the unfiltered images and inhomogeneities in the side bands are the result of residual aberrations and noise.

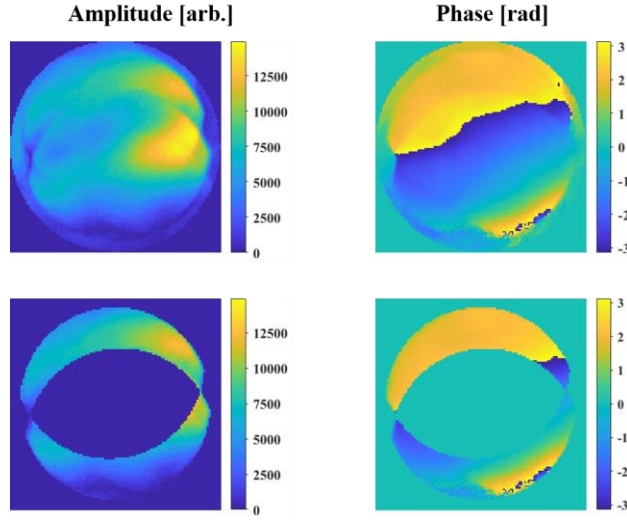


**Figure 9.** Amplitude and phase of  $G(K_f, Q_0)$  for a spatial frequency  $Q_0$  as a function of detector coordinate  $K_f$ . Double overlap regions were cut out by applying a mask that sets all other values to zero.

Relying on the aberration corrector of the electron microscope, the influence of any aberrations was neglected in SSB ptychographic reconstructions in this thesis. In a subsequent processing step, adding  $\pi$  to the phase of one of the double overlaps and summing over all  $K_f$  for any given  $Q_0$  yields  $\phi'(Q_0)$  and a Fourier transform returns the real-space transmission function  $\varphi'(R)$ . With conventional detectors, the transfer limit of spatial frequencies is given by the aperture. With ptychography, resolution beyond the

information limit of the microscope can be achieved.<sup>64</sup> However, modern electron microscopes exceed an information limit of 0.1 nm. Therefore, ptychography is commonly performed using only the bright-field disc information.<sup>63,65,66</sup>

#### 1.4.2.2 Wigner distribution deconvolution (WDD)

Without using the WPOA,  $G(\mathbf{K}_f, \mathbf{Q}_0)$  cannot be simplified any further, and the object function must be separated from the aperture function through deconvolution. An inverse Fourier transform of (1.18) with respect to the detector coordinate  $\mathbf{K}_f$  returns a new 4D dataset  $H(\mathbf{R}, \mathbf{Q}_0)$  that is mathematically devoid of a convolution and of specific character.<sup>54</sup>

$$\begin{aligned} H(\mathbf{R}, \mathbf{Q}_0) &= IFT_{\mathbf{K}_f}[G(\mathbf{K}_f, \mathbf{Q}_0)] \\ &= \int P^*(\mathbf{a})P(\mathbf{a} + \mathbf{R}) \exp(-2\pi i \mathbf{Q}_0 \cdot \mathbf{a}) d\mathbf{a} \cdot \int \varphi^*(\mathbf{b})\varphi(\mathbf{b} + \mathbf{R}) \exp(2\pi i \mathbf{Q}_0 \cdot \mathbf{b}) d\mathbf{b} \end{aligned} \quad (1.21)$$

with probe and transmission functions with respect to the real-space coordinates  $\mathbf{a}$ ,  $\mathbf{b}$  and  $\mathbf{R}$ .

$H(\mathbf{R}, \mathbf{Q}_0)$  can be written as the product of two Wigner distribution functions with

$$\chi_q(x, y) = \int q^*(z)q(z + x) \exp(2\pi i z \cdot y) dz \quad (1.22)$$

as

$$H(\mathbf{R}, \mathbf{Q}_0) = \chi_P(\mathbf{R}, -\mathbf{Q}_0) \cdot \chi_\varphi(\mathbf{R}, \mathbf{Q}_0) \quad (1.23)$$

In this step, the purpose of calculating  $H(\mathbf{R}, \mathbf{Q}_0)$  becomes evident, since all the influences of the microscope transfer function can be divided out of the dataset. To prevent noise amplification and avoid division by zero, a Wiener filter is used and the dataset is transformed as follows:

$$\chi_\varphi(\mathbf{R}, \mathbf{Q}_0) = \frac{\chi_P^*(\mathbf{R}, -\mathbf{Q}_0)H(\mathbf{R}, \mathbf{Q}_0)}{|\chi_P(\mathbf{R}, -\mathbf{Q}_0)|^2 + \epsilon} \quad (1.24)$$

where  $\epsilon$  is a small constant that should be set as the signal-to-noise ratio at each point, but is conventionally chosen as a small fraction of  $|\chi_P(\mathbf{R}, -\mathbf{Q}_0)|^2$ .<sup>65</sup> An  $\epsilon$ -ratio can be defined as

$$\epsilon_{\text{rat}} = \frac{\epsilon}{|\chi_P(\mathbf{R}, -\mathbf{Q}_0)|^2} \quad (1.25)$$

and  $\epsilon_{\text{rat}}$  is usually set between 0.01 and 0.1.<sup>64,65</sup>

Subsequently, to retrieve the object information, another Fourier transform is performed.

$$D(\mathbf{K}_f, \mathbf{Q}_0) = FT_{\mathbf{K}_f}[\chi_\varphi(\mathbf{R}, \mathbf{Q}_0)] = \phi(\mathbf{K}_f)\phi^*(\mathbf{K}_f - \mathbf{Q}_0) \quad (1.26)$$

Slicing through this dataset at a spatial frequency of  $\mathbf{K}_f = 0$  leads to the solution of  $\phi(\mathbf{Q}_0)$  as

$$\phi(\mathbf{Q}_0) = \frac{D^*(\mathbf{0}, \mathbf{Q}_0)}{\sqrt{D(\mathbf{0}, \mathbf{0})}} \quad (1.27)$$

and a simple inverse Fourier transform returns  $\varphi(\mathbf{R})$ .<sup>54</sup> WDD ptychographic reconstructions were performed relying on the aberration corrector of the electron microscope. The influence of any residual aberrations was neglected in this work.

## 2. Materials and Methods

### 2.1. Sample preparation

Due to the extreme sensitivity of HP materials towards high-energy irradiation, sample preparation via top-down processes, e.g., with a focused ion beam (FIB), cannot be considered for the preparation of thin TEM samples. A focused gallium ion beam alters the native structure of HPs, and FIB-prepared specimens are not representative of the structures of the photoactive materials.<sup>49</sup> Alternatives such as ultramicrotomy, ion milling, electropolishing, etc. are also not an option for TEM sample fabrication due to the extreme sensitivity of HPs to air exposure and moisture. Therefore, all samples investigated in this study were prepared from bottom-up solution processes in an argon atmosphere either directly on the TEM grids by drop-casting, spin coating, and annealing or as nanocrystals dispersed in a solvent and subsequently drop-casted on the grid. Prior to sample deposition, all grids were cleaned with a PELCO easiGlow<sup>TM</sup> glow discharge device using a current of 15  $\mu$ A for 45 s.

#### 2.1.1. CsPbBr<sub>3</sub> nanocrystals

To synthesize CsPbBr<sub>3</sub> nanocrystals, a Cs-oleate solution was prepared from Cs<sub>2</sub>CO<sub>3</sub>, oleic acid (OA) and 1-octadecene (ODE) in a first step. 0.75 g of Cs<sub>2</sub>CO<sub>3</sub> (2.3 mmol), 3.0 mL OA (9.51 mmol), and 75 mL ODE were heated to 120 °C under vacuum conditions. After 2 h, the reaction product was cooled down to room temperature and stored in an argon atmosphere after backfilling with argon for further use. Subsequently, 1 g of PbBr<sub>2</sub> (2.17 mmol) was heated with 50 mL of ODE to 120 °C under vacuum conditions. 5 mL of OA and 5 mL of oleylamine (OLA) were preheated to 70 °C and added to the mixture. After complete solubilization of PbBr<sub>2</sub> under vacuum conditions, the temperature was raised to the injection temperature of 160 °C. 4 mL of the preheated Cs-oleate precursor were injected quickly into the reaction mixture. After 10 s, the mixture was cooled down to room temperature in an ice-water bath. To isolate the nanocrystals, the mixture was centrifuged with methyl acetate (MeOAc) (with a mixture : MeOAc ratio of 1:1.1) for 10 min at 8800 rpm. The precipitate was dispersed in 6 mL of n-Hexane and the last step was repeated. Finally, the product was dispersed in 10 mL of toluene to remove excess PbBr<sub>2</sub> and Cs-oleate. The nanocrystal dispersion was stored in the dark in a refrigerator. For TEM investigations, 10  $\mu$ L of the nanocrystal dispersion was drop-cast on a copper grid coated with a lacey carbon film as sample support. The solvent was evaporated by heating the sample for 1 min on a heating plate at 110 °C.

#### 2.1.2. CsPbIBr<sub>2</sub> thin films

In a first step, a 0.5 M precursor solution was prepared by mixing 0.26 g CsI and 0.37 g PbBr<sub>2</sub> with 2 mL dimethylsulfoxide (DMSO) in an argon atmosphere. The solution was stirred for 30 min at room temperature and filtered with a syringe filter to remove any undissolved solid precursors. For thin film preparation, the TEM grid was fixed on a sapphire substrate with polyimide tape. The grid substrate was preheated on a

heating plate to 60 °C for 3 min. The preheated grid was spin-coated with 20  $\mu\text{L}$  of the precursor solution (4980 rpm for 30 s) and subsequently annealed at 280 °C for 30 s. A color change was observed from initially yellow to dark red after a few seconds. The grid was removed from the sapphire again for TEM investigations.

### **2.1.3. CsPbI<sub>3</sub> thin films**

For the preparation of CsPbI<sub>3</sub> TEM samples, a 0.5 M precursor solution was prepared by mixing stoichiometric amounts of CsI and PbI<sub>2</sub> with DMSO. The solution was stirred for 30 min at room temperature and subsequently filtered by a syringe filter to remove any undissolved solid precursor. Plasma cleaned holey carbon copper grids were heated to 350 °C on a filter paper on a heating plate and 10  $\mu\text{L}$  of the precursor solution were drop-cast. After 10 s of annealing during which a color change from yellow to black was observed, the grid was cooled down to room temperature. The entire sample preparation process was conducted in an argon atmosphere.

## **2.2. STEM investigations**

STEM investigations were carried out using a JEOL JEM-ARM200F STEM equipped with a cold field-emission gun and a probe C<sub>s</sub>-corrector (DCOR, CEOS GmbH). Measurements were performed at ambient temperatures with an acceleration voltage of 200 kV. Conventional images were captured with a Gatan ADF detector using small spot sizes of 8 C and 10 C in the experimental setting. ADF images were captured with a camera length of 2 cm. Depending on the aperture, a probe with a semi-convergence angle of 14.4 mrad (20  $\mu\text{m}$  condenser lens aperture) or 20.4 mrad (30  $\mu\text{m}$  condenser lens aperture) was used to capture the data. EELS acquisition was performed using a Gatan GIF Quantum ERS imaging filter with an entrance aperture of 5 mm and a camera length of 1.5 cm, resulting in a collection semi-angle of 111 mrad. The sample thickness was estimated from dual EELS measurements of low-loss and high-loss spectra. XEDS measurements were performed using a 100 mm<sup>2</sup> JEOL Centurio SSD-EDS detector positioned above the sample. 4D STEM data was captured using a MerlinEM Medipix3 detector by Quantum Detectors. A camera length of 40 cm and a probe semi-convergence angle of 20.4 mrad (CsPbBr<sub>3</sub>) and 14.4 mrad (CsPbIBr<sub>2</sub>, CsPbI<sub>3</sub>) were used. The detector was operated in 1-bit mode, allowing a maximum detection of one electron per detector pixel in one frame. With this detector setup, dead-time free detection was achieved with the fastest frame time of 48  $\mu\text{s}$ .

## **2.3. 4D STEM data processing**

Ptychographic reconstructions were performed with an open-source repository of MATLAB scripts called ptychoSTEM available on GitLab.<sup>57,58,63</sup> 4D STEM datasets were initially loaded into a 4D array in MATLAB. With probe step size, electron wavelength and convergence semi-angle sample- and detector plane were calibrated. For virtual imaging, a variety of detector masks were applied to the datasets. For phase reconstructions, the 4D STEM data was truncated to extract only the bright-field discs. After

performing the Fourier transform with respect to the probe position  $\mathbf{R}_0$ , the power spectrum of  $G(\mathbf{K}_f, \mathbf{Q}_0)$  was used to verify the correct calibration of the real and reciprocal space (Figure 7). For SSB ptychography, double overlap regions were extracted,  $\pi$  was added to the phase of one side band and by summation with a subsequent Fourier transform, the specimen transmission function was obtained assuming zero lens aberrations. WDD was performed following the deconvolution and reconstruction procedure described in section 1.4.2.2 assuming no lens aberration effects.

## 2.4. Electron dose measurements

Since the ARM-DCOR microscope was not equipped with a Faraday cup to directly measure the beam current, the CCD camera located at the end of the Gatan Imaging Filter (GIF) was calibrated. The drift tube of the GIF is equipped with a built-in picoammeter able to detect any current falling on the drift tube inside the prism. By setting a wrong primary voltage (30 kV instead of 200 kV) in the quantum filter control window, the beam was deflected to hit the wall of the drift tube. The beam currents were measured for different spot sizes and apertures to calibrate the CCD camera for the incident electrons. The dose was then calculated for each image or 4D STEM dataset individually.

### 3. Results

#### 3.1. Electron dose measurements

The electron dose was estimated by calibrating the average CCD camera counts per electron incident on the detector. The beam current was measured for different spot sizes and two different apertures, and CCD images of the electron beam were subsequently acquired. For each measurement, six CCD camera images were acquired for six current measurements. The conversion factor (CF) of CCD camera counts to incident electrons was calculated using equation (3.1) and an error propagation calculation was performed.

$$CF = \frac{C \cdot e}{I_m \cdot t_1} \quad (3.1)$$

with  $C$  = CCD counts,  $e$  = elemental charge,  $I_m$  = measured current and  $t_1$  = acquisition time CCD.

A dark-current measurement was performed for each spot size to ensure that no charge accumulation was present. Measured dark currents in the range of 1 pA were subtracted from the measured current for each spot size. The CCD camera signal was extracted for each image in a region slightly larger than the actual aperture diameter to include all electrons even from the blurry aperture edges. The signal was integrated over a region containing all pixels with a signal greater than 0.1 % of the inner disc signal (see Figure 10). The conversion factors calculated for different combinations of spot sizes and apertures are listed in Table 1. In this work, it was not possible to use the built-in picoammeter tool for direct current measurements. The low-dose studies of HPs were performed with beam currents in the range or even below the measured dark currents. In this case, the exposure time of the CCD camera was extended to a few seconds.

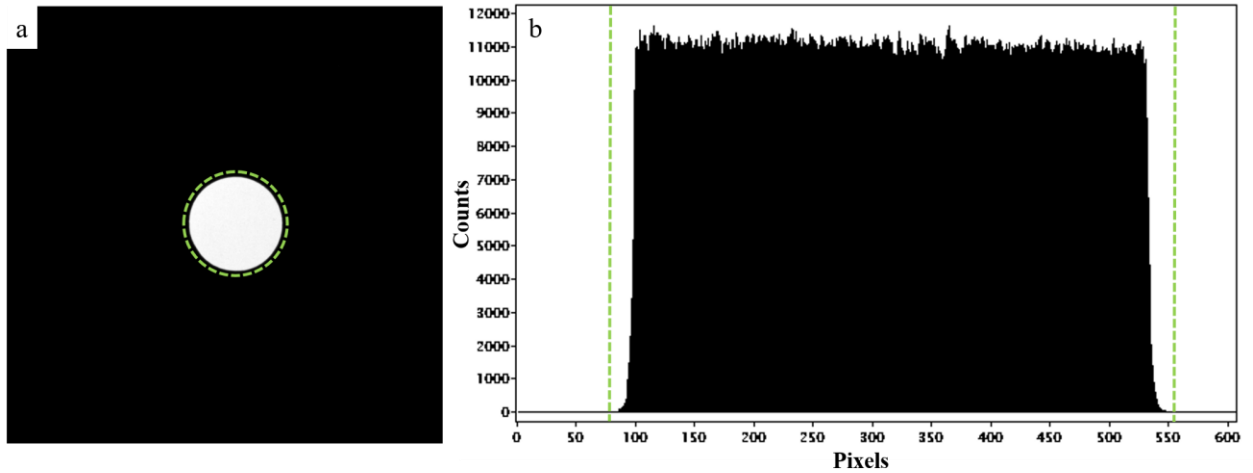


**Figure 10.** (a) Selected area for signal integration to determine the CCD camera counts, exemplified for a spot size of 2C. (b) Signals are integrated over areas with a signal greater than 0.1 % of the average signal.

The average conversion factor was calculated as  $8.02 \pm 0.05$  counts per electron. For dose calculations, CCD images were captured right after the measurements to estimate the electron dose according to equation (3.2).

$$\text{Dose} [e^-/\text{\AA}^2] = \frac{C \cdot t_2}{CF \cdot t_1 \cdot s} \quad (3.2)$$

with  $t_2$  = data acquisition time and  $s$  = image size in  $\text{\AA}^2$ .

**Table 1.** Beam current and corresponding counts measured by the CCD camera for different spot sizes and apertures. A conversion factor for the counts per electron was calculated for each combination.

Spot Size	Aperture	Emission current [ $\mu\text{A}$ ]	Measured current [pA]	CCD counts $\cdot 10^9$	Exposure time[s]	Conversion factor
2C	30 $\mu\text{m}$	13.9 - 13.6	$333.3 \pm 1.7$	$1.6841 \pm 0.0990$	0.1	$8.10 \pm 0.06$
2C	20 $\mu\text{m}$	13.4 - 13.3	$163.0 \pm 0.8$	$0.8194 \pm 0.0395$	0.1	$8.05 \pm 0.08$
3C	30 $\mu\text{m}$	13.1 - 13.0	$255.3 \pm 1.9$	$2.5426 \pm 0.0243$	0.2	$7.96 \pm 0.09$
3C	20 $\mu\text{m}$	12.9 - 12.8	$125.7 \pm 1.5$	$1.2516 \pm 0.0083$	0.2	$7.94 \pm 0.12$
4C	30 $\mu\text{m}$	12.7 - 12.6	$153.4 \pm 1.3$	$3.0837 \pm 0.0163$	0.4	$8.05 \pm 0.08$
4C	20 $\mu\text{m}$	12.5 - 12.4	$76.1 \pm 0.8$	$1.5395 \pm 0.0106$	0.4	$8.10 \pm 0.10$
5C	30 $\mu\text{m}$	12.3 - 12.3	$70.2 \pm 1.2$	$1.7676 \pm 0.0136$	0.5	$8.06 \pm 0.15$
5C	20 $\mu\text{m}$	12.1 - 12.1	$36.1 \pm 0.5$	$0.8847 \pm 0.0051$	0.5	$7.91 \pm 0.25$

### 3.2. CsPbBr<sub>3</sub>

CsPbBr<sub>3</sub> nanocrystals with different morphologies were observed in the sample. Figure 11 shows two examples with corresponding atomic structures. Both, nanowire and nanoplatelet morphologies exhibit an orthorhombic structure and belong to the Pnma space group ( $\gamma$ -CsPbBr<sub>3</sub>).

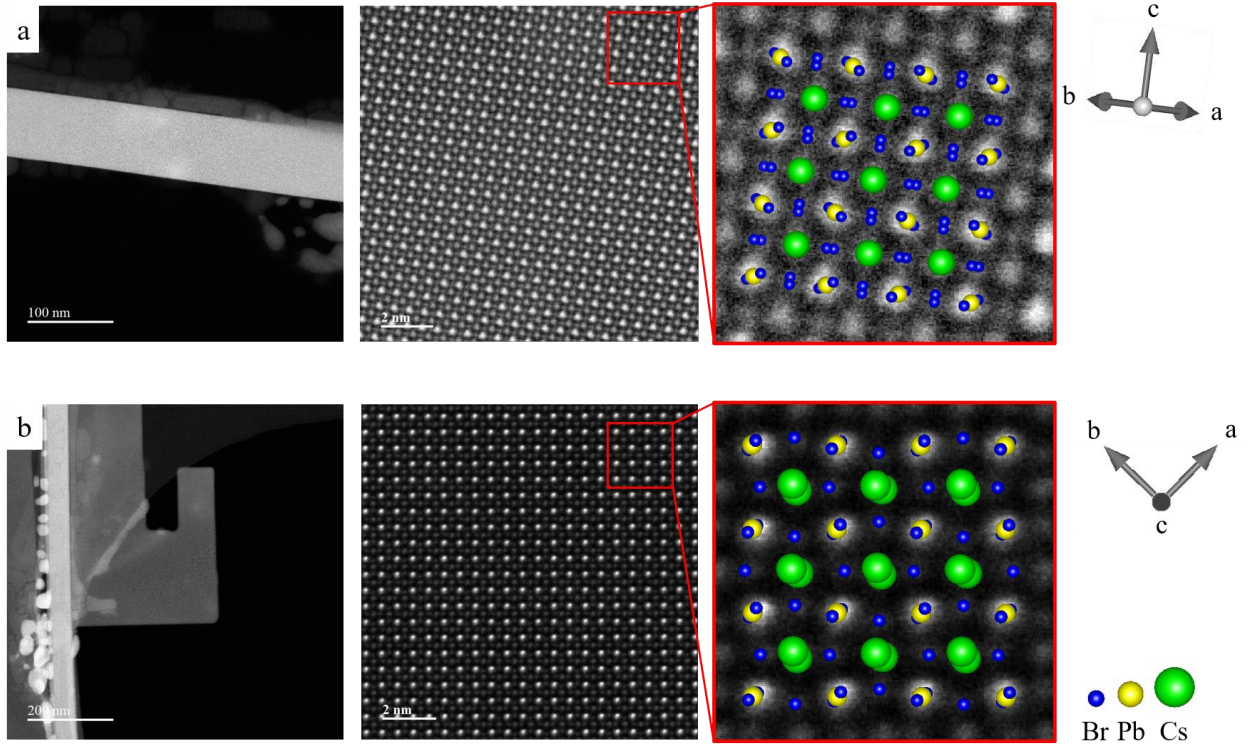


**Figure 11.** ADF images of  $\gamma$ -CsPbBr<sub>3</sub>. (a) Nanowire oriented along the [110] crystallographic direction. (b) Nanoplatelet oriented along the [001] crystallographic direction.

Due to thickness effects, structure images of the thicker nanowires have a lower signal-to-noise ratio and appear more blurry than images of thin nanoplatelets. Therefore, 4D STEM datasets of thin nanoplatelet morphologies were captured to reduce thickness influences on the measurements and enable the application

of the WPOA with better accuracy. The platelet studied here had a thickness of  $\sim 9$  nm. Figure 12 shows a sub-area from which a 4D STEM dataset was recorded. A CBED pattern was recorded for each of the  $400 \times 400$  probe positions. By summing all CBEDs for all probe positions, a position-averaged CBED (PACBED) is generated. With a convergence angle of 20.4 mrad, which corresponds to the bright-field disc radius, CBED patterns were captured within a collection angle of  $\sim 50.2$  mrad. To enable fast data acquisition, the datasets were acquired in 1-bit mode. This mode allowed a zero dead-time acquisition with a frame time of 48  $\mu$ s, resulting in a total acquisition time of  $\sim 7.7$  s for the entire dataset.

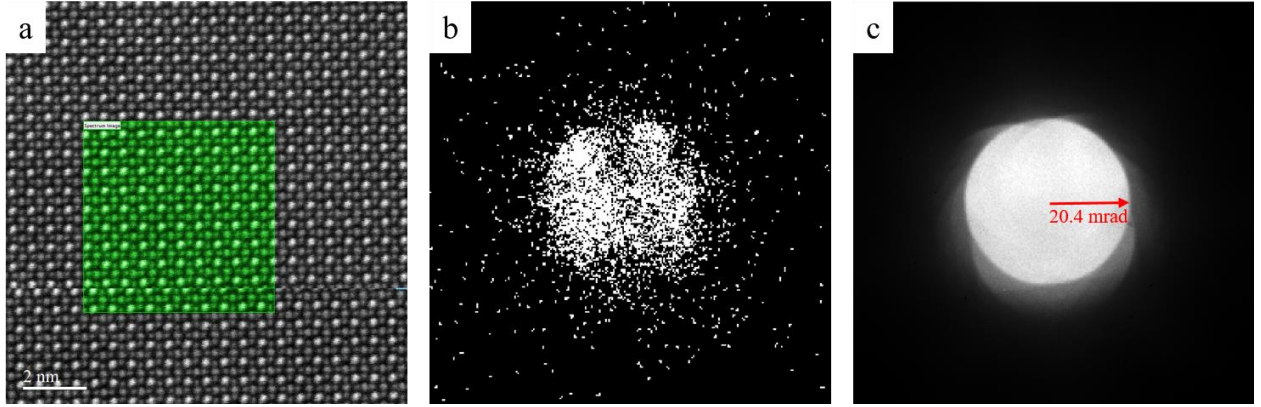


**Figure 12.** (a) Sub-region of  $\gamma$ -CsPbBr<sub>3</sub> from which  $400 \times 400$  CBEDs were captured. (b) Single CBED pattern recorded by the direct electron camera in 1-bit mode. (c) PACBED as a sum of all CBEDs for all probe positions in the scan.

With ADF detectors that can only capture a certain convergence angle (83-205 mrad for Figure 11), it is difficult to find proper adjustments to capture high-contrast images for atoms of different atomic weights. From a 4D STEM dataset, images of all possible detector geometries can be obtained in a post-acquisition step by applying specific masks. All intensity values from undesired scattering angles are set to zero and an image is generated by integrating the residual signal for all probe positions. Three example detector geometries commonly used for STEM imaging are illustrated in Figure 13.



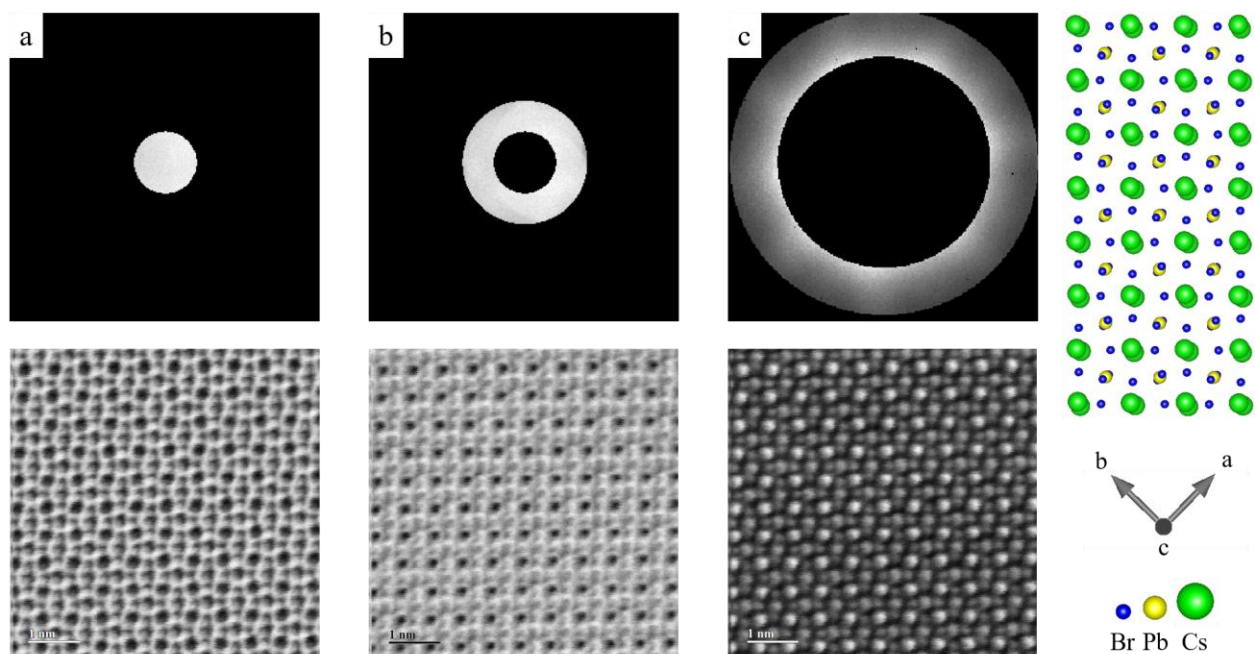


**Figure 13.** Synthetic STEM images calculated by applying detector masks. (a) BF image using a mask that includes scattering angles of 0–10.2 mrad, (b) ABF image using a mask that includes scattering angles of 10.2–20.4 mrad and (c) ADF image using a mask that includes scattering angles of 34.9–50.2 mrad.

For BF images a fraction of unscattered electrons or electrons scattered to very low angles is captured. Therefore, atomic columns appear dark in bright-field images. For DF images, scattered electrons are detected and atomic columns appear bright. The heavier the atom is, the higher the average scattering angle and the higher the intensity in DF images or lower in BF images respectively. It is therefore possible to distinguish different elements from STEM image intensities. However, STEM images represent a 2D representation of a 3D structure. If the atomic columns of different elements are projected to the same position, a distinction based on image intensities is no longer easily possible. In this case, spectroscopic methods such as EELS are used to extract elemental data. For elemental mapping, the energy-loss characteristic of each element expected in the sample was selected and extracted from an 80×108 pixels spectrum image (SI). Each pixel contains an EEL spectrum acquired for 0.0098 s captured with a probe size of 6C, a probe convergence angle of 20.4 mrad, and a camera length of 1.5 cm. EELS SI analysis was carried out with a 5 mm filter entrance aperture over an energy loss range of 780–2535 eV. A principal component analysis (PCA) filter was used to remove noise from the SI including 10 principal components. The elemental maps reveal the overlap of Pb atomic columns with a fraction of Br columns. Due to the low signal-to-noise ratio for the Pb edge, which is located at a high energy loss, the Pb columns are poorly visible in the elemental maps as shown in Figure 14.

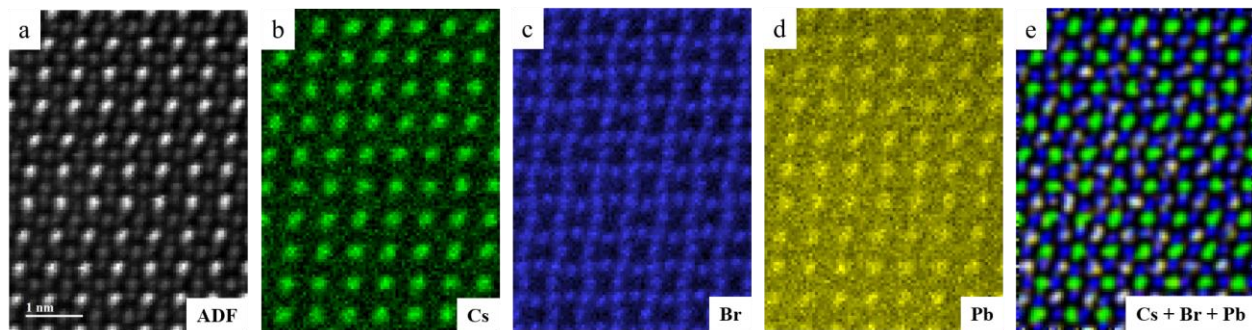


**Figure 14.** Elemental mapping of  $\gamma$ -CsPbBr<sub>3</sub> along [001]. (a) Simultaneously acquired ADF image, (b) extracted signal for the Cs M<sub>4,5</sub> edge, (c) extracted signal for the Br L<sub>2,3</sub> edge, (d) extracted signal for the Pb M<sub>4,5</sub> edge and (e) colorized map using the color scheme from (b-d).

From the same datasets used for synthetic images, ptychographic reconstructions were performed according to the scheme presented in sections 1.4.2.1 and 1.4.2.2. The results of the phase reconstructions are shown in Figure 15. SSB and WDD ptychography reveal a strong contrast for all element species, regardless of their atomic number. Furthermore, due to the improved signal-to-noise ratio (SNR), features of the structure that were previously invisible are revealed. Horizontally and vertically overlapping Cs columns are distinguishable. Moreover, it is also apparent that the sample is somewhat tilted off zone axis due to the slight distortion of atomic columns in one direction (visible especially for Br columns). The effect of the overlapping lead and bromine atoms is more apparent in the phase image, although again they are not directly distinguishable.

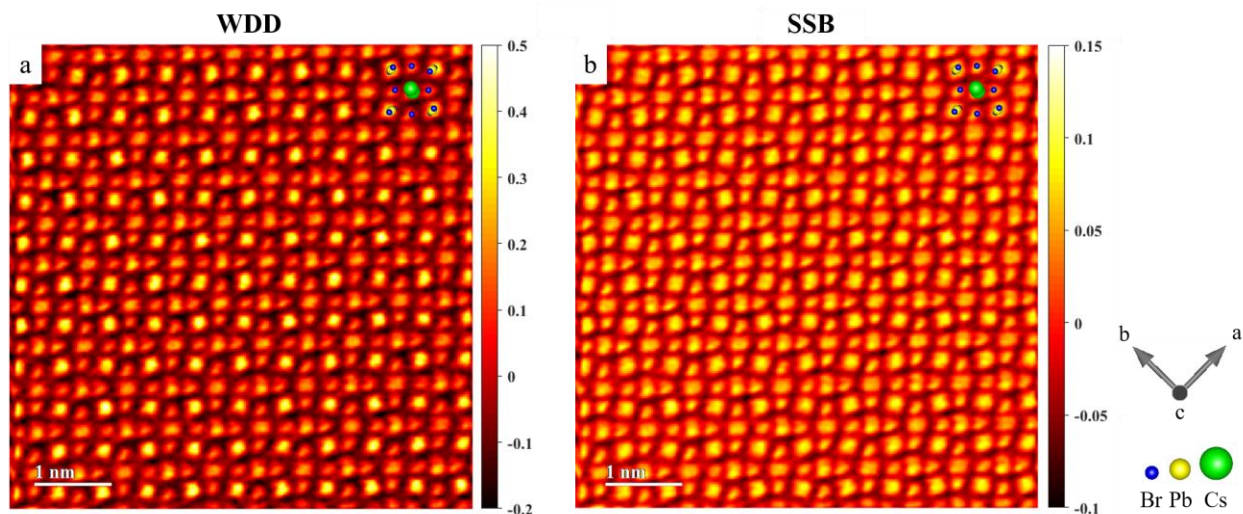


**Figure 15.** Reconstructed phase in unit of radian of  $\gamma$ -CsPbBr<sub>3</sub> along the [001] direction. (a) WDD and (b) SSB ptychography. In both cases, residual aberrations were neglected for image reconstruction.

In general, the atomic columns in phase-reconstructed images as well as in synthetic images are slightly distorted due to sample drift during data acquisition. The minimum pixel time for 4D STEM data acquisition was 48  $\mu$ s in the 1-bit mode. For conventional ADF images, this problem was circumvented by recording 10 frames with shorter pixel time (2  $\mu$ s) followed by drift correction and summation instead of capturing



one image with a pixel time of 20  $\mu$ s. A major advantage of the multi-frame acquisition is that artifacts caused e.g., by environmental effects such as ground vibrations can be averaged or removed by excluding affected frames. Due to the long minimum pixel time for 4D STEM, multi-frame acquisition was not considered as an option here. Since the  $\gamma$ -CsPbBr<sub>3</sub> nanoplatelet was relatively stable under electron beam illumination, all measurements were performed with conventional doses. Changes in the structure were only observed after prolonged illumination. Figure 16 (a-c) shows damaged structures of a different sample area. For long illumination with a high dose, the formation and growth of Pb nanoparticle precipitates was observed. Upon further irradiation, the precipitates grew and voids in the host lattice formed around the bright-contrast Pb nanoparticles, leading to the dismantling of the host lattice. It was observed that the formation of nanoparticles started preferentially at the corners and edges of the surface. Figure 16 (d-f) shows the nanoplatelet after conventional imaging and 4D STEM with an intact host lattice and barely visible radiation damage.

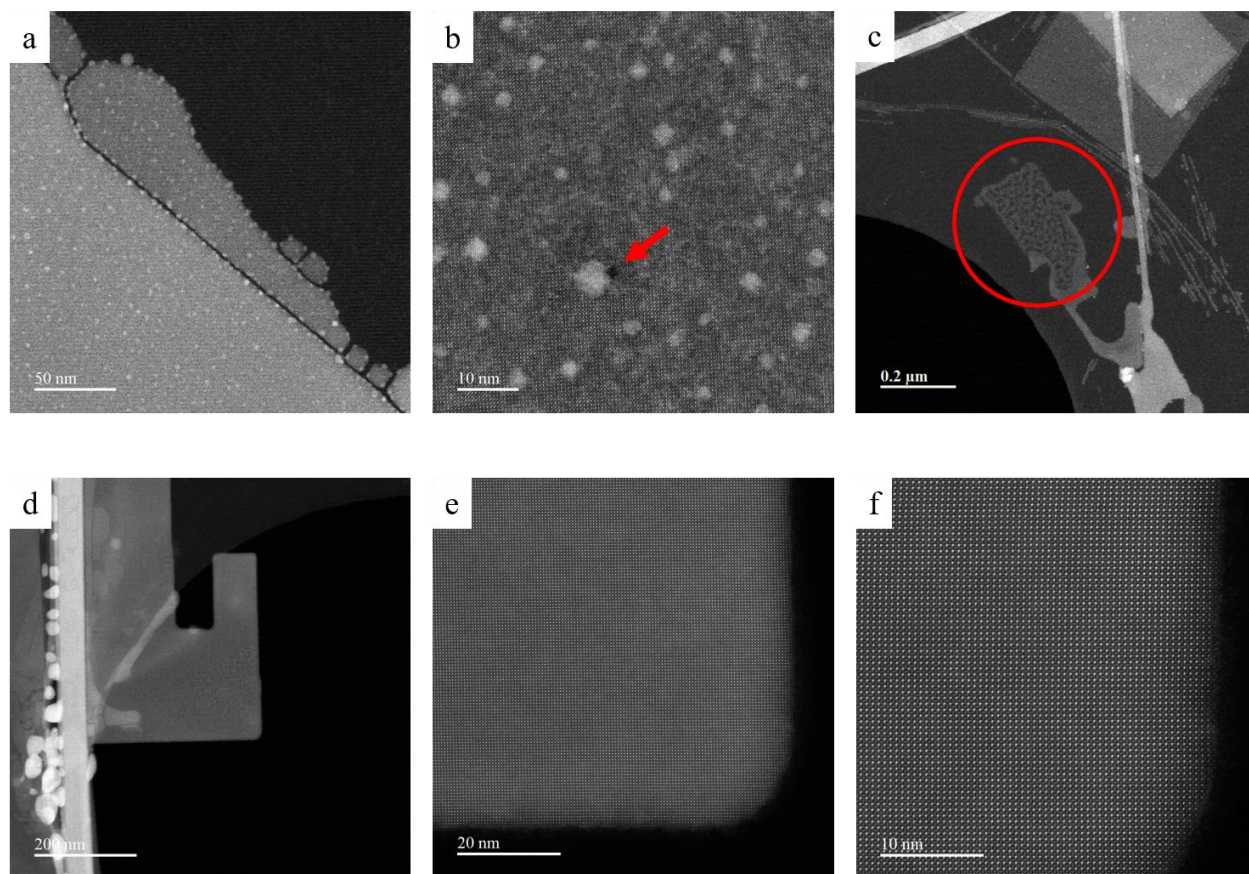


**Figure 16.** (a) ADF images of bright-contrast precipitates due to beam damage after irradiation with high electron doses pronounced at corners and edges. (b) Void formation in the host lattice upon precipitate growth, indicated by a red arrow leading to (c) dismantling of the host lattice (red circle). (d-f) Nanoplatelet after imaging with moderate doses with almost no beam damage visible.

### 3.3. CsPbIBr<sub>2</sub>

CsPbIBr<sub>2</sub> samples were prepared directly on the TEM grid as thin films by drop-casting and spin coating. The samples were extremely sensitive to radiation under conventional imaging conditions. Radiation damage occurred after only a few scans at high magnification. Therefore, the beam dose was drastically reduced to preserve the undamaged structure. Instead of the 30- $\mu\text{m}$  aperture, a 20- $\mu\text{m}$  aperture was used, reducing the beam convergence angle to 14.4 mrad. In addition, all images were captured with the smallest available spot size of 10 C. The electron gun emission current was reduced from 15  $\mu\text{A}$  to  $<5 \mu\text{A}$ , to less than 1/3 of the usual value. Figure 17 shows images of the atomic structure acquired with an ADF detector spanning scattering angles between 83 and 205 mrad.

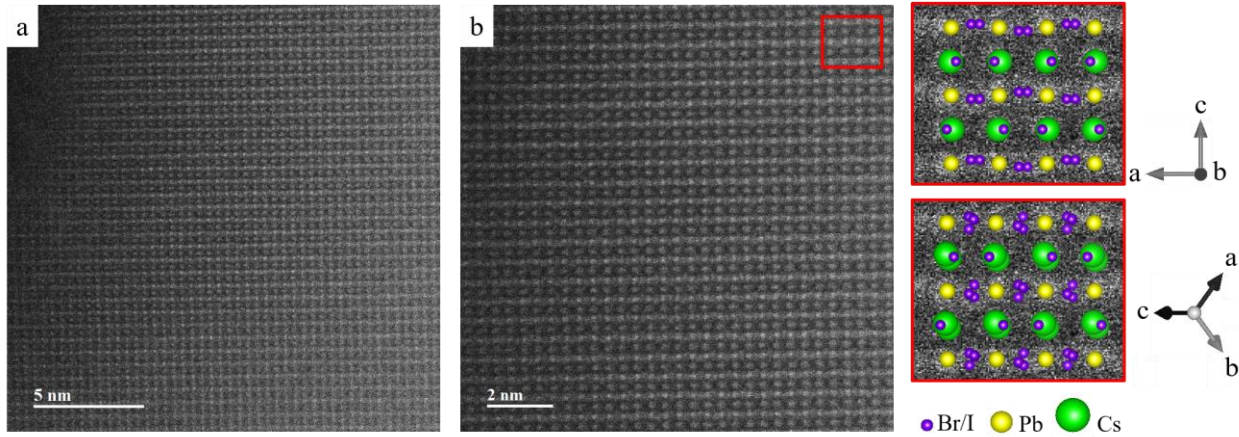


**Figure 17.** ADF images of the atomic structure of CsPbIBr<sub>2</sub>. (a) Image, captured with a low electron dose of  $\sim 560 \text{ e}^-/\text{\AA}^2$  and (b) a dose of  $\sim 1275 \text{ e}^-/\text{\AA}^2$ . Insets in (b) show possible structural orientations.

Due to the poor SNR in the ADF images, it is unclear which atomic orientation is present. However, it can be concluded that CsPbIBr<sub>2</sub> is present in its photoactive  $\gamma$ -CsPbIBr<sub>3</sub> polymorph.  $\gamma$ -CsPbIBr<sub>3</sub> has an orthorhombic structure. 4D STEM datasets were acquired at low doses using the DEC. Due to the different approach for electron detection, a better SNR was expected, especially for low-dose measurements. Datasets were acquired for  $500 \times 500$  probe positions and each CBED was captured within a collection angle of  $\sim 92.2$  mrad. Due to the high magnification and relatively slow scanning speed, a dose of  $\sim 4070 \text{ e}^-/\text{\AA}^2$  was used to record the dataset. The electron beam current was calculated as 0.2 pA from the CCD image. The synthetic images calculated for three different detector geometries are shown in Figure 18.



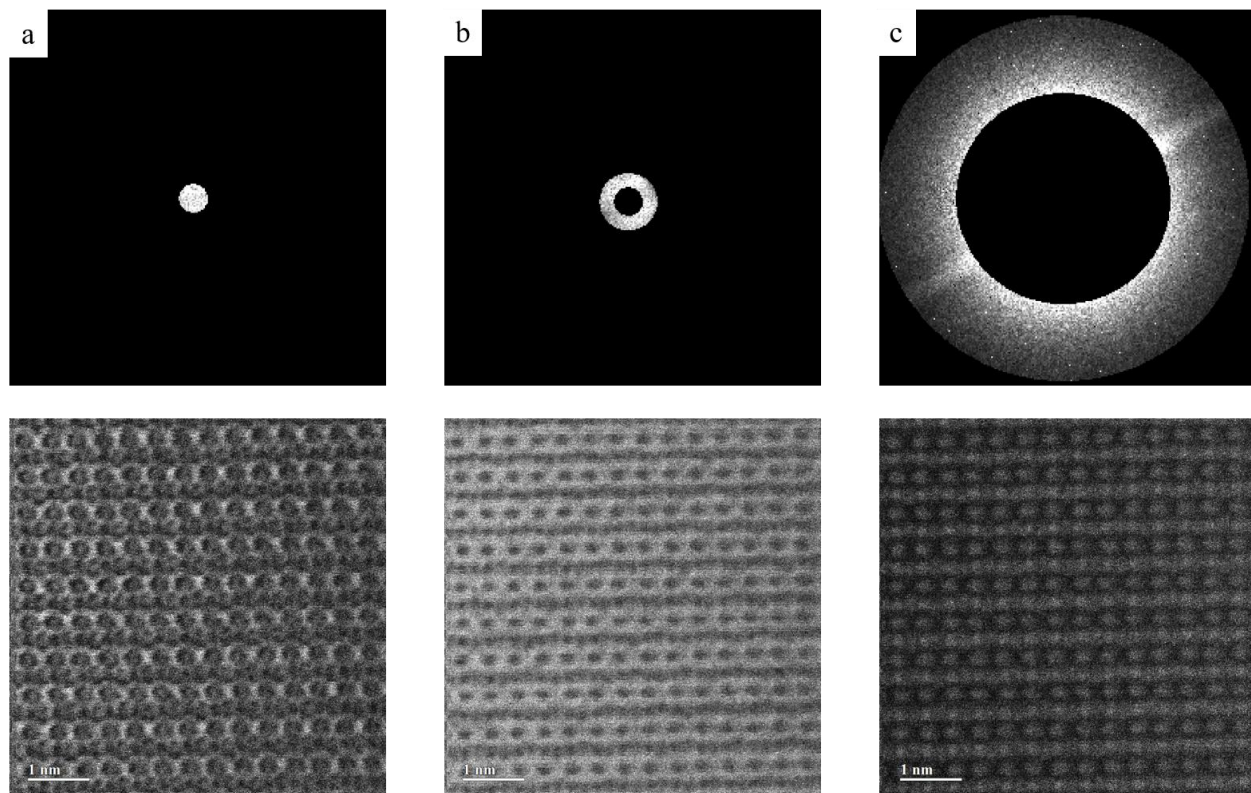


**Figure 18.** Synthetic STEM images of  $\gamma$ -CsPbIBr<sub>2</sub> calculated by applying detector masks. (a) BF image from a mask that includes scattering angles of 0–7.2 mrad, (b) ABF image using a mask that includes scattering angles of 7.2–14.4 mrad and (c) ADF image calculated from a mask that includes scattering angles of 53.3–92.2 mrad.

No clear conclusions about the structural orientation can be drawn from the synthetic images either. To map the atomic structure of the undamaged AIHP, SSB and WDD reconstructions were performed on the same dataset used to generate the synthetic images. The results are shown in Figure 19.

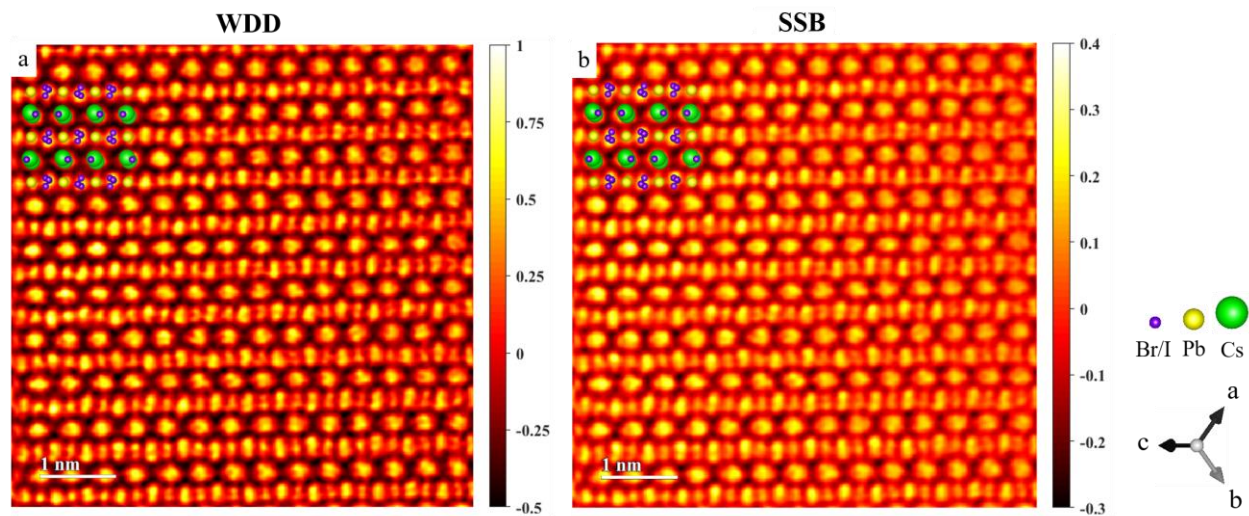


**Figure 19.** Reconstructed phase in unit of radian of  $\gamma$ -CsPbIBr<sub>2</sub> along the [111] direction. (a) WDD and (b) SSB ptychography. In both cases residual aberrations were neglected for image reconstruction.

From the phase-reconstructed images, the actual atomic orientation is evident. The  $\gamma$ -CsPbIBr<sub>2</sub> crystals are oriented along the crystallographic [111] direction. The nature of Br/I atomic columns and their orientation in the lattice are visible. The phase-reconstructed images show high contrast for all atomic species. The effect of sample thickness on the methods is particularly evident from the reconstructions of  $\gamma$ -CsPbIBr<sub>2</sub>. As the sample thickness increases from left to right (~17 nm to ~22 nm), the atomic structures evident from the phase reconstructions appear to become increasingly blurred and indistinct. With increasing thickness, dynamical scattering effects can no longer be neglected, and the multiplicative approximation for the exit wave is no longer valid. WPOA and POA for SSB and WDD reconstructions approach the limit of their applicability, and the reconstructed phase image no longer shows a clear atomic structure. This effect is more pronounced for SSB ptychography, since the linear approximation to the specimen transmission function in the WPOA applies only to really thin materials.

Initially, it was unclear whether the iodine substitution in  $\gamma$ -CsPbIBr<sub>2</sub> would lead to phase separation or nanodomain formation of CsPbBr<sub>3</sub> and CsPbI<sub>3</sub> regions or to a randomly mixed solid solution. Since a uniform intensity distribution was observed for the Br/I columns in the ADF and phase-reconstructed images, it appears that random bromine ions were substituted by iodine ions in the lattice. No phase segregation or formation of nanodomains is expected, as also suggested by Zhou et al. for a similarly prepared sample of  $\gamma$ -CsPbIBr<sub>2</sub>.<sup>44</sup> EELS measurements were performed to obtain elemental maps of Cs, Br and I. The electron dose was increased to a level sufficient to obtain a significant signal of the respective elements. Unfortunately, the dose was not high enough to obtain a sufficient signal-to-background ratio for the Pb peak at high energy loss. However, by increasing the radiation dose, substantial structural damage was taken into account. For elemental mapping, the energy-loss characteristics of Cs, Br, and I were selected and extracted from a 120×149 pixel spectrum image (SI). Each pixel contains an EEL spectrum acquired for 0.0098 s with a probe size of 8 C, a probe convergence angle of 20.4 mrad and a camera length of 1.5 cm. EELS SI analysis was carried out with a 5 mm filter entrance aperture over an energy loss range of 550 to 2600 eV. Since a comparatively low electron dose was used for spectroscopic measurements, the signal-to-background ratio was relatively poor. The use of PCA filters in this case can lead to serious artifacts.<sup>67</sup> To improve the signal-to-background ratio and to rely on the interpretation of raw data, an in-house written tool was used. The tool selects repetitive features, i.e., specific atomic columns within a defined frame. The signal is extracted for all frames and subsequently summed into a stack from which the elemental maps are extracted. Figure 20 shows elemental mappings of stacks from different repeating features in the structure.

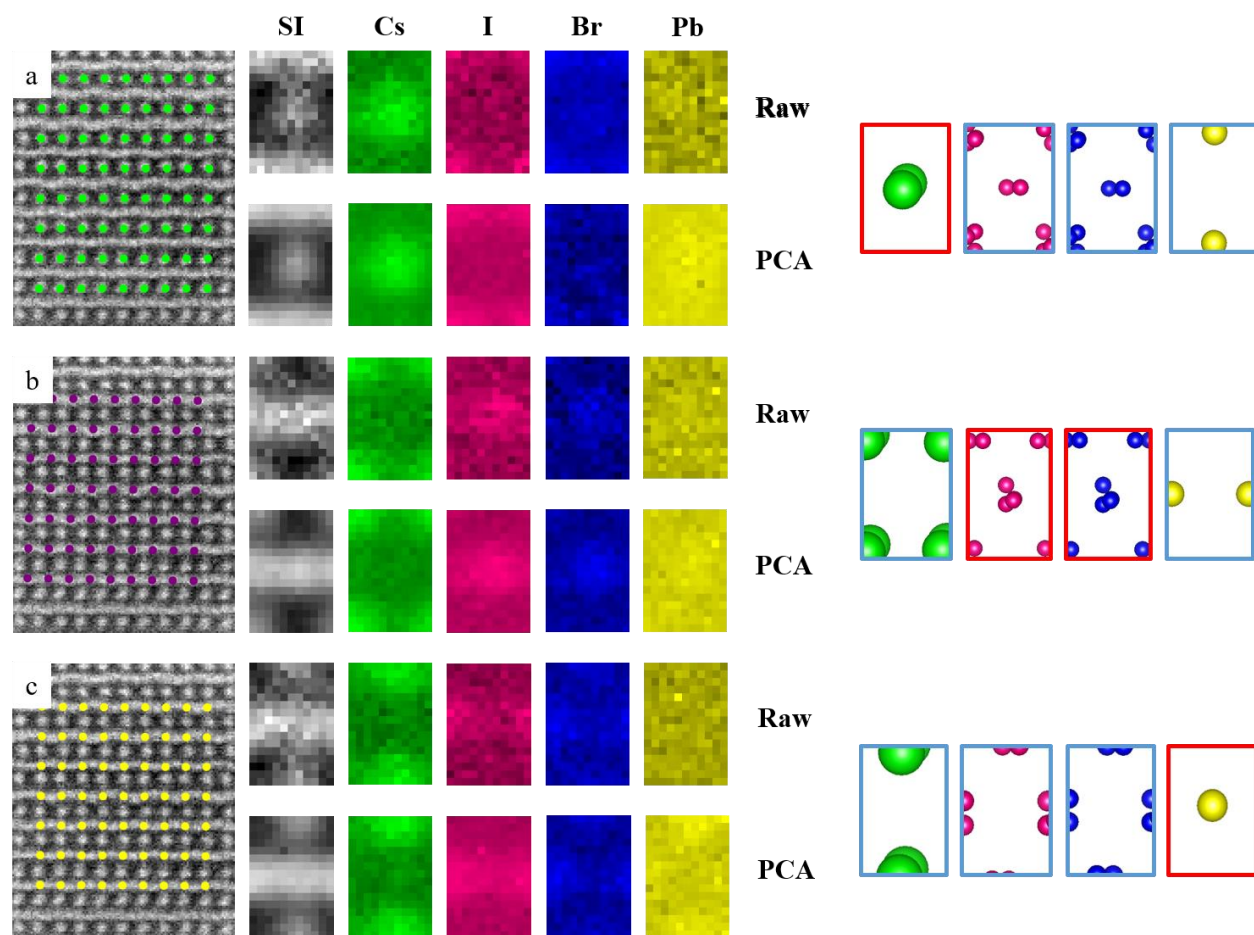


**Figure 20.** EELS elemental maps extracted from stacks of signals around repeating sample features. For each feature elemental maps were extracted from raw and PCA filtered data. (a) Signal extracted around Cs atomic columns, (b) signal extracted around Br/I columns and (c) signal extracted from Pb atomic columns.

Due to the poor signal-to-background ratio of the lead peak, it was not possible to extract any lead signals. However, it is evident from the raw data that no other element was detected at the lead position. It was observed that when the PCA filter was applied, a signal at the expected lead position appeared as an artifact of the filter for both iodine and cesium.

Although no beam damage was observed after low-dose imaging and 4D STEM, high-dose imaging and spectroscopy resulted in rapid, severe damage of the lattice. After only a few scans with conventional imaging doses of  $\sim 2 \cdot 10^4 \text{ e}^-/\text{\AA}^2$  (30  $\mu\text{m}$  aperture,  $<15 \mu\text{A}$  emission current, 8 C spot size), beam damage was observed in the form of high-contrast lead precipitates in the host lattice (Figure 21 (b)). After spectroscopic imaging with a high dose (30  $\mu\text{m}$  aperture,  $<15 \mu\text{A}$  emission current, 6C spot size), severe damage with a dismantling of the host lattice left a hole in the structure. A large number of nanoparticles was found in the damaged areas (Figure 21 (d)).



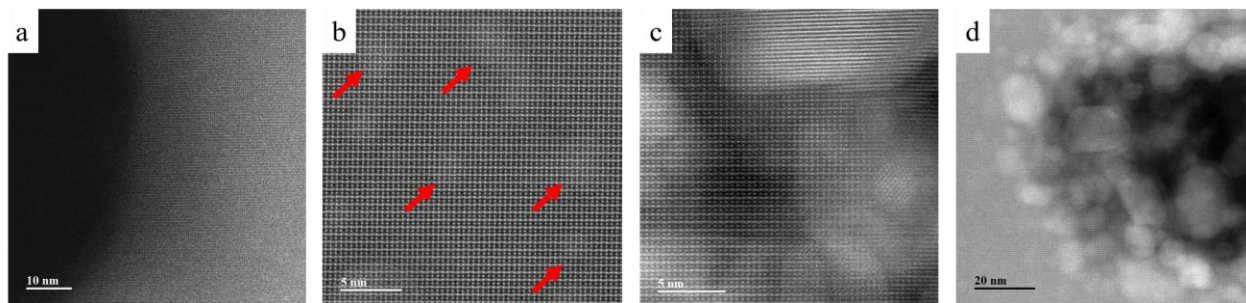


**Figure 21.** Damage pathway of  $\gamma$ -CsPbIBr<sub>2</sub> with increasing dose. (a) No damage was observed after low-dose imaging and 4D STEM. (b) With conventional imaging doses, beam damage occurred after a few scans as high-contrast nanoprecipitates indicated by arrows. (c) After high-dose SI acquisition, a large number of nanoparticles formed, dismantling the lattice and leaving a hole behind (d).

Based on the atomic structure, the precipitates were identified as metallic lead. On their way through the lattice, the lead precipitates distorted the host lattice. In addition, in some cases, the formation of a second phase was observed in the damaged areas. These particularities are exemplified in Figure 22.

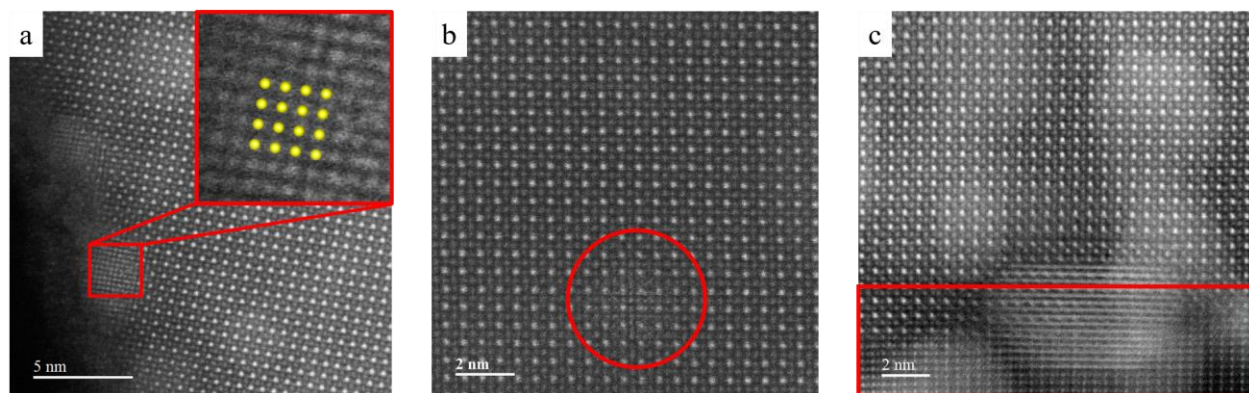


**Figure 22.** (a) Cubic metallic lead precipitate with an overlay of the atomic structure in the inset. (b) Distorted host lattice due to precipitate diffusion under electron beam irradiation. (c) Secondary phase forming in severely damaged areas as lead leaves the lattice.

To further characterize the beam-induced damage, elemental maps were extracted from simultaneously recorded EELS and XEDS SIs. Since only a very weak lead signal was recorded for the high energy loss Pb edge in EELS; the Pb signal was extracted from the XEDS SI for interpretation. The elemental maps shown in Figure 23 confirm the precipitation of Pb nanoparticles. SI data was acquired over the area indicated by a red rectangle. The investigated area contains strongly damaged areas as well as less damaged areas. In both cases, lead precipitates are recognizable.



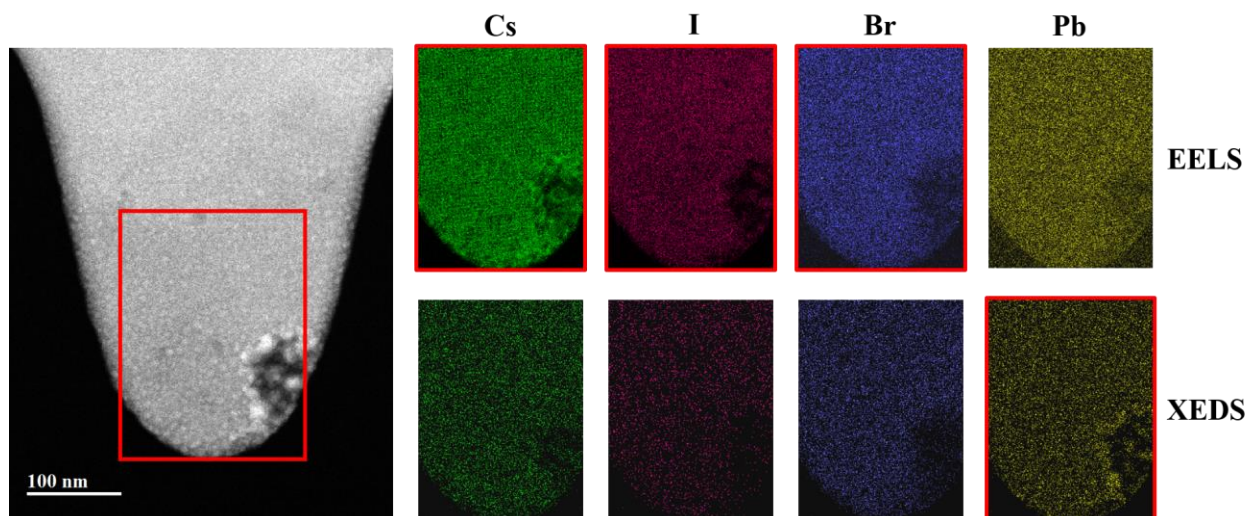


**Figure 23.** Elemental maps extracted from EELS and XEDS SIs. Due to the low signal-to-background ratio of Pb signals in EELS measurements, XEDS maps were extracted to confirm the presence of Pb nanoprecipitates.

In addition, a sharp decrease in the relative peak intensity of bromine and iodine in the XEDS SI within damaged areas indicates a depletion of Br and I as shown in Figure 24. For comparison, the spectra were normalized to the  $\text{Cu}_{\text{K}\alpha 1,2}$  peak. While no difference is observed between less and severely damaged areas for the Cs peaks, a clear difference is visible in Br and I peak intensities. The lower peak intensities for Br and I indicate a loss of halide species upon irradiation. A slightly stronger signal for Pb is recorded in the damaged region and assigned to the accumulation of a large number of Pb nanoparticles.

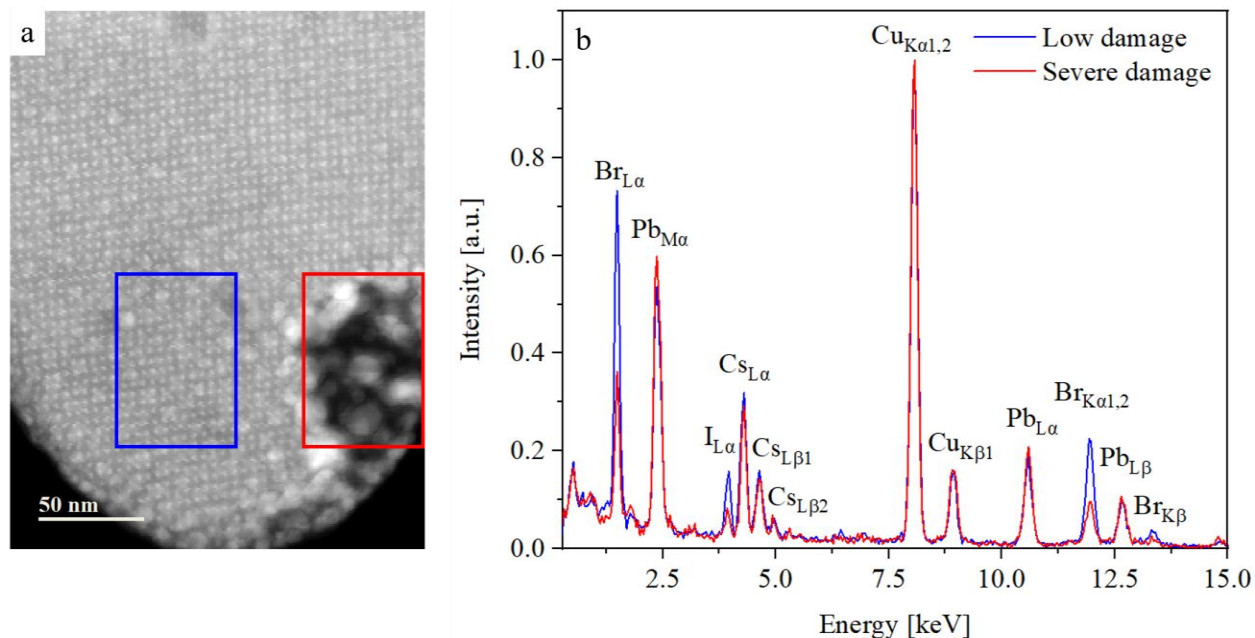


**Figure 24.** (a) Simultaneously acquired ADF image of the damaged structure containing a severely damaged area. (b) XEDS spectra extracted from the insets in (a) for an area of low damage (blue) and severe damage (red). The spectra were normalized to the  $\text{Cu}_{\text{K}\alpha 1,2}$  peak of the supporting grid.

### 3.4. CsPbI<sub>3</sub>

CsPbI<sub>3</sub> samples were prepared directly on the TEM grid as thin films by drop-casting and spin coating. As this material was also extremely sensitive under conventional radiation doses, the dose was reduced. An aperture of 20  $\mu\text{m}$  (14.4 mrad convergence angle) was used, and all images were captured with a spot size of 10 C. The electron gun emission current was reduced from 15  $\mu\text{A}$  to  $<5 \mu\text{A}$ , i.e., to less than 1/3 of its usual value. Atomic structure images acquired with an ADF detector are shown in Figure 25 for scattering angles between 83 and 205 mrad. Each image represents a drift corrected summed stack of 10 images captured with a pixel time of 2  $\mu\text{s}$  resulting in an overall acquisition time of 20.97 s. The beam current was measured as 0.96 pA.

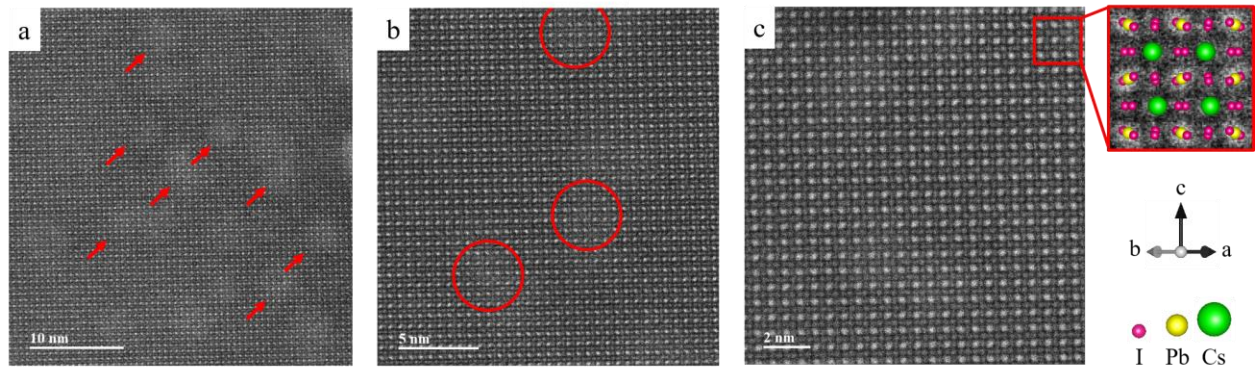


**Figure 25.** ADF images of CsPbI<sub>3</sub>. (a) Image acquired with a dose of  $\sim 830 \text{ e}/\text{\AA}^2$ . Beam damage in the form of bright-contrast lead precipitates is visible and indicated by red arrows. (b) Image acquired with a dose of  $\sim 2110 \text{ e}/\text{\AA}^2$ . Distorted host lattice due to mobile lead precipitates, highlighted by red circles. (c) High magnification image with structural inset. The image was acquired with a dose of  $\sim 4530 \text{ e}/\text{\AA}^2$ .

From the atomic structure images of CsPbI<sub>3</sub>, the presence of an orthorhombic structure can be deduced. This orthorhombic CsPbI<sub>3</sub>, also called  $\gamma$ -CsPbI<sub>3</sub>, belongs to the Pbnm space group. The images in Figure 25 show the atomic structure along the crystallographic [110] direction. Along this orientation, differently oriented Pb/I atomic columns are distinguishable. However, even for low-dose conventional imaging, beam damage was visible in the structure. One reason for this is that a certain dose was already applied to adjust the microscope and on the other hand the beam current was still relatively high. Therefore, the dose was reduced further by lowering the emission current to  $<1 \mu\text{A}$  to reduce and avoid beam damage. ADF images including convergence angles between 83 and 205 mrad are shown in Figure 26. Even at such low doses, radiation damage was observed close to the specimen edge after scanning the beam a few times to adjust the microscope.

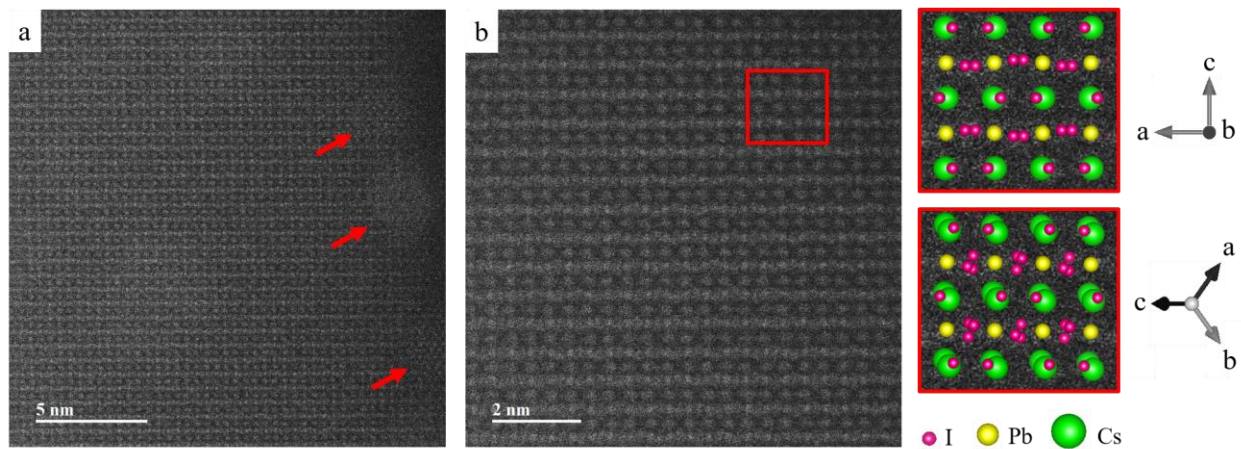


**Figure 26.** (a) ADF image captured with a dose of  $\sim 630 \text{ e}/\text{\AA}^2$  and a beam current of  $\sim 0.23 \text{ pA}$ . Beam damage is observed close to the specimen edge, indicated by red arrows. (b) Higher magnification image acquired with a dose of  $\sim 1180 \text{ e}/\text{\AA}^2$  and a beam current of  $\sim 0.19 \text{ pA}$ . The insets in (b) show possible crystal orientations.

Due to the poor SNR of the ADF detector at low electron doses, it was again unclear which structural orientation was present. Therefore, 4D STEM datasets were acquired at low doses using the DEC. Datasets were acquired for  $500 \times 500$  probe positions and each CBED was captured within a collection angle of  $\sim 92.2 \text{ mrad}$ . Due to the high magnification and relatively slow scanning speed a dose of  $\sim 3540 \text{ e}/\text{\AA}^2$  was used to record the dataset. The electron beam current was calculated from the CCD image to be  $0.2 \text{ pA}$ . The synthetic images calculated for three different detector geometries are shown in Figure 27. Already from the synthetic images the present structural orientation becomes evident. The crystallites are oriented along the  $[111]$  direction similar to  $\gamma\text{-CsPbIBr}_2$ .

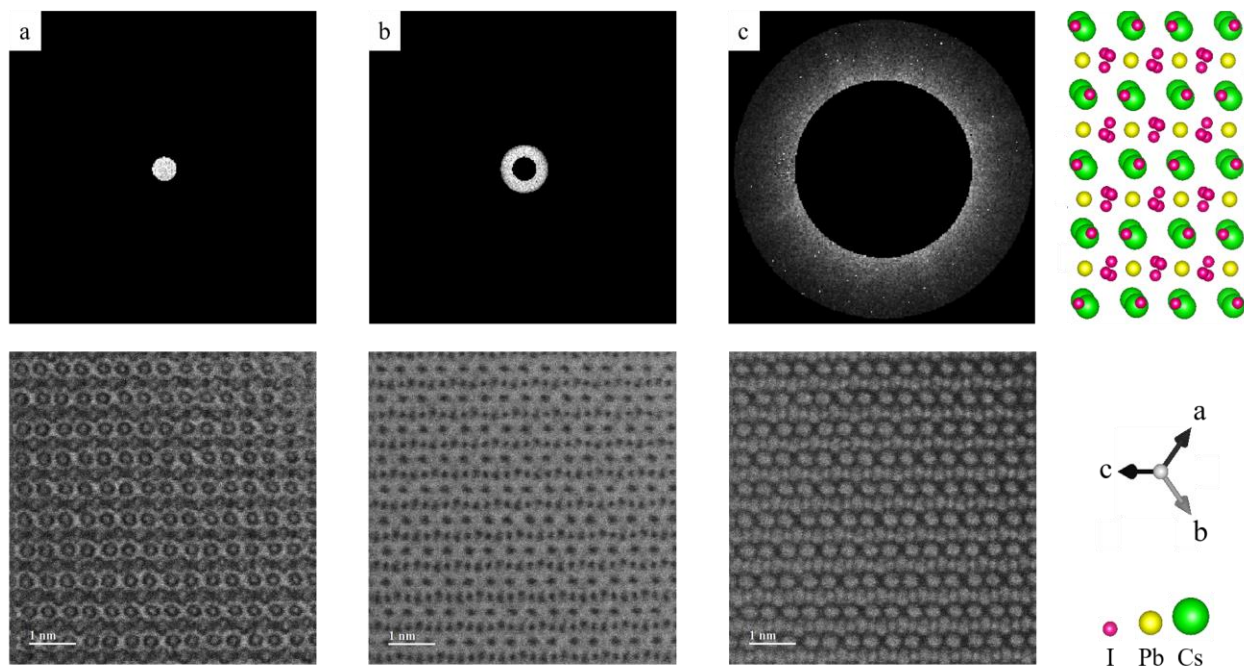


**Figure 27.** Synthetic STEM images of  $\gamma\text{-CsPbI}_3$  calculated by applying detector masks. (a) BF image from a mask that includes scattering angles of  $0\text{--}7.2 \text{ mrad}$ , (b) ABF image using a mask that includes scattering angles of  $7.2\text{--}14.4 \text{ mrad}$  and (c) ADF image calculated from a mask that includes scattering angles of  $53.3\text{--}92.2 \text{ mrad}$ .



Ptychographic reconstructions were performed from the same data sets used for the synthetic images. The results are shown in Figure 28.

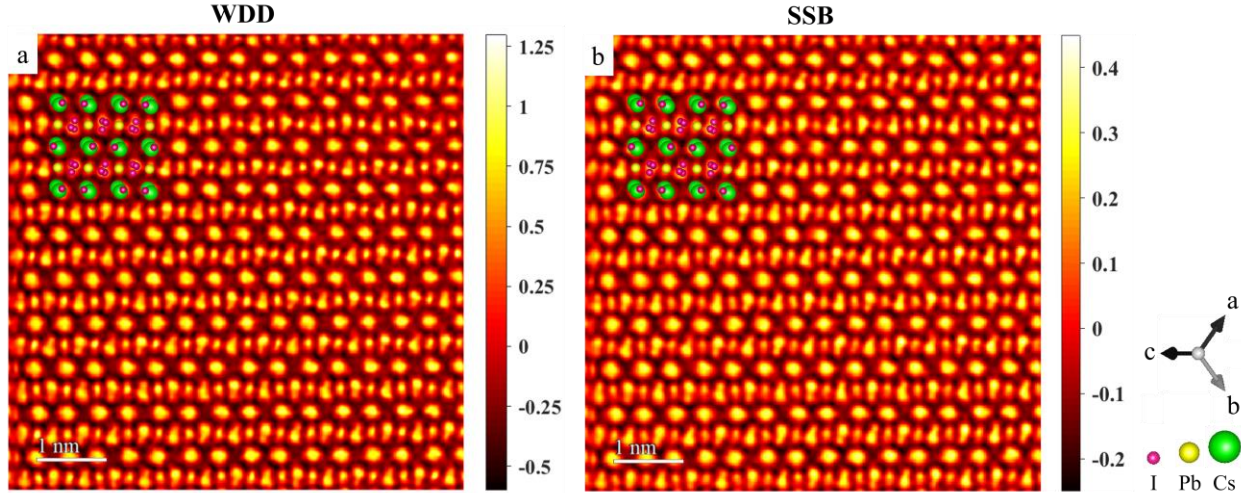


**Figure 28.** Reconstructed phase in radians of  $\gamma$ -CsPbI<sub>3</sub> along the [111] direction. (a) WDD and (b) SSB ptychography. In both cases, residual aberrations were neglected for image reconstruction.

Beam damage was not avoided completely in  $\gamma$ -CsPbI<sub>3</sub> with low doses, however, an atomically resolved image of the structure was successfully reconstructed. Although the thickness also changes from  $\sim 8$  nm to  $\sim 11$  nm from the right to the left, thickness effects are much less pronounced as for the CsPbIBr<sub>2</sub> sample. The effects of beam damage in  $\gamma$ -CsPbI<sub>3</sub> were similar to those seen in the previously studied materials. Upon prolonged irradiation, high-contrast lead precipitates initially formed preferentially on edges and grain boundaries. Upon further irradiation, the perovskite host lattice was destroyed and in some cases, a second phase formed in addition to the nanoparticles. Figure 29 shows a highly damaged area. At the lower right corner of Figure 29, the still intact perovskite lattice can be seen. The inset shows a magnified damaged area with lead precipitates and the second phase, which was not examined in further detail here and is presumably a phase containing cesium.

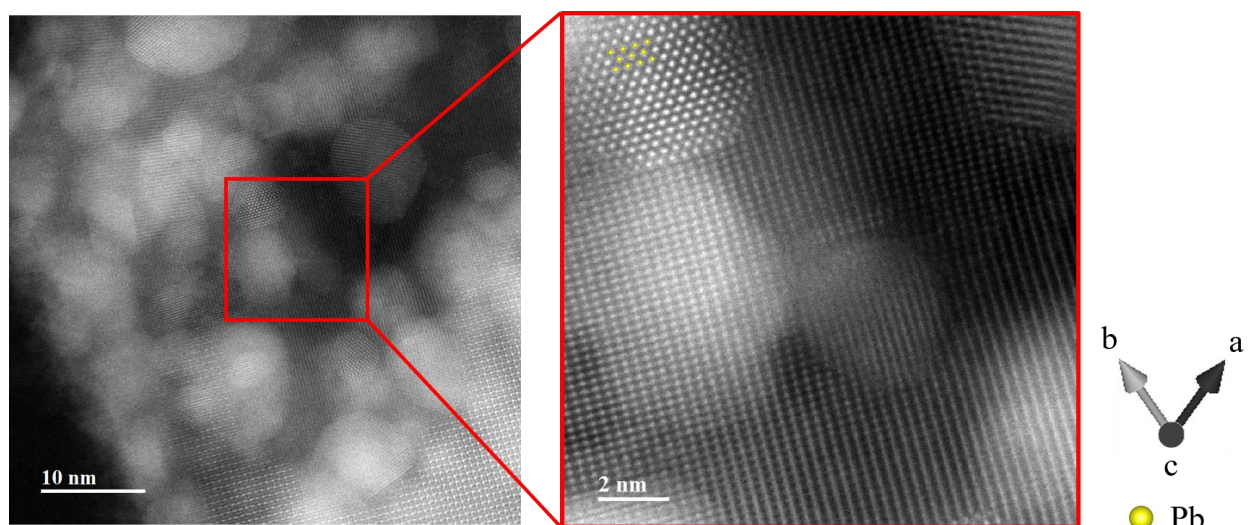


**Figure 29.** Severely damaged perovskite lattice after high-dose irradiation. In addition to the formation of lead nanoparticles, the formation of a second phase was observed.

Due to the high sensitivity of  $\gamma$ -CsPbI<sub>3</sub>, it was not possible to perform high-magnification spectroscopic imaging for elemental mapping of the atomic structure. Interestingly, copper precipitates were found on the sample surface in some cases. The origin of these copper precipitates was suspected either from the supporting copper grid itself or in contamination of the precursor solution. Since copper can dope  $\gamma$ -CsPbI<sub>3</sub> at the Pb site, it cannot be ruled out that the stability of the material was affected. It has been shown for nanocrystals that copper doping increases the general stability of CsPbI<sub>3</sub>.<sup>68</sup> No copper signal was found in the perovskite lattice itself, yet the material appeared to be more stable around the precipitates. Therefore, to ensure that the presence of the copper particles did not affect the measurement results, all investigations were performed at sites free of any copper contaminations. Figure 30 shows EELS elemental maps over an area containing a copper precipitate. From the extracted data it is evident, that the copper signal is mostly confined to the area of the precipitate. To reduce the noise level in the data, a PCA filter including 30 principal components was used. Due to the low signal-to-background ratio, the lead signal was not included here. Although the radiation dose was relatively high, no beam damage was observed around the copper particle after SI acquisition.

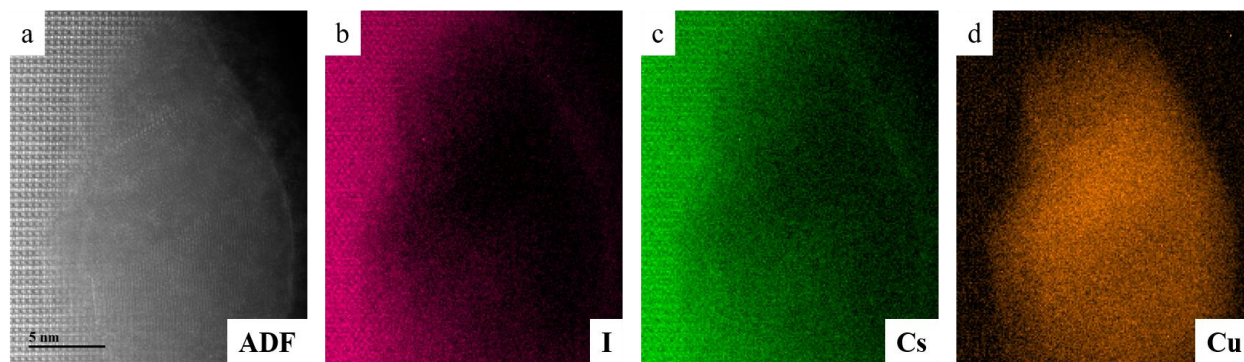


**Figure 30.** Maps, extracted from an EELS SI of a copper precipitate. (a) Simultaneously acquired ADF image, (b) extracted signal for the I M<sub>4,5</sub> edge, (c) extracted signal for the Cs M<sub>4,5</sub> edge, (d) extracted signal for the Cu L<sub>2,3</sub> edge.

## 4. Discussion

### 4.1. Noise and dose efficiency

#### 4.1.1. Direct electron detectors

In addition to significant advances in TEM technology, including vacuum systems, aberration correction, and field emission sources, electron detectors are continuously improved. Since the introduction of ADF detectors, typically consisting of scintillator photomultiplier tube arrangements, detector geometries and information processing have been enhanced further and further. Various detector geometries, e.g., segmented detectors, bright-field or annular bright-field detectors, allow for fast readout speed and small pixel dwell times in the  $\mu\text{s}$  range.<sup>69</sup> However, all these detector geometries integrate the signal over large areas, and information is lost. The detectors require a lot of space, so in most cases, measurements cannot be carried out simultaneously. As a result, measurements have to be carried out consecutively, causing difficulties in comparability due to sample drift. Furthermore, higher doses are required, which is inconvenient for sensitive materials.<sup>70</sup> Compared to the variety of scintillator-based devices, DEC detectors provide data with a much lower noise level with increased detector quantum efficiency (DQE) and modulation transfer function (MTF). They possess a comparatively high readout speed and radiation hardness. They can be considered as universal detectors enabling the acquisition of data with all possible detector geometries simultaneously. Moreover, they provide access to advanced techniques such as ptychography by recording the entire CBEDs instead of signal integration.<sup>70,71</sup> Besides all the advantages of DEC detectors, there are still some limitations. Until now, at least for the MerlinEM Medipix3 detector installed on the ARM200F in Stuttgart, there was no way to extract any live information from the 4D STEM data during the measurement. Conventional detectors are still needed to navigate to sample features of interest and to align the microscope. This makes it extremely difficult to adjust the microscope at low doses, as the DQE of scintillator-based detectors decreases with decreasing dose. In addition, very large amounts of data are generated in a short time and must be stored and processed. A dataset, e.g., for  $\text{CsPbI}_3$ , contains  $500 \times 500$  probe positions for which  $256 \times 256$ -pixel CBEDs are recorded. This results in over  $1.6 \cdot 10^{10}$  data points and a total dataset size of  $\sim 15$  GB that must be processed. For the low-dose investigations of  $\text{CsPbIBr}_2$  and  $\text{CsPbI}_3$ , both the synthetic images and the phase reconstructions have a higher SNR than the data acquired with the scintillator ADF detector. While the structural orientation can already be seen from the synthetic images, the SNR in the ADF images is too poor to draw any conclusions. Regarding the definition of a signal-to-noise ratio already implied by its name, there are two main factors responsible for the poor quality of ADF images: the available signal and the extent of noise. Due to the faster pixel dwell time, the ADF images were captured at a lower total dose, which reduced the available signal. However, also for images acquired with doses similar to the 4D STEM datasets, a significantly poorer image quality was observed. The collection angle for the selected camera length of the ADF detector was larger (83–205 mrad) than the

angle used for the synthetic ADF images (53.3–92.2 mrad). For the high-angle annular dark-field images (HAADF) captured with the scintillator detector, the available signal for image generation is lower. Weaker scattering at high angles lowers the SNR from the signal side. For phase reconstructions, the bright-field disc of the CBEDs was the focus. Therefore, a camera length was chosen where the bright-field disc covered a sufficient number of pixels on the DEC. The electrons were captured within a smaller overall collection angle. The synthetic ADF images represent low-angle annular dark-field images (LAADF) with a better SNR on the signal side due to the contribution of a larger amount of electrons. For future investigations, the camera length will be adjusted for direct ADF imaging at low doses to include lower scattering angles to increase the available signal. From the noise side of the SNR, there are three main contributions to noise in STEM images. First of all, due to the discrete nature of electrons, there is statistical noise, also called shot noise, following a Poisson distribution.<sup>72</sup> During data acquisition, the readout process adds additional, so-called readout noise to the data. A measure of the amount of noise a detector adds to the signal is the DQE. In general, the DQE is specified as

$$\text{DQE} = \frac{(\text{SNR}_{\text{output}})^2}{(\text{SNR}_{\text{input}})^2} \leq 1 \quad (4.1)$$

The DQE is not a constant, but depends on several factors. The DQE varies with spatial frequency, electron imaging conditions (i.e., electron dose), electron beam energy, and detector operation mode. It strongly depends on how the signal is generated. In the following, the influence of signal generation, i.e., the influence of the detector gain, is discussed in more detail. For a mean number of  $N$  electrons arriving in an interval, the standard deviation (statistical noise) is  $\sqrt{N}$ . For an average of  $N$  incident electrons the  $\text{SNR}_{\text{input}}$  is given as  $N/\sqrt{N} = \sqrt{N}$ . In scintillator-based detectors, incident electrons are converted into photons that are transferred to the sensor. An image is created based on the amount of light detected for each pixel. DEC's do not have a scintillator, and in the case of the MerlinEM Medipix3 detector, the electrons create a set of electron-hole pairs as they pass through the semiconductor sensor material on top of the chip. Regardless of the mechanism, for all types of detectors, the  $N$  average incident electrons are converted into a  $gN$  output signal, where  $g$  refers to the gain of the detector. The  $gN$  output signal has a variance of  $\sqrt{gN}$ . The input noise  $\sqrt{N}$  is converted to  $g\sqrt{N}$  and thus the  $\text{SNR}_{\text{output}}$  is given as  $gN/\sqrt{g^2N + gN}$ . Substituting  $\text{SNR}_{\text{output}}$  and  $\text{SNR}_{\text{input}}$  in equation (4.1), the DQE can be calculated for an ideal detector (not considering the influences of imaging conditions, spatial frequency and detector modes here).

$$\text{DQE} = \frac{(\text{SNR}_{\text{output}})^2}{(\text{SNR}_{\text{input}})^2} = \frac{\left(\frac{gN}{\sqrt{g^2N + gN}}\right)^2}{(\sqrt{N})^2} = \frac{1}{1 + \frac{1}{g}} \quad (4.2)$$

The DQE is proportional to the gain factor of the camera, and therefore it is clear that a high detector gain preserves a good DQE, while for low detector gains (with  $g$  between 2 and 10 counts/electron for

scintillators) the DQE is limited. Contributions of readout noise are effectively suppressed in DEC's due to the large gain factor. With an energy of 3.6 eV required to generate an electron-hole pair in silicon, a 60 keV electron can create over 16000 electron-hole pairs, and the readout noise is practically negligible.<sup>73</sup> Therefore, the pixel array detectors outperform conventional scintillator-based cameras in terms of readout noise. Furthermore, the DQE is strongly dose-dependent for low-gain cameras. At low doses, i.e., with only a few electrons impinging on the camera, the DQE of a scintillator-based camera is typically very low due to the readout noise.<sup>74</sup> This explains the poor SNR in the low-dose ADF images illustrated in Figure 17 and Figure 25. Recording frames with a short pixel dwell time, subsequent drift correction, and summation is also problematic at such low doses. Noise might sum up and degrade the image quality additionally. Nevertheless, to see the proper atomic structure and avoid the influences of sample drift, the method was still used. Scan distortions or artifact-affected frames, as well as beam damage starting above a certain overall dose, can be excluded. For conventional doses, the DQE of scintillator devices plateaus and drops again for higher doses due to channel-to-channel gain variations that cannot be properly corrected.<sup>74</sup> Therefore, the ADF images illustrated in Figure 11 show high contrast and good SNR for conventional doses. Even at very low electron doses, there is practically no readout noise present in the images captured with the DEC, which explains the higher SNR of the synthetic images. The third major contribution to noise is Gaussian distributed thermal noise (thermal electron-hole pair formation). In the MerlinEM Medipix3 camera, thermal noise is suppressed by selecting proper threshold values for event energies to be detected.<sup>75</sup> The overall noise is therefore dominated by statistical noise and is uncorrelated, since all measurements are independent with respect to  $\mathbf{K}_f$  and  $\mathbf{R}_0$ . In conclusion, noise in the 4D STEM dataset is uniformly distributed over all spatial frequencies and real-space coordinates and is therefore referred to as white noise.<sup>64</sup> The nature of the phase reconstruction processes is responsible for the high SNR and high image quality achieved in the phase-reconstructed images.

#### 4.1.2. Ptychography

In SSB ptychography, the signal for a WPO is extracted only from the double overlap regions (see Figure 8). Acting as an intrinsic band pass filter, detector pixels outside the double overlap zone are rejected. This has been shown to increase the SNR compared to imaging techniques such as CoM or iCoM that use the entire bright-field disc.<sup>76</sup> The noise level for each spatial frequency can be directly related to the size of the double overlap regions. In SSB ptychography, the noise level changes with spatial frequency  $\mathbf{Q}_0$ . Thus, especially high and low spatial frequencies with small double overlap regions are transferred with a better efficiency due to elimination of unnecessary detector areas containing only noise compared to other imaging techniques such as DPC or ABF imaging.<sup>72</sup> Therefore, the atomic structure of the HPs is clearly revealed in the phase-reconstructed images with a higher SNR and better contrast than synthetic images and especially ADF images due to the better detector performance at low doses.



The key parameter for noise contribution in WDD ptychography is the choice of the  $\epsilon$  parameter of the Wiener filter (equations (1.24) and (1.25)). The parameter determines how much signal and noise are suppressed. Especially at low radiation doses, the parameter must be chosen carefully to avoid amplification of noise or loss of information-rich signal. O’Leary et al. demonstrated for an aluminosilicate zeolite (ZSM-5) dataset captured with a low dose of  $200 \text{ e}^-/\text{\AA}^2$  that small values for  $\epsilon_{\text{rat}}$  (0.01–0.1) can lead to noise amplification whereas larger values of  $\epsilon_{\text{rat}} = 1$  might avoid noise amplification but also suppress meaningful data. They suggested to use SSB ptychography whenever possible.<sup>64</sup> Figure 31 shows WDD reconstructions of the CsPbI<sub>3</sub> dataset captured with a low dose of  $\sim 3540 \text{ e}^-/\text{\AA}^2$ . For comparability, the arbitrary phases in the reconstructions for different  $\epsilon_{\text{rat}}$  values were normalized. A too low value of 0.01 for  $\epsilon_{\text{rat}}$  leads to noise amplification, while a high value of 1 suppresses noise, but no specific improvement is evident compared to a value of 0.1. Therefore, a  $\epsilon_{\text{rat}}$  value of 0.1 was selected in this thesis.

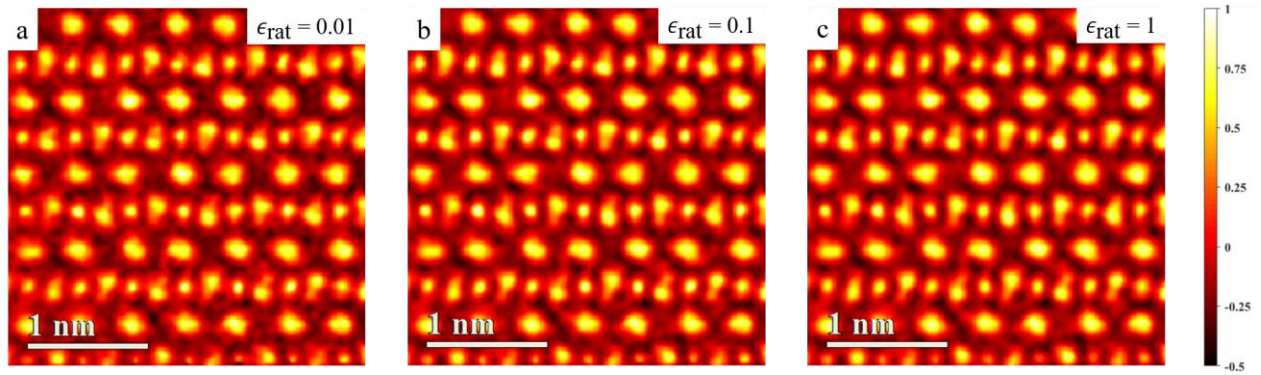


**Figure 31.** Comparison of WDD phase reconstruction results for CsPbI<sub>3</sub>. Enlarged subsections are shown for  $\epsilon$  ratios of (a) 0.01, (b) 0.1 and (c) 1.

In many cases, the improved dose efficiency of electron ptychography with much lower noise levels has been shown to reveal interesting sample features such as monovacancies, adatoms, lattice defects, etc. Recently, a new world record was achieved using multislice defocused probe ptychography with a resolution limited only by thermal fluctuation of the atoms. The researchers were able to localize single embedded dopant atoms in all three dimensions from a single projection measurement.<sup>66,77,78</sup>

## 4.2. Resolution

As stated in equation (1.4), in an uncorrected microscope, the highest possible resolution is limited mainly by spherical aberration, which increases with an increasing radial angle. For a given spherical aberration, the angular range over which the phase of the electron wave remains constant is very limited. A certain defocus value can be selected to compensate for aberrations, and apertures are used to limit the angular range that yields a minimally aberrated beam.<sup>54,55</sup> Using an aperture of specific size introduces a resolution limit as a function of the aperture semi-convergence angle. According to the Rayleigh criterion, a diffraction-limited resolution  $d$  is given for an aperture with a semi-convergence angle  $\alpha$  as

$$d = 0.61 \cdot \frac{\lambda}{\alpha} \quad (4.3)$$

with  $\lambda$  as the wavelength of beam electrons.<sup>79</sup>

Apertures are chosen to find a good balance between diffraction- and aberration-related resolution limit. In principle, larger apertures can be used in aberration-corrected microscopes, but in this case, higher-order or parasitic geometric aberrations, as well as chromatic aberration, limit the resolution in a complex way.<sup>80,81</sup> In this work, the smallest available apertures were used at the expense of resolution to reduce the radiation dose. For the acquisition of CsPbBr<sub>3</sub> datasets, a 30  $\mu\text{m}$  aperture, resulting in a probe of 20.4 mrad semi-convergence angle  $\alpha$ , was used. This imposes a diffraction-limited resolution of 0.75  $\text{\AA}$ . For the more sensitive CsPbIBr<sub>2</sub> and CsPbI<sub>3</sub> samples, a 20  $\mu\text{m}$  aperture with a 14.4 mrad probe semi-convergence angle  $\alpha$  was used. In this case, the electron dose was lowered by a factor of  $\sim 2$  compared to the 30  $\mu\text{m}$  aperture. The diffraction-limited resolution is reduced in this case to 1.06  $\text{\AA}$ . Furthermore, the spatial resolution in STEM is generally determined by the probe size and probe current, as well as the beam-sample interaction. Besides that, the resolution is further reduced by experimental factors such as scan distortions, image noise, radiation damage, structural mistilt, etc.<sup>53,82,83</sup> Figure 32 shows the power spectra of the respective ptychographic reconstructions on a logarithmic scale. The big red circles indicate the diffraction-limited resolution calculated with equation (4.3).

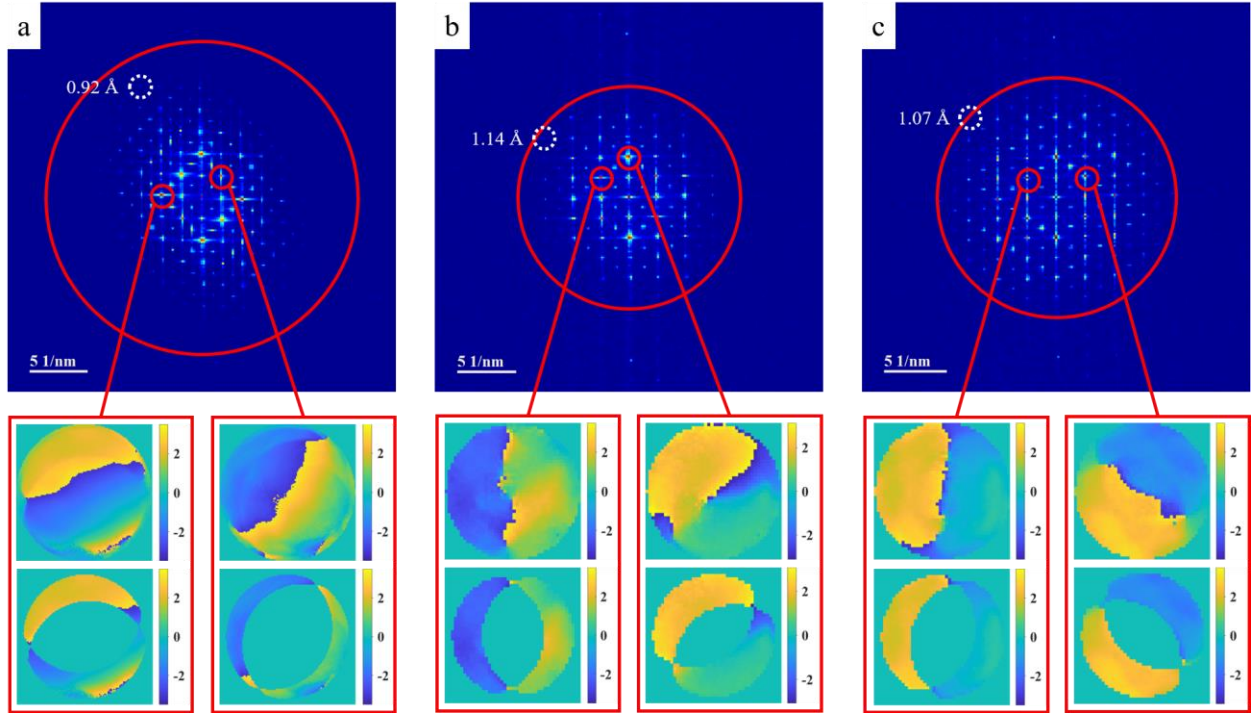


**Figure 32.** Power spectra of  $G(\mathbf{K}_f, \mathbf{Q}_0)$  for (a) CsPbBr<sub>3</sub>, (b) CsPbIBr<sub>2</sub> and (c) CsPbI<sub>3</sub>. Big red circles indicate the diffraction limited resolution. For each power spectrum, two spatial frequencies with a high contribution are illustrated and the phase of  $G(\mathbf{K}_f, \mathbf{Q}_0)$  is shown as a function of  $\mathbf{K}_f$ . For each inset the whole bright-field disc is shown at the top and extracted signal relevant for the phase reconstruction at the bottom.

In the case of CsPbBr<sub>3</sub> with a diffraction-limited maximum resolution of 0.75 Å, the practically achieved resolution is much lower (up to ~0.92 Å). For two spatial frequencies with large power spectrum values, the phase and extracted signal after multiplication with a mask are highlighted. Theoretically, using an aberration-free beam, the two side bands should have a phase shifted by  $\pi$  with respect to each other. In all regions outside the double overlap, the phase should be equal to zero or cancel each other. From the two illustrated phases of  $G(\mathbf{K}_f, \mathbf{Q}_0)$  as a function of  $\mathbf{K}_f$ , it is evident, that this is not always the case. Especially the presence of residual aberrations leads to phase changes and these in turn to a deterioration of the resolution. Besides that, thickness effects, the slight tilt of the sample off zone axis and scan distortions are responsible for the lower actual resolution. Since a larger aperture was used for CsPbBr<sub>3</sub>, the absolute resolution is better than for CsPbIBr<sub>2</sub> and CsPbI<sub>3</sub> where a smaller aperture was used. However, the relative resolution with respect to the diffraction limit is better for the smaller apertures. For CsPbIBr<sub>2</sub>, diffraction spots corresponding to a real-space distance of 1.14 Å are visible, and for CsPbI<sub>3</sub>, even spots corresponding to a distance of 1.07 Å can be seen. The reason for the improved relative resolution is that the smaller semi-convergence angle of the 20 µm aperture reduces the beam to a diameter that is less affected by aberrations resulting in almost aberration-free datasets. Although the same aperture was used for CsPbIBr<sub>2</sub> and CsPbI<sub>3</sub> the actual resolution achieved for the CsPbIBr<sub>2</sub> dataset is lower than that of the CsPbI<sub>3</sub> dataset. In general, less high-spatial-frequency reflections are visible in the power spectrum. The CsPbIBr<sub>2</sub> dataset shows slightly more signs of aberration-induced phase changes due to imperfect microscope alignment. The CsPbI<sub>3</sub> dataset seems to be almost free of any aberrations. The resolution limit of 1.06 Å is practically achieved since diffraction spots corresponding to a real-space distance of 1.07 Å are still visible. In principle, for both SSB and WDD ptychography, it is possible to correct for aberrations in silico in a post-acquisition step. In SSB ptychography, spherical aberrations are equal in  $A(\mathbf{K}_f)$  and  $A(\mathbf{K}_f - \mathbf{Q}_0)$  for all points on the line  $\mathbf{K}_f = \mathbf{Q}_0/2$  due to their symmetry. This means they cancel in  $A(\mathbf{K}_f)A^*(\mathbf{K}_f + \mathbf{Q}_0)$  and  $A^*(\mathbf{K}_f)A(\mathbf{K}_f - \mathbf{Q}_0)$ . By extracting data only from points that satisfy  $\mathbf{K}_f = \mathbf{Q}_0/2$ , the phase can be reconstructed without the influence of spherical aberrations. However, this severely limits the dose efficiency of SSB ptychography. In modern aberration-corrected STEMs, minor aberrations may remain, but instead of using only a small subset of  $G(\mathbf{K}_f, \mathbf{Q}_0)$ , one usually relies on the aberration corrector. Therefore, no post-processing aberration correction is usually performed in SSB ptychography.<sup>57</sup> In WDD, a post-acquisition aberration correction is possible via singular-value decomposition, a matrix-inversion method. The aberration coefficients can be determined from the phase of  $G(\mathbf{K}_f, \mathbf{Q}_0)$ . A probe function is synthesized and deconvolved from the data. It was shown that aberration correction is worthwhile and gives good results when the microscope is severely misaligned. With almost perfect alignment and datasets as good as the CsPbIBr<sub>2</sub> and CsPbI<sub>3</sub>, the post-processing aberration correction would not have an effect and was therefore not performed in this thesis.<sup>63,65,84</sup> Besides different environmental conditions during the measurement, mainly thickness effects might be primarily responsible for the lower amount of high spatial frequency spots

visible in the power spectrum of CsPbIBr<sub>2</sub>. As mentioned before, the sample thickness in the reconstructed image of CsPbIBr<sub>2</sub> increases from the left to the right from  $\sim 17$  nm to  $\sim 22$  nm, whereas the thickness of the CsPbI<sub>3</sub> sample was generally lower with a lower increase from  $\sim 8$  nm to  $\sim 11$  nm from the right to the left. The CsPbBr<sub>3</sub> nanocrystal had a uniform thickness of  $\sim 9$  nm. The atomic structures evident from the phase reconstructions appear to become increasingly blurred and indistinct with increasing thickness.

### 4.3. Thickness effects

For WPOA and POA, a multiplicative transmission function is assumed, which neglects any dynamical scattering effects. In the WPOA, amplitude and phase of the electron wave are independent on the angle of the incident beam electrons with respect to the sample. For thicker samples or samples containing heavy elements, dynamical scattering can no longer be neglected, and the multiplicative approximation for the beam being transmitted through the specimen is no longer valid. If WPOA and POA do not hold, kinematical conditions can be used, and electrons are assumed to be Bragg scattered once upon transmission. In the case of strong scattering, contrast reversals might be observed in the phase-reconstructed images, since phase shifts of more than  $2\pi$  occur with a reset of the phase to zero.

Rodenburg et al. have already considered the finite sample thickness in their seminal work on WDD ptychography. The scattering vector  $q_z$  in  $z$  direction is given by elastic scattering to the Ewald sphere and can be Taylor expanded around  $-(q_x^2 + q_y^2)/q^2$  as

$$q_z = q - \sqrt{(q^2 - q_x^2 - q_y^2)} \cong \frac{\lambda}{2}(q_x^2 + q_y^2) \quad (4.4)$$

The possible resolution  $d$  is determined by the maximum scattering angle  $q_{x,MAX} = 1/d$ . For a 2D material, the Ewald sphere measurement corresponds to the measurement of 2D diffraction intensities and the 3D transform is independent of  $q_z$ . For a 3D object with a certain thickness  $T$ , longitudinal speckles of size  $1/T$  are found. The 3D object can be treated as 2D as long as the Ewald sphere intersects the speckles, centered at  $q_z = 0$ . Based on this, Rodenburg et al. have derived an equation for the maximum sample thickness.

$$T \approx \frac{2d^2}{\lambda} \quad (4.5)$$

with an Ewald sphere departure less than the speckle width of  $1/T$ .<sup>54</sup>

Chapman et al. have used a stricter criterion of  $q_z < 1/4T$ , i.e., a departure lower than half the speckle half-width in the field of x-ray microscopy.<sup>85</sup> With this assumption the maximum allowable thickness of a specimen is given as

$$T \approx \frac{d^2}{2\lambda} \quad (4.6)$$

Tsai et al. tested the maximum allowable thickness in a numerical study and suggest that Rodenburg's criterion can be relaxed. According to their study, the maximum sample thickness can be calculated with equation (4.7).<sup>86</sup>

$$T \leq \frac{5.2d^2}{\lambda} \quad (4.7)$$

For an accelerating voltage of 200 kV, i.e., an electron wavelength of  $\lambda = 2.5079 \cdot 10^{-12}$  m, the theoretical maximum thickness values for the applicability of phase reconstruction algorithms are listed in Table 2 for the three different criteria according to equations (4.5), (4.6), and (4.7) where  $d$  is the diffraction-limited resolution calculated with equation (4.3).

**Table 2.** Maximum sample thickness to achieve the diffraction limited resolution for a given aperture. Three approximations presented by Rodenburg (equation (4.5)), Chapman (equation (4.6)), and Tsai (equation (4.7)).<sup>54,85,86</sup>

Maximum Thickness $T$	30 $\mu\text{m}$ aperture ( $d = 0.75 \text{ \AA}$ )	20 $\mu\text{m}$ aperture ( $d = 1.06 \text{ \AA}$ )
Chapman <sup>85</sup>	1.12 nm	2.24 nm
Rodenburg <sup>54</sup>	4.49 nm	8.96 nm
Tsai <sup>86</sup>	11.66 nm	23.30 nm

Regardless of how thick the sample actually is, there is nothing to stop someone from acquiring a 4D STEM dataset and applying the reconstruction methods. However, the results must be interpreted with caution. If the specimen becomes too thick, the achieved resolution decreases. This effect was particularly observed in the case of the CsPbIBr<sub>2</sub> sample. The sample was already relatively thick in the thinnest area with a thickness increase from left to right (see Figure 19). At a thickness of  $\sim 17$  nm to  $\sim 22$  nm the structure becomes more and more blurry and fine features are no longer visible. This effect is particularly pronounced for the SSB reconstruction since the WPOA desires a very thin specimen. As a result, less high-spatial-frequency spots were visible in the power spectrum and the resolution was reduced. Reversing the equations, an approximate maximum achievable resolution can be calculated for a given thickness. Table 3 shows the theoretically possible resolution according to Rodenburg, Chapman, and Tsai for the measured thickness of the samples investigated in this work.

**Table 3.** Maximum possible resolution for a given thickness or thickness range calculated by reversing equations (4.5), (4.6), and (4.7).

Possible resolution $d$	CsPbBr <sub>3</sub> ( $T = 9$ nm)	CsPbIBr <sub>2</sub> ( $T = 17 - 22$ nm)	CsPbI <sub>3</sub> ( $T = 8 - 11$ nm)
Chapman <sup>85</sup>	2.12 $\text{\AA}$	2.92 - 3.32 $\text{\AA}$	2.00 - 2.35 $\text{\AA}$
Rodenburg <sup>54</sup>	1.06 $\text{\AA}$	1.46 - 1.66 $\text{\AA}$	1.00 - 1.17 $\text{\AA}$
Tsai <sup>86</sup>	0.66 $\text{\AA}$	0.95 - 1.03 $\text{\AA}$	0.62 - 0.73 $\text{\AA}$

From the visible power spectrum spots and the resolution achieved in each case, it is evident that a higher resolution was achieved than predicted by the Rodenburg equation. However, the resolution was not quite as good as with the Tsai equation, where the calculated possible resolutions are higher than the diffraction limit. For the CsPbI<sub>3</sub> reconstruction from a sample with a thickness of  $\sim 8$  nm to  $\sim 11$  nm from right to left,

neither the thickness nor the thickness variation seems to have a strong influence on SSB and WDD reconstructions (see Figure 28). Diffraction-limited resolution is nearly reached, and high-spatial-frequency spots are visible. It appears that the Rodenburg criterion can be relaxed somewhat, and the Chapman criterion is too strict. It has been shown in the past that ptychographic imaging is possible well beyond its approximation constraints. Much thicker and heavier crystals can be imaged beyond the WPOA validity. In 1998, Plamann and Rodenburg already imaged Si (110) crystals up to 25 nm in thickness.<sup>87</sup> In addition, Yang et al. demonstrated the effectivity of ptychographic reconstructions for samples expected to exhibit dynamical scattering and therefore violating the multiplicative sample scattering function.<sup>65</sup> It is difficult to make a numerical statement because the resolution is additionally affected by aberrations. For each sample, only one dataset for the specific sample area and thickness was recorded. Besides that, the thickness estimation of the HP samples is rather uncertain. A log-ratio model was used to calculate the thickness from EELS measurement. Assuming independent scattering events, a simple expression can be found that includes the sample thickness.

$$\frac{T}{\lambda} = \ln\left(\frac{I}{I_0}\right) \quad (4.8)$$

where  $T$  refers to the sample thickness,  $\lambda$  is the mean free path of inelastic scattering,  $I$  is the area under the whole EEL spectrum and  $I_0$  is the integrated zero-loss-peak intensity.

If  $\lambda$  is known, the thickness can be estimated.<sup>15</sup> Since  $\lambda$  varies from material to material and depends strongly on the material- and measurement conditions, an exact calculation is difficult. To estimate the mean free path, a script was used to calculate  $\lambda$  based on the approach of Malis et al. involving experimental parameters.<sup>88</sup> According to the author, the script provides an approximate value with an accuracy of  $\pm 20\%$ . Therefore, the samples may be actually thinner or thicker depending on the accuracy of  $\lambda$ . The values calculated here, therefore, only represent a rough estimate of the approximate thickness. However, no contrast reversals with increasing thickness were observed in the phase-reconstructed images in this thesis. Moreover, peaks in the phase images can always be located at the atomic column positions compared to the synthetic images. In general, it appears that ptychographically reconstructed phase images are more robust to thickness changes and dynamical effects compared to HRTEM. For several reasons, it was impossible to use particularly thin specimens in this work. First of all, CsPbIBr<sub>2</sub> and CsPbI<sub>3</sub> samples were synthesized directly on the TEM grids. The intention here was to produce a film that covers the holes of the supporting carbon film on the copper grids. This allows the study of free-standing HPs. It was observed that at a certain dilution of the precursor solution, HP films with a lower thickness were synthesized, but they were only found on the carbon support film and no longer in any of the holes. Recording a 4D STEM dataset of a material on an amorphous carbon film makes little sense, as the carbon film reduces the data quality significantly. It was also observed, the thinner the crystals were, the more sensitive they reacted to the electron beam. This fact is discussed in more detail below. To be able to adjust the microscope accordingly and to record datasets of the undamaged structures, a sample area with an appropriate thickness was selected.

## 4.4. Beam damage

### 4.4.1. Damage mechanism

The first sign of radiation damage in all three materials of the AIHP class  $\text{CsPbX}_3$  investigated in this study was the occurrence of high-contrast nanoprecipitates. In recent reports, these nanoparticles have been consistently identified as metallic lead.<sup>44,45,89</sup> In this thesis, the presence of face-centered cubic metallic lead as a result of beam damage was verified from their bright-contrast in ADF images (heaviest atomic species), the atomic structure (see structural model overlay in Figure 22 or Figure 29), and XEDS and EELS spectroscopy. It was shown that x-rays, as well as electrons, are capable of reducing  $\text{Pb}^{2+}$  from various metal systems to  $\text{Pb}^0$ .<sup>90,91</sup> For oxide species or  $\text{CaF}_2$  compounds, electron-stimulated reduction of the cationic species is accompanied by oxidation and desorption of the anion species.<sup>92,93</sup> As demonstrated by Dang et al. for  $\text{CsPbBr}_3$  and  $\text{CsPbI}_3$  nanocrystals and by Zhou et al. for  $\text{CsPbIBr}_2$ , the formation of Pb nanoparticles goes along with desorption of the halide species from the material.<sup>44,45</sup> The loss of halide species upon irradiation was also observed for the HPs investigated in this study. From the XEDS investigations, a significant reduction in the relative peak intensity of the halide species is visible in severely damaged areas compared to less damaged areas (Figure 24). The stimulated desorption pathway may be due to a Knotek-Feibelman inter-atomic Auger mechanism. Incident electrons excite the cation species ( $\text{Pb}^{2+}$ ) and leave an inner shell hole. The inner shell hole is filled by an electron from a neighboring anionic species (e.g.,  $\text{Br}^-$ ). In an Auger emission process, the excess energy is absorbed by the anions. The emerging neutral or positively charged halide species desorbs to the vacuum.<sup>89,94</sup> This stimulated desorption process can be classified as a type of ionization damage.<sup>95</sup> Upon irradiation, the formation of Pb nanoparticles was observed starting preferentially on corners and edges of the crystals as well as on grain boundaries and the material surface. The material surface is characterized by a lower barrier to atomic diffusion. In addition, the atoms have lower coordination and their electronic configuration may be altered more easily. The desorption of halide species is more probable if the atom is bound to a surface site rather than to inner bulk atoms. With energetically less stable surfaces, the surface-to-volume ratio plays an important role in the overall stability of HPs.  $\text{Pb}^0$  diffusion occurs preferentially on the crystallite surface due to the lower surface diffusion barrier. However, bulk diffusion was also observed as highlighted in Figure 22 (b) and Figure 25 (b) causing distortions of the perovskite lattice upon movement. Most probably, electron irradiation enhances the diffusivity of lead through energy- and momentum transfer and enables bulk diffusion.<sup>45,96</sup> With increasing size, the formerly epitaxially bound Pb nanoparticles transformed into mostly spherically shaped anisotropic, nonepitaxial bound nanoparticles. Upon Pb consumption, the formation of voids around the nanoparticles was observed. Dang et al. stated, that upon long-term illumination of  $\text{CsPbBr}_3$ , the size of the Pb nanoparticles decreases again until the particle disappears. The particles first become amorphous and the atoms subsequently disperse on the remaining host lattice or carbon support film.<sup>45</sup> This explains the large number of voids but low number of Pb particles in the damaged nanocrystal highlighted in Figure 16 (c). It

was shown that thinner nanocrystals with a thickness of 3 nm and thus a high surface-to-volume ratio damaged much quicker compared to thicker nanocrystals. After exposure to similar electron doses for a long time (~90 min), Dang et al. neither observed any voids nor did XEDS measurements reveal any loss of Br species for the thicker crystals. Only Pb nanoparticles were found on the material surface.<sup>45</sup> This also explains the high stability of the CsPbBr<sub>3</sub> nanocrystal (~8 nm thickness) investigated in this work. After imaging with conventional electron doses and the acquisition of 4D STEM data, there was practically no beam damage visible except for the formation of Pb nanoparticles, which were only barely visible. In contrast, thinner regions showed stronger signs of beam damage with void formation around the Pb nanoparticles and a dismantled host lattice (Figure 16 (a-c)). To study HPs using electron ptychography, a compromise for sample thickness must be found. The sample must be thick enough to achieve a sufficiently high surface-to-volume ratio to minimize beam damage effects, but thin enough for the WPOA and POA to be valid. In their study on CsPbBr<sub>3</sub> nanocrystals, Dang et al. stated that beam damage in AIHPs is dominated by radiolysis, as the damage was more pronounced at lower beam energies. If knock-on damage was dominant the material would have been more stable with lower beam energies. Besides that, they investigated the effect of temperature on stability. With increasing temperature, more Pb nanoparticles were found after the same total doses were applied. In contrast, the lower the temperature, the less Pb nanoprecipitates were observed and below -60 °C no Pb particles were present. At low temperatures, the activation energy barrier for diffusion can probably not be overcome by the Pb<sup>0</sup> atoms and no cluster formation is possible. The halide species still desorbs at low temperature and Pb<sup>2+</sup> most likely reduces to Pb<sup>0</sup> without the formation of any clusters.<sup>45</sup> It was shown that cryogenic temperatures lead to a rapid amorphization of the perovskite lattice and do not provide any significant stability enhancement.<sup>46,49</sup> Therefore, the HP investigation in this work was conducted at room temperature with the highest possible beam energy. In addition to the formation of Pb nanoparticles and desorption of halide species, the formation of a second phase was observed in some cases for both CsPbI<sub>3</sub> and CsPbIBr<sub>2</sub> (see inset in Figure 29 or Figure 22 (c)). The second phase was not characterized further within the frame of this thesis and is most probably a Cs-containing phase. Zhou et al. also observed the formation of a second phase as a decomposition product in their study of the beam-induced structure evolution of CsPbIBr<sub>2</sub> thin films. They prepared similar HP thin films directly on the TEM grids via spin coating and suggest a maximum overall dose of 6000–8000 e<sup>-</sup>/Å<sup>2</sup> to avoid any beam damage. They found that a higher total dose (over 14000 e<sup>-</sup>/Å<sup>2</sup>) can be applied with discontinuous irradiation, i.e., via beam blanking between measurements. The formation of a CsPb<sub>(1-x)</sub>(IBr)<sub>(3-y)</sub> superstructure with ordered vacancies was observed in SAED measurements upon irradiation. The researchers identified the final decomposition product as metallic Pb nanoparticles, a Cs<sub>2</sub>IBr second phase and electron-stimulated desorption of I/Br species.<sup>44</sup> Chen et al. also agree that radiolysis might be the major cause of beam damage in CsPbI<sub>3</sub>. They observe rapid iodine desorption, void formation, and Pb aggregation in accordance with the results of this work.<sup>97</sup> In comparison to OIHPs, the damage mechanism in AIHPs is significantly different. In OIHPs, the less stable organic cations, e.g., CH<sub>3</sub>NH<sub>3</sub><sup>+</sup> are



more easily reduced or damaged than  $\text{Pb}^{2+}$ , and the decomposition product is usually  $\text{PbI}_2$ . When  $\text{Cs}^+$  replaces the highly sensitive organic cations, the  $\text{Pb}^{2+}$  species is reduced instead. The fatal difficulty, as mentioned earlier, is that  $\text{PbI}_2$  can be easily mistaken for the undecomposed perovskite structure.<sup>25,44,46,48</sup> A prime example is the study of Chen et al. While their study of  $\text{CsPbI}_3$  was unobjectionable, they investigated radiation effects in  $\text{PbI}_2$  instead of  $\text{CH}_3\text{NH}_3\text{PbI}_3$ . They explained the polycrystalline appearance and voids in their film by a poor crystal quality, although both are characteristic for the  $\text{PbI}_2$  decomposition product. Subsequently, numerous erroneous conclusions were drawn from this misconception. The observed beam damage could not be reconciled with the damage induced by radiolysis, knock-on, or heat-induced damage. They suggested that electron-beam-induced electric field formation was responsible for the “anomalous” beam damage phenomena they observed. This could be true for  $\text{PbI}_2$ , but not for  $\text{CH}_3\text{NH}_3\text{PbI}_3$ .<sup>97</sup> In general, a trend in stability was observed in the frame of this thesis. AIHPs are more stable under the electron beam than OIHPs due to their inorganic nature.<sup>98</sup> However, within the  $\text{CsPbX}_3$  class, the  $\text{CsPbBr}_3$  nanocrystals appeared to be more stable than the mixed perovskite  $\text{CsPbIBr}_2$  and this one in turn more stable than  $\text{CsPbI}_3$  under irradiation. For this reason, the  $\text{CsPbBr}_3$  nanocrystals could be investigated under conventional conditions, while the dose had to be drastically reduced for the mixed perovskite and even more lowered for the  $\text{CsPbI}_3$  sample. If the main damaging mechanism was knock-on damage, the stability gradient should be reversed. Since lighter elements are easier to displace,  $\text{CsPbI}_3$  should be the most stable phase in this case. However, knock-on damage can promote halide desorption and  $\text{Pb}^0$  diffusion via momentum transfer but is not the dominant damaging mechanism in AIHPs. Several studies observe faster damage at lower acceleration voltages.<sup>44,45,89</sup>

#### 4.4.2. TEM and STEM investigations of AIHPs

Optoelectronic properties of halide perovskites depend on structural features such as grain character, symmetry, octahedral distortions, etc. Since grain boundaries and other planar defects might play an important role in polycrystalline HPs, which researchers are not yet clear about, it is helpful to understand their properties. To study these features, it is of great importance to avoid artifacts caused by beam damage and resulting misinterpretations. Conventional atomic-resolution images from many literature studies contain Pb nanoparticles as a consequence of high-dose electron irradiation, three of them are exemplified in Figure 33.<sup>99–102</sup> Since the host lattice remains largely intact, the presence of Pb nanoparticles should not be a serious problem. However, conclusions about, e.g., lattice parameters should be drawn with caution because the composition might have changed. In some cases, Pb nanoparticles have been mistaken for HP nanocrystals leading to incorrect conclusions about particle morphologies.<sup>103</sup> Low-dose studies are important to avoid any misinterpretations, as seen also very often for OIHPs, especially when investigating damage caused by influences other than the electron beam.

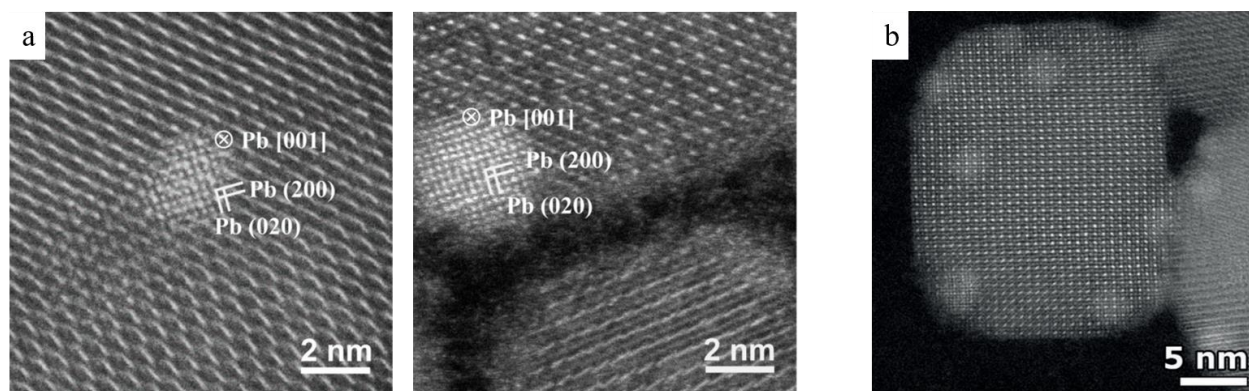


**Figure 33.** Lead precipitates upon beam damage in  $\text{CsPbX}_3$  perovskites. (a) STEM HAADF images of  $\text{CsPbBr}_3$  nanocrystals with cubic Pb precipitates oriented along the [001] direction.<sup>102</sup> (b) STEM HAADF image of a  $\text{CsPbI}_3$  nanocrystal with bright-contrast Pb precipitates.

Because of the beam sensitivity, there are few studies on atomic resolution imaging of  $\text{CsPbX}_3$  and most of them for  $\text{CsPbBr}_3$  which is found to be most stable under electron beam. Yu et al. investigated Ruddlesden-Popper phases in 2D nanosheets using HAADF-STEM. They reduced the electron dose with a short pixel dwell time at the expense of Br column contrast. In general, their experimental images agree well with structural models and simulations as illustrated in Figure 34. However, they assigned a cubic morphology to the structure, which may be questionable.<sup>104</sup>

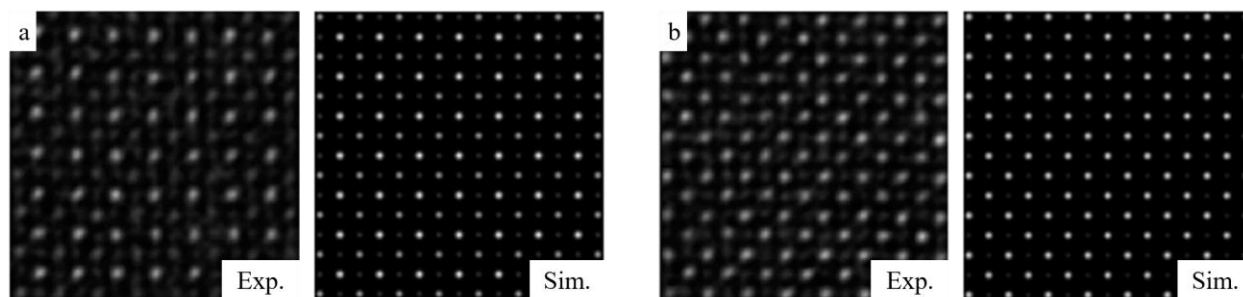


**Figure 34.** Experimental and simulated images of different domains in a single  $\text{CsPbBr}_3$  nanocrystal. (a) Perovskite phase and (b) Ruddlesden-Popper type structure both with poor Br and Cs contrast.

Although bromine, iodine, and cesium are not light elements, their contrast in ADF images is much poorer than the Pb contrast due to the nature of ADF imaging. In ptychographic phase imaging, all atomic species show high contrast even at low doses. This contrast enhancement provides access to atomic-scale structural phenomena. The potential of contrast improvement under low-dose conditions utilizing ptychography has already been demonstrated for  $\text{CsPbBr}_3$ . Dos Reis et al. used phase reconstructions to image elongated Br sites originating from out-of-phase octahedral rotations. In the noisy ADF images, bromine atoms were barely visible. They revealed atomic structure phenomena with a strong enhancement of bromine contrast compared to the simultaneously acquired ADF images. This allowed them to measure the octahedral rotation angle in a tetragonal  $I4/mcm$  crystal oriented along the [001] direction. For data acquisition, they used electron doses in the order of  $\sim 10^3 \text{ e}^-/\text{\AA}^2$ , and no beam damage was observed afterwards.<sup>105</sup> For the same material, Yu et al. imaged the atomic structure using low dose rate in-line holography, that combined

HRTEM and exit-wave reconstruction. In their study, image series were captured with a total dose of  $\sim 8000 \text{ e}^-/\text{\AA}^2$ . They were able to perform a quantitative structure determination without causing any beam damage. They revealed the coexistence of cubic high-temperature and orthorhombic low-temperature phases in single  $\text{CsPbBr}_3$  particles.<sup>106</sup>

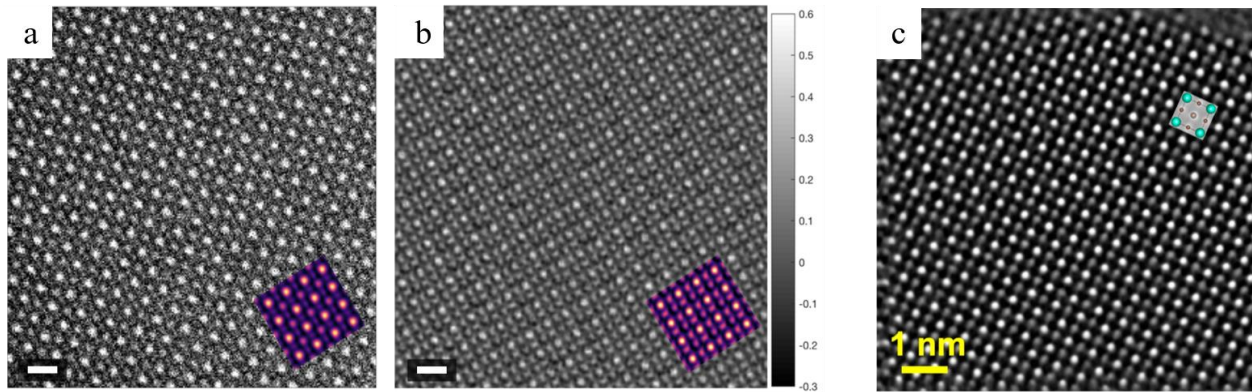


**Figure 35.** (a) Simultaneously acquired ADF image of  $\text{CsPbBr}_3$  with high noise level and poor Br contrast and (b) phase reconstructed image with enhanced contrast for all elements.<sup>105</sup> Scale bars in (a) and (b) are 5 Å. (c) Phase image of  $\text{CsPbBr}_3$  obtained by exit wave reconstruction of 80 low dose-rate HRTEM images.<sup>106</sup>

It was shown, that the beam sensitivity of HPs is strongly dependent on crystal size, composition, and synthesis routes. In some cases, even spectroscopic imaging was possible. Similar to the elemental maps extracted from EELS SIs in this work, Song et al. extracted XEDS elemental maps for a  $\text{CsPbBr}_3$  sample. They used total electron doses of  $\sim 9 \cdot 10^4 \text{ e}^-/\text{\AA}^2$  and observed no beam damage after data acquisition with improved perovskite stability. They found bromine columns constituting a perfect perovskite structure.<sup>107</sup>

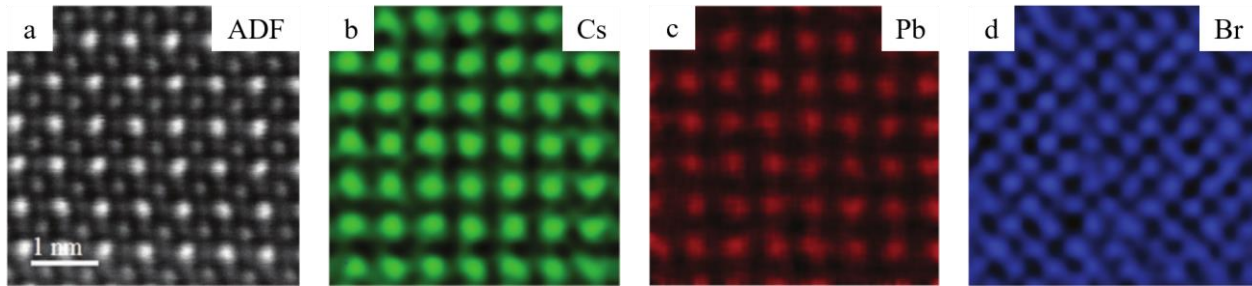


**Figure 36.** Atomic resolution XEDS elemental mapping of an orthorhombic  $\text{CsPbBr}_3$  nanocrystal. (a) Simultaneously acquired ADF image, (b) Cs atomic columns, (c) Pb atomic columns, and (d) Br atomic columns.<sup>107</sup>

In this work, it was shown that ptychography is particularly suitable for high-resolution imaging even for more sensitive all-inorganic halide perovskites ( $\text{CsPbIBr}_2$  and  $\text{CsPbI}_3$ ). Compared to conventional imaging, ptychography opens the possibility to study the structural properties of HPs without damage. At low electron doses, maximum contrast transfer is achieved for fine specimen details. With technical advances in data processing and imaging speed, DEC-STEM studies will be important for the further development of perovskite optoelectronic devices.

## 4.5. Sampling considerations

### 4.5.1. Probe step size

Since all spatial frequencies given by the diffraction limit should be represented, a probe step size must be chosen that contains all spatial frequencies for a given resolution in the context of the Nyquist-Shannon sampling theorem.<sup>108</sup> For a given aperture with a convergence angle  $\alpha$  and electron wavelength  $\lambda$ , the minimum distance between adjacent probe positions  $\Delta R_0$  to include the maximum theoretically possible spatial frequency is given as

$$\Delta R_0 = \frac{\lambda}{4\alpha} \quad (4.9)$$

This results in a minimum step size of 0.4354 Å for the 20 µm aperture and a minimum step size of 0.3734 Å for the 30 µm aperture. Undersampled data give rise to aliasing effects and thus periodic artefacts in the phase reconstructions. Oversampled data offer no advantages in terms of resolution or image quality, but also have no negative side effects other than higher electron dose. The step size should be chosen slightly smaller than the calculated minimum step size. For the 4D STEM datasets, step sizes of 0.1502 Å (CsPbBr<sub>3</sub>), 0.1213 Å (CsPbIBr<sub>2</sub>), and 0.1230 Å (CsPbI<sub>3</sub>) were used. Due to the slight oversampling, aliasing artifacts are excluded. In general, the minimum step size can be reduced by lower acceleration voltages (larger electron wavelengths) or smaller apertures. However, smaller apertures reduce the highest achievable resolution. At lower acceleration voltages the influences of temporal incoherence reduce the data quality.

### 4.5.2. Detector sampling conditions

The resolution of the detector plane is determined by the angular range of the individual pixels. The detector resolution can be controlled by adjusting the effective distance between the image- and detector plane. Depending on this effective distance (camera length), the number of pixels used to sample the bright-field disc, from which the phase information is extracted, can be adjusted. Yang et al. showed that a minimum array of 16×16 pixels is sufficient to obtain the highest signal-to-noise ratio, which is not further increased by using more pixels. Using only 16×16 detector pixels significantly increases readout and data acquisition speeds allowing for faster data acquisition with a lower dose. However, Yang et al. neglected any residual aberrations in their studies on simulated data. Under realistic conditions, a larger number of pixels may be preferential.<sup>58</sup> For the acquisition of 4D STEM datasets in this study, the entire detector area of 256×256 pixels was used. The camera length was set so that the bright-field disk extended to 40×40 pixels for the 20 µm aperture and 104×104 pixels for the 30 µm aperture to ensure sufficient sampling of the detector plane. As the entire detector area was used and not only the bright-field information, dark-field electrons were recorded as well and synthetic image calculations were possible. To reduce the scanning speed, a different method was used, which is discussed in detail below. Furthermore, poor sampling in reciprocal space

(binning or small amount of detector pixels available) can be compensated by dense sampling in the real space by controlling the probe step size and vice versa.<sup>109</sup>

#### 4.5.3. Binary ptychography

Besides all the advantages offered by the use of DEC and the variety of techniques they bring (virtual imaging, orientation – and strain mapping, phase contrast imaging, etc.), the only limiting factor of slow scanning speeds remains. This makes it particularly challenging to perform low dose measurements on beam sensitive materials. Furthermore, scan distortions, sample drift, and instabilities in the microscope alignment are more pronounced in datasets acquired with slow speeds. For a gap-less mode with high dynamic range (4095 e<sup>-</sup>/pixel) and a frame time of 0.55 ms, even very small currents would result in a high overall electron dose. These doses are too high for radiation-sensitive materials, especially HPs and would inevitably lead to damage. With a frame time of 0.55 ms per frame, the acquisition of the CsPbI<sub>3</sub> dataset would have taken ~140 s and a dose of about  $4 \cdot 10^4$  e<sup>-</sup>/Å<sup>2</sup> would have been required. The sample would have drifted considerably during this period and the result would probably be uninterpretable. However, the frame speed of the DEC can be increased strongly. This can be achieved either by hardware binning, windowing, or by a reduction of the detector dynamic range.<sup>84,110</sup> The latter was carried out in this thesis to enable faster frame rates. The counting depth of the MerlinEM Medipix3 detector was reduced to 1-bit. That means each detector pixel can only record either 1 or 0 within one frame. With this adjustment, the frame time was reduced to 48 µs and the data acquisition time was reduced from 140 s to 12 s. Example binary CBED patterns from each of the three datasets are shown in Figure 37.

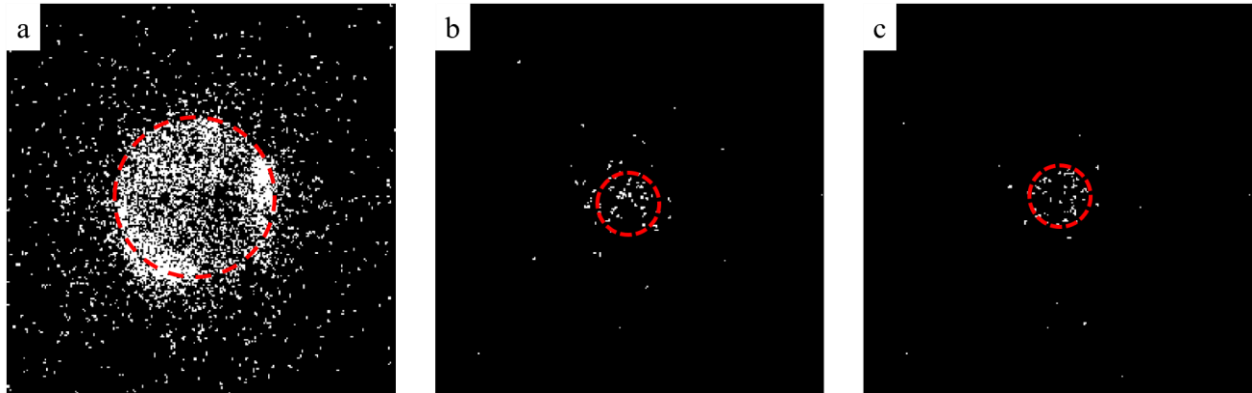


**Figure 37.** Example single frame binary CBED patterns from (a) CsPbBr<sub>3</sub>, (b) CsPbIBr<sub>2</sub>, and (c) CsPbI<sub>3</sub> datasets. Red dashed circles indicate the radius of the bright-field disc.

Individual electron events are distinguishable. However, it is also apparent that the higher the dose, the more electrons are detected and the bright-field disc becomes slightly saturated. For really high doses, every bright-field pixel would be 1 and no phase reconstruction would be possible. Conversely, it has been shown that there is also a lower dose limit under which there is not enough signal in the CBEDs to reconstruct the phase.<sup>84</sup> In this thesis, the use of the 1-bit mode for binary data acquisition has been shown to be an effective method to record datasets at high magnification, with a low dose and a fast frame time. Even at moderate

doses in the case of CsPbBr<sub>3</sub>, a high-contrast phase image was obtained with binary data. The results demonstrate, that a high dynamic range which can be achieved, e.g., in the 12-bit counting mode on cost of acquisition speed, is not always necessary to obtain high-quality data especially under low-dose conditions.

## 5. Summary

It was shown that ptychography is a promising technique for dose-efficient imaging of beam-sensitive materials at low doses. Taking advantage of DEC's and ongoing improvements in big data processing, high-SNR images of the atomic structure can be obtained without causing structural damage. The reconstructions showed a strong contrast for all atomic species independent of their atomic number. With the DEC, it is not only possible to solve the phase problem, but also any detector masks can be applied to the data, which facilitates synthetic imaging. With the universal detector, multiple measurements can be performed simultaneously on the same dataset. The relatively slow readout speed of the DEC was increased by binary data acquisition and it was shown that this approach works even at moderate doses without saturation of the bright-field disc. Effects of sample drift and high doses are lowered. A high dynamic range is not always required for high-quality datasets, especially at low-dose conditions. In the reconstructions, a superior dose efficiency with improved SNRs enabled the visualization of fine structural details, invisible in ADF images captured with scintillator-based detectors that fail under low-dose conditions. The use of smaller apertures not only enabled low-dose imaging, but reduced the influence of any aberrations drastically. High-spatial-resolution images were obtained in the absence of aberrations approaching the diffraction limit given by the aperture. Although the absolute resolution reduces when smaller apertures are used, the relative resolution with respect to the diffraction limit is much better. It was shown that even for slightly thicker samples ptychographic reconstructions give a representation of the structure. However, the resolution decreases and the images appear to become increasingly blurry. Thickness effects make the approximation of WPOA and POA inapplicable and thus the multiplicative transfer function is no longer valid. Nevertheless, a compromise for sample thickness must be found concerning beam damage and ptychography. The thinner the sample, the better ptychography works, but the faster the sample is damaged. Beam damage in AIHPs investigated in this study is characterized by a reduction of  $\text{Pb}^{2+}$  species to form metallic Pb nanoparticles and desorption of halide species from the material. The dominant damage mechanism is most probably radiolysis.



## 6. Outlook

Although it was shown that high-resolution low-dose imaging of AIHPs is possible via electron ptychography, doses in the  $10^3 \text{ e}^-/\text{\AA}^2$  range are still one order of magnitude too high to enable imaging of OIHPs. The main limiting factors so far have been the slow detector frame time and the non-existent DEC live mode. At slow acquisition speeds, higher doses are automatically applied. To counteract this, the beam current was drastically reduced and small apertures were used. This resulted in very poor ADF detector signals. Thus, the microscope adjustment was much harder, required more time and higher doses. In addition, insertion and retraction as well as proper centering of the electron beam between the measurements is unfavorable. Detector frame times will be enhanced in future works by detector binning and reduction of active pixels to the bright-field disc area only. Besides that, a live mode of the 4D STEM camera will be available, which will allow for easier adjustments due to the superior detector performance at low-dose conditions allowing for even lower doses. Another insurmountable problem was the contact of the specimen with the atmosphere when they were mounted into the sample holder. Being manufactured and stored in argon atmosphere and investigated in ultra-high vacuum, a brief contact with air and thus oxygen and moisture could not be prevented. While the AIHP samples did not show visible damage after short contact with air, for OIHPs in most cases severe damage was visible. Whether this damage was a result of air contact or occurred immediately upon illumination cannot be specified. Due to the severe damage, OIHPs could not be investigated as part of this work but will be the subject of future work. In the future, the StEM group will own a transfer holder that allows for air contact free transfer of the sample from the argon atmosphere to the TEM vacuum. This will prevent damage caused by moisture or air. Furthermore, protective measures, such as graphene encapsulation could be considered to reduce beam damage. There is an urgent need to develop and use TEM-based tools for the elucidation of many ambiguities in HP materials to optimize their performance. Overall, electron ptychography is growing in popularity and has the potential to become an important tool for low-dose investigations in STEM. With improvements in data processing, storage and DEC, 4D STEM will be an important tool to investigate structure-property relationships in HPs. It will contribute to the understanding of degradation mechanisms, defects, and stability enhancement for applications in real life. Clarifying key questions about the atomistic origin of optoelectronic properties, degradation mechanisms, stabilization possibilities, crystallization mechanisms from precursor solutions, etc. are the future goals.



## 7. References

1. Li, J., Johnson, G., Zhang, S. & Su, D. In situ transmission electron microscopy for energy applications. *Joule* **3**, 4–8; 10.1016/j.joule.2018.12.007 (2019).
2. Abou-Ras, D., Nichterwitz, M., Romero, M. J. & Schmidt, S. S. Electron microscopy on thin films for solar cells. In *Advanced characterization techniques for thin film solar cells*, edited by D. Abou-Ras, T. Kirchartz & U. Rau (Wiley-VCH Verlag GmbH & Co. KGaA, Weinheim, Germany, 2016), pp. 371–420.
3. Smith, D. J. Characterization of nanomaterials using transmission electron microscopy. In *Chemistry of colloidal nanocrystals*, edited by A. I. Kirkland & S. J. Haigh (Royal Society of Chemistry, Cambridge, 2021), pp. 1–29.
4. Boseck, S. Electron microscopy in medicine and biology: applications. In *Optics in biomedical sciences*, edited by J. M. Enoch, G. von Bally & P. Greguss (Springer Berlin Heidelberg, Berlin, Heidelberg, 1982), Vol. 31, pp. 15–20.
5. Franken, L. E., Grünewald, K., Boekema, E. J. & Stuart, M. C. A. A technical introduction to transmission electron microscopy for soft-matter: imaging, possibilities, choices, and technical developments. *Small* **16**, e1906198; 10.1002/sml.201906198 (2020).
6. Sciau, P. Transmission Electron Microscopy: Emerging investigations for cultural heritage materials. In *Advances in imaging electron physics* (Elsevier, 2016), Vol. 198, pp. 43–67.
7. Williams, D. B. & Carter, C. B. *Transmission electron microscopy. A textbook for materials science*. 2nd ed. (Springer, New York, London, 2009).
8. Goodhew, P. General introduction to transmission electron microscopy (TEM). In *Aberration-corrected analytical transmission electron microscopy*, edited by R. Brydson (John Wiley & Sons, Ltd, Chichester, United Kingdom, 2011), pp. 1–19.
9. Graef, M. de. *Introduction to conventional transmission electron microscopy*. (Cambridge University Press, Cambridge, 2009).
10. Tanaka, M. Convergent-beam electron diffraction. In *Electron crystallography*, edited by D. L. Dorset, S. Hovmöller & X. Zou (Springer Netherlands, Dordrecht, 1997), pp. 77–113.
11. Nellist, P. D. The principles of STEM imaging. In *Scanning transmission electron microscopy*, edited by S. J. Pennycook & P. D. Nellist (Springer New York, New York, NY, 2011), pp. 91–115.
12. Ophus, C. Four-dimensional scanning transmission electron microscopy (4D-STEM): From scanning nanodiffraction to ptychography and beyond. *Microscopy and Microanalysis* **25**, 563–582; 10.1017/S1431927619000497 (2019).
13. Park, J. *et al.* Bandgap measurement of thin dielectric films using monochromated STEM-EELS. *Ultramicroscopy* **109**, 1183–1188; 10.1016/j.ultramic.2009.04.005 (2009).
14. Potapov, P. L., Engelmann, H.-J., Zschech, E. & Stöger-Pollach, M. Measuring the dielectric constant of materials from valence EELS. *Micron* **40**, 262–268; 10.1016/j.micron.2008.07.006 (2009).
15. Iakoubovskii, K., Mitsuishi, K., Nakayama, Y. & Furuya, K. Thickness measurements with electron energy loss spectroscopy. *Microscopy Research and Technique* **71**, 626–631; 10.1002/jemt.20597 (2008).
16. Garvie, L. A. J., Craven, A. J. & Brydson, R. Use of electron-energy loss near-edge fine structure in the study of minerals. *American Mineralogist* **79**, 411–425 (1994).

17. Egerton, R. F. Energy-loss instrumentation. In *Electron energy-loss spectroscopy in the electron microscope*, edited by R. F. Egerton (Springer US, Boston, MA, 2011), pp. 29–109.
18. Hofer, F., Schmidt, F. P., Grogger, W. & Kothleitner, G. Fundamentals of electron energy-loss spectroscopy. *IOP Conference Series: Materials Science and Engineering* **109**, 12007; 10.1088/1757-899X/109/1/012007 (2016).
19. Kässens, M., Reimer, R. & Wegerhoff, R. Mikroskopische Verfahren. In *Romeis - Mikroskopische Technik*, edited by M. Mulisch & U. Welsch (Springer Berlin Heidelberg, Berlin, Heidelberg, 2015), pp. 1–42.
20. Shindo, D. & Oikawa, T. Energy dispersive x-ray spectroscopy. In *Analytical electron microscopy for materials science*, edited by D. Shindo & T. Oikawa (Springer Japan, Tokyo, 2002), pp. 81–102.
21. Hofmann, S. Quantitative analysis (data evaluation). In *Auger- and x-ray photoelectron spectroscopy in materials science*, edited by S. Hofmann (Springer Berlin Heidelberg, Berlin, Heidelberg, 2013), Vol. 49, pp. 77–204.
22. Müllejans H. & Bruley. J. Electron energy-loss spectroscopy (EELS) ; comparison with X-ray analysis. *Le Journal de Physique IV* **03**, 2083-2092; 10.1051/jp4:19937332 (1993).
23. Chattarji, D. *The theory of Auger transitions* (Academic Press, London, 1976).
24. Egerton, R. F. Radiation damage to organic and inorganic specimens in the TEM. *Micron* **119**, 72–87; 10.1016/j.micron.2019.01.005 (2019).
25. Chen, S. & Gao, P. Challenges, myths, and opportunities of electron microscopy on halide perovskites. *Journal of Applied Physics* **128**, 10901; 10.1063/5.0012310 (2020).
26. Katz, E. A. Perovskite: Name puzzle and German-Russian odyssey of discovery. *Helvetica Chimica Acta* **103**, e2000061; 10.1002/hlca.202000061 (2020).
27. Mitchell, R. H., Welch, M. D. & Chakhmouradian, A. R. Nomenclature of the perovskite supergroup: A hierarchical system of classification based on crystal structure and composition. *Mineralogical Magazine* **81**, 411–461; 10.1180/minmag.2016.080.156 (2017).
28. Akkerman, Q. A. & Manna, L. What defines a halide perovskite? *ACS energy letters* **5**, 604–610; 10.1021/acsenerylett.0c00039 (2020).
29. Wang, P. *et al.* Solution-processable perovskite solar cells toward commercialization: Progress and challenges. *Advanced Functional Materials* **29**, 1807661; 10.1002/adfm.201807661 (2019).
30. Gao, L. & Yang, G. Organic-inorganic halide perovskites: From crystallization of polycrystalline films to solar cell applications. *Solar RRL* **4**, 1900200; 10.1002/solr.201900200 (2020).
31. Jena, A. K., Kulkarni, A. & Miyasaka, T. Halide Perovskite Photovoltaics: Background, Status, and Future Prospects. *Chemical Reviews* **119**, 3036–3103; 10.1021/acs.chemrev.8b00539 (2019).
32. Zhang, Q., Shang, Q., Su, R., Do, T. T. H. & Xiong, Q. Halide perovskite semiconductor lasers: Materials, cavity design, and low threshold. *Nano Letters* **21**, 1903–1914; 10.1021/acs.nanolett.0c03593 (2021).
33. Perumal Veeramalai, C. *et al.* Lead–halide perovskites for next-generation self-powered photodetectors: a comprehensive review. *Photonics Research* **9**, 968–991; 10.1364/PRJ.418450 (2021).
34. Zhou, Y., Chen, J., Bakr, O. M. & Mohammed, O. F. Metal halide perovskites for x-ray imaging scintillators and detectors. *ACS energy letters* **6**, 739–768; 10.1021/acsenerylett.0c02430 (2021).

35. Liu, X.-K. *et al.* Metal halide perovskites for light-emitting diodes. *Nature Materials* **20**, 10–21; 10.1038/s41563-020-0784-7 (2021).
36. Iftikhar, F. J. *et al.* Structural and optoelectronic properties of hybrid halide perovskites for solar cells. *Organic Electronics* **91**, 106077; 10.1016/j.orgel.2021.106077 (2021).
37. Kojima, A., Teshima, K., Shirai, Y. & Miyasaka, T. Organometal halide perovskites as visible-light sensitizers for photovoltaic cells. *Journal of the American Chemical Society* **131**, 6050–6051; 10.1021/ja809598r (2009).
38. National Renewable Energy laboratory (NREL). *Efficiency Records Chart* (<https://www.nrel.gov/pv/cell-efficiency.html>, accessed on 08/03/2021, ).
39. Xiang, W., Liu, S. & Tress, W. A review on the stability of inorganic metal halide perovskites: challenges and opportunities for stable solar cells. *Energy & Environmental Science* **14**, 2090–2113; 10.1039/D1EE00157D (2021).
40. Ke, W. & Kanatzidis, M. G. Prospects for low-toxicity lead-free perovskite solar cells. *Nature communications* **10**, 965; 10.1038/s41467-019-08918-3 (2019).
41. An, Y. *et al.* Structural stability of formamidinium- and cesium-based halide perovskites. *ACS energy letters* **6**, 1942–1969; 10.1021/acsnenergylett.1c00354 (2021).
42. Berhe, T. A. *et al.* Organometal halide perovskite solar cells: degradation and stability. *Energy & Environmental Science* **9**, 323–356; 10.1039/C5EE02733K (2016).
43. Chen, S. *et al.* Atomic scale insights into structure instability and decomposition pathway of methylammonium lead iodide perovskite. *Nature communications* **9**, 4807; 10.1038/s41467-018-07177-y (2018).
44. Zhou, X.-G. *et al.* Probing the electron beam-induced structural evolution of halide perovskite thin films by scanning transmission electron microscopy. *The Journal of Physical Chemistry C* **125**, 10786–10794; 10.1021/acs.jpcc.1c02156 (2021).
45. Dang, Z. *et al.* In situ transmission electron microscopy study of electron beam-induced transformations in colloidal cesium lead halide perovskite nanocrystals. *ACS Nano* **11**, 2124–2132; 10.1021/acsnano.6b08324 (2017).
46. Chen, S. *et al.* Transmission electron microscopy of organic-inorganic hybrid perovskites: myths and truths. *Science Bulletin* **65**, 1643–1649; 10.1016/j.scib.2020.05.020 (2020).
47. Rothmann, M. U. *et al.* Atomic-scale microstructure of metal halide perovskite. *Science* **370**, eabb5940; 10.1126/science.abb5940 (2020).
48. Li, Y. *et al.* Unravelling atomic structure and degradation mechanisms of organic-inorganic halide perovskites by cryo-EM. *Joule* **3**, 2854–2866; 10.1016/j.joule.2019.08.016 (2019).
49. Rothmann, M. U. *et al.* Structural and chemical changes to CH<sub>3</sub>NH<sub>3</sub>PbI<sub>3</sub> induced by electron and gallium ion beams. *Advanced Materials* **30**, e1800629; 10.1002/adma.201800629 (2018).
50. Bursill, L. A., Thomas, J. M. & Rao, K. J. Stability of zeolites under electron irradiation and imaging of heavy cations in silicates. *Nature* **289**, 157–158; 10.1038/289157a0 (1981).
51. Brennan, M. C., Kuno, M. & Rouvimov, S. Crystal structure individual CsPbBr<sub>3</sub> perovskite nanocubes. *Inorganic Chemistry* **58**, 1555–1560; 10.1021/acs.inorgchem.8b03078 (2019).
52. Zhang, D. *et al.* Atomic-resolution transmission electron microscopy of electron beam-sensitive crystalline materials. *Science* **359**, 675–679; 10.1126/science.aao0865 (2018).

53. Nellist, P. D. Scanning transmission electron microscopy. In *Science of microscopy*, edited by P. W. Hawkes & J. C. H. Spence (Springer New York, New York, 2007), pp. 65–132.
54. Rodenburg, J. M. & Bates, R. H. T. The theory of super-resolution electron microscopy via Wigner-distribution deconvolution. *Philosophical Transactions of the Royal Society of London. Series A: Physical and Engineering Sciences* **339**, 521–553; 10.1098/rsta.1992.0050 (1992).
55. Scherzer, O. The theoretical resolution limit of the electron microscope. *Journal of Applied Physics* **20**, 20–29; 10.1063/1.1698233 (1949).
56. Bracewell, R. N. *The Fourier transform and its applications*. 2nd ed. (McGraw-Hill, Auckland, 1985).
57. Pennycook, T. J. *et al.* Efficient phase contrast imaging in STEM using a pixelated detector. Part 1: experimental demonstration at atomic resolution. *Ultramicroscopy* **151**, 160–167; 10.1016/j.ultramic.2014.09.013 (2015).
58. Yang, H., Pennycook, T. J. & Nellist, P. D. Efficient phase contrast imaging in STEM using a pixelated detector. Part II: optimisation of imaging conditions. *Ultramicroscopy* **151**, 232–239; 10.1016/j.ultramic.2014.10.013 (2015).
59. Hoppe, W. Beugung im inhomogenen Primärstrahlwellenfeld. I. Prinzip einer Phasenmessung von Elektronenbeugungsinterferenzen. *Acta Crystallographica Section A* **25**, 495–501; 10.1107/S0567739469001045 (1969).
60. Rodenburg, J. M., McCallum, B. C. & Nellist, P. D. Experimental tests on double-resolution coherent imaging via STEM. *Ultramicroscopy* **48**, 304–314; 10.1016/0304-3991(93)90105-7 (1993).
61. Rodenburg, J. M. & Faulkner, H. M. L. A phase retrieval algorithm for shifting illumination. *Applied Physics Letters* **85**, 4795–4797; 10.1063/1.1823034 (2004).
62. Rodenburg, J. M. *et al.* Hard-x-ray lensless imaging of extended objects. *Physical Review Letters* **98**, 34801; 10.1103/PhysRevLett.98.034801 (2007).
63. Yang, H. *et al.* Simultaneous atomic-resolution electron ptychography and Z-contrast imaging of light and heavy elements in complex nanostructures. *Nature communications* **7**, 12532; 10.1038/ncomms12532 (2016).
64. O'Leary, C. M. *et al.* Contrast transfer and noise considerations in focused-probe electron ptychography. *Ultramicroscopy* **221**, 113189; 10.1016/j.ultramic.2020.113189 (2021).
65. Yang, H. *et al.* Electron ptychographic phase imaging of light elements in crystalline materials using Wigner distribution deconvolution. *Ultramicroscopy* **180**, 173–179; 10.1016/j.ultramic.2017.02.006 (2017).
66. Jiang, Y. *et al.* Electron ptychography of 2D materials to deep sub-ångström resolution. *Nature* **559**, 343–349; 10.1038/s41586-018-0298-5 (2018).
67. Cueva, P., Hovden, R., Mundy, J. A., Xin, H. L. & Muller, D. A. Data processing for atomic resolution electron energy loss spectroscopy. *Microscopy and Microanalysis* **18**, 667–675; 10.1017/S1431927612000244 (2012).
68. Chen, Z. *et al.* Cu<sup>2+</sup>-doped CsPbI<sub>3</sub> nanocrystals with enhanced stability for light-emitting diodes. *The Journal of Physical Chemistry Letters* **12**, 3038–3045; 10.1021/acs.jpclett.1c00515 (2021).
69. MacLaren, I., Macgregor, T. A., Allen, C. S. & Kirkland, A. I. Detectors-The ongoing revolution in scanning transmission electron microscopy and why this important to material characterization. *APL Materials* **8**, 110901; 10.1063/5.0026992 (2020).

70. Nord, M. *et al.* Fast pixelated detectors in scanning transmission electron microscopy. Part I: Data acquisition, live processing, and storage. *Microscopy and Microanalysis* **26**, 653–666; 10.1017/S1431927620001713 (2020).
71. Levin, B. D. A. Direct detectors and their applications in electron microscopy for materials science. *Journal of Physics: Materials* **4**, 42005; 10.1088/2515-7639/ac0ff9 (2021).
72. Seki, T., Ikuhara, Y. & Shibata, N. Theoretical framework of statistical noise in scanning transmission electron microscopy. *Ultramicroscopy* **193**, 118–125; 10.1016/j.ultramic.2018.06.014 (2018).
73. Mir, J. A. *et al.* Medipix3 Demonstration and understanding of near ideal detector performance for 60 & 80 keV electrons, 26.08.2016.
74. Fan, G. Y. & Ellisman, M. H. Digital imaging in transmission electron microscopy. *Journal of Microscopy* **200**, 1–13; 10.1046/j.1365-2818.2000.00737.x (2000).
75. Mir, J. A. *et al.* Characterisation of the Medipix3 detector for 60 and 80keV electrons. *Ultramicroscopy* **182**, 44–53; 10.1016/j.ultramic.2017.06.010 (2017).
76. O’Leary, C. *The development and applications of STEM ptychography using direct electron detectors* (University of Oxford, Oxford, 2020).
77. Wen, Y. *et al.* Simultaneous identification of low and high atomic number atoms in monolayer 2D materials using 4D scanning transmission electron microscopy. *Nano Letters* **19**, 6482–6491; 10.1021/acs.nanolett.9b02717 (2019).
78. Chen, Z. *et al.* Electron ptychography achieves atomic-resolution limits set by lattice vibrations. *Science* **372**, 826–831; 10.1126/science.abg2533 (2021).
79. Rayleigh. Investigations in optics, with special reference to the spectroscope. *The London, Edinburgh, and Dublin Philosophical Magazine and Journal of Science* **8**, 261–274; 10.1080/14786447908639684 (1879).
80. Weyland, M. & Muller, D. A. Tuning the convergence angle for optimum STEM performance (2020).
81. Haider, M., Uhlemann, S. & Zach, J. Upper limits for the residual aberrations of a high-resolution aberration-corrected STEM. *Ultramicroscopy* **81**, 163–175; 10.1016/S0304-3991(99)00194-1 (2000).
82. Ning, S. *et al.* Scanning distortion correction in STEM images. *Ultramicroscopy* **184**, 274–283; 10.1016/j.ultramic.2017.09.003 (2018).
83. van den Broek, W., van Aert, S., Goos, P. & van Dyck, D. Throughput maximization of particle radius measurements through balancing size versus current of the electron probe. *Ultramicroscopy* **111**, 940–947; 10.1016/j.ultramic.2010.11.025 (2011).
84. O’Leary, C. M. *et al.* Phase reconstruction using fast binary 4D STEM data. *Applied Physics Letters* **116**, 124101; 10.1063/1.5143213 (2020).
85. Chapman, H. N. *et al.* High-resolution ab initio three-dimensional x-ray diffraction microscopy. *Journal of the Optical Society of America A* **23**, 1179–1200; 10.1364/JOSAA.23.001179 (2006).
86. Tsai, E. H. R., Usov, I., Diaz, A., Menzel, A. & Guizar-Sicairos, M. X-ray ptychography with extended depth of field. *Optics Express* **24**, 29089–29108; 10.1364/OE.24.029089 (2016).
87. Plamann, T. & Rodenburg, J. M. Electron ptychography. II. Theory of three-dimensional propagation effects. *Acta Crystallographica Section A Foundations of Crystallography* **54**, 61–73; 10.1107/S0108767397010507 (1998).

88. Malis, T., Cheng, S. C. & Egerton, R. F. EELS log-ratio technique for specimen-thickness measurement in the TEM. *Journal of Electron Microscopy Technique* **8**, 193–200; 10.1002/jemt.1060080206 (1988).
89. Dang, Z., Luo, Y., Wang, X.-S., Imran, M. & Gao, P. Electron-beam-induced degradation of halide-perovskite-related semiconductor nanomaterials. *Chinese Optics Letters* **19**, 30002; 10.3788/COL202119.030002 (2021).
90. Philippe, B. *et al.* Chemical and electronic structure characterization of lead halide perovskites and stability behavior under different exposures—A photoelectron spectroscopy investigation. *Chemistry of Materials* **27**, 1720–1731; 10.1021/acs.chemmater.5b00348 (2015).
91. Pan, Z. W., Dai, Z. R. & Wang, Z. L. Lead oxide nanobelts and phase transformation induced by electron beam irradiation. *Applied Physics Letters* **80**, 309–311; 10.1063/1.1432749 (2002).
92. Knotek, M. L. Stimulated desorption. *Reports on Progress in Physics* **47**, 1499–1561; 10.1088/0034-4885/47/11/002 (1984).
93. Gonzalez-Martinez, I. G. *et al.* Electron-beam induced synthesis of nanostructures: a review. *Nanoscale* **8**, 11340–11362; 10.1039/C6NR01941B (2016).
94. Knotek, M. L. & Feibelman, P. J. Ion desorption by core-hole auger decay. *Physical Review Letters* **40**, 964–967; 10.1103/PhysRevLett.40.964 (1978).
95. Egerton, R. F., Li, P. & Malac, M. Radiation damage in the TEM and SEM. *Micron* **35**, 399–409; 10.1016/j.micron.2004.02.003 (2004).
96. Egerton, R. F. Beam-induced motion of adatoms in the transmission electron microscope. *Microscopy and Microanalysis* **19**, 479–486; 10.1017/S1431927612014274 (2013).
97. Chen, X. & Wang, Z. Investigating chemical and structural instabilities of lead halide perovskite induced by electron beam irradiation. *Micron* **116**, 73–79; 10.1016/j.micron.2018.09.010 (2019).
98. Ran, J. *et al.* Electron-beam-related studies of halide perovskites: Challenges and opportunities. *Advanced Energy Materials* **10**, 1903191; 10.1002/aenm.201903191 (2020).
99. Sun, J.-K. *et al.* Polar solvent induced lattice distortion of cubic CsPbI<sub>3</sub> nanocubes and hierarchical self-assembly into orthorhombic single-crystalline nanowires. *Journal of the American Chemical Society* **140**, 11705–11715; 10.1021/jacs.8b05949 (2018).
100. Tong, Y. *et al.* Highly luminescent cesium lead halide perovskite nanocrystals with tunable composition and thickness by ultrasonication. *Angewandte Chemie* **55**, 13887–13892; 10.1002/anie.201605909 (2016).
101. Binyamin, T. *et al.* Fully inorganic mixed cation lead halide perovskite nanoparticles: A study at the atomic level. *Chemistry of Materials* **32**, 1467–1474; 10.1021/acs.chemmater.9b04426 (2020).
102. Zhang, M., Li, H., Jing, Q., Lu, Z. & Wang, P. Atomic characterization of byproduct nanoparticles on cesium lead halide nanocrystals using high-resolution scanning transmission electron microscopy. *Crystals* **8**, 2; 10.3390/cryst8010002 (2017).
103. Szeremeta, J., Antoniuk, M. A., Wawrzyńczyk, D., Nyk, M. & Samoć, M. The two-photon absorption cross-section studies of CsPbX<sub>3</sub> (X = I, Br, Cl) nanocrystals. *Nanomaterials* **10**, 1054; 10.3390/nano10061054 (2020).
104. Yu, Y., Zhang, D. & Yang, P. Ruddlesden-Popper phase in two-dimensional inorganic halide perovskites: A plausible model and the supporting observations. *Nano Letters* **17**, 5489–5494; 10.1021/acs.nanolett.7b02146 (2017).



105. dos Reis, R. *et al.* Determination of the structural phase and octahedral rotation angle in halide perovskites. *Applied Physics Letters* **112**, 71901; 10.1063/1.5017537 (2018).
106. Yu, Y. *et al.* Atomic resolution imaging of halide perovskites. *Nano Letters* **16**, 7530–7535; 10.1021/acs.nanolett.6b03331 (2016).
107. Song, K. *et al.* Atomic-resolution imaging of halide perovskites using electron microscopy. *Advanced Energy Materials* **10**, 1904006; 10.1002/aenm.201904006 (2020).
108. Shannon, C. E. A mathematical theory of communication. *Bell System Technical Journal* **27**, 379–423; 10.1002/j.1538-7305.1948.tb01338.x (1948).
109. Batey, D. J. *et al.* Reciprocal-space up-sampling from real-space oversampling in x-ray ptychography. *Physical Review A* **89**; 10.1103/PhysRevA.89.043812 (2014).
110. Ryll, H. *et al.* A pnCCD-based, fast direct single electron imaging camera for TEM and STEM. *J. Inst.* **11**, P04006; 10.1088/1748-0221/11/04/P04006 (2016).